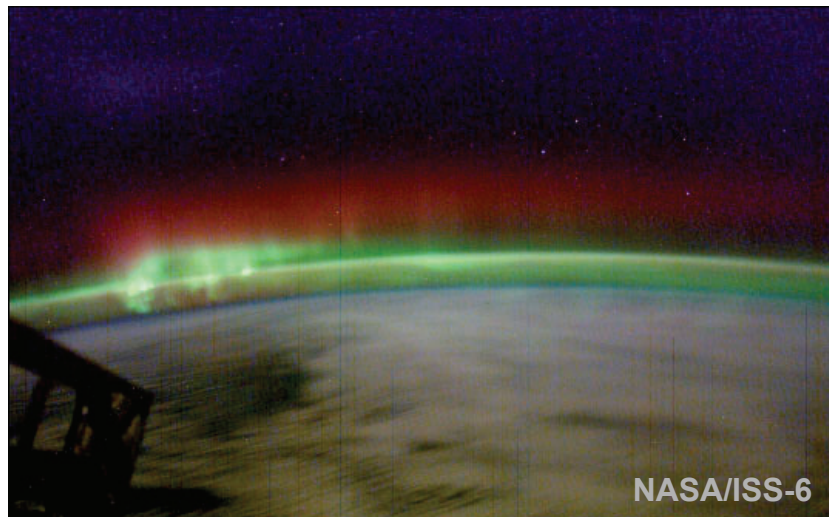




# Multi-instrument studies of polar mesopause region temperature and airglow variability

Margit E. Dyrland



*A dissertation for the degree of Philosophiae Doctor (PhD)*

**UNIVERSITY OF TROMSØ**

Faculty of Science and Technology

Department of Physics and Technology

&

**THE UNIVERSITY CENTRE IN SVALBARD**

Department of Arctic Geophysics

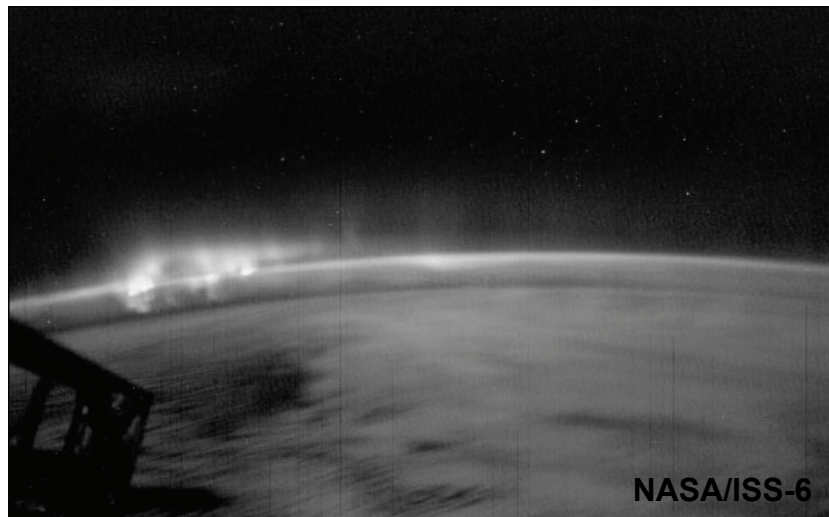
January 2010





# Multi-instrument studies of polar mesopause region temperature and airglow variability

Margit E. Dyrland



*A dissertation for the degree of Philosophiae Doctor (PhD)*

**UNIVERSITY OF TROMSØ**

Faculty of Science and Technology

Department of Physics and Technology

&

**THE UNIVERSITY CENTRE IN SVALBARD**

Department of Arctic Geophysics

January 2010

**Front page image:**

Aurora and airglow photographed from the International Space Station (ISS).  
Image Science and Analysis Laboratory, NASA-Johnson Space Center.

<http://eol.jsc.nasa.gov/scripts/sseop/photo.pl?mission=ISS006&roll=E&frame=47517>

**Author's address:** The University Centre in Svalbard  
P.O. Box 156  
9171 Longyearbyen  
Norway  
[margit.dyrland@unis.no](mailto:margit.dyrland@unis.no)

**Supervisors:** Professor Fred Sigernes  
Department of Arctic Geophysics  
The University Centre in Svalbard  
[fred.sigernes@unis.no](mailto:fred.sigernes@unis.no)

Professor Ove Havnes  
Department of Physics and Technology  
The University of Tromsø  
N-9037 Tromsø  
Norway  
[ove.havnes@uit.no](mailto:ove.havnes@uit.no)

## **Acknowledgements**

Many people deserve a big thank you for helping me get to the point where I could hand in this thesis. First I would like to thank my great supervisor Fred Sigernes, who encouraged me to apply for the position, helped write the project proposal and have helped me throughout the whole process from the start to the end. My official supervisor Ove Havnes at the University of Tromsø also deserves thanks for his kind help and advice.

In addition to my "official" team, I have gotten invaluable help from collaborating with the two clever, kind and cool professors Frank Mulligan at the National University of Ireland Maynooth and Chris Hall at the University of Tromsø. Their dedication and support have been crucial. A huge thank you to both of you! I would also like to thank a number of my other research colleagues for good advice and support throughout the years: Bob Lowe, Chuck Deehr, John French and the rest of the NDMC (Network for the Detection of Mesopause Change) team who taught me that I was not alone in this field and with my scientific problems. I am also indebted to Professors Masaki Tsutsumi and Takehiko Aso who have kindly allowed me to play with data from the Nippon/NIPR/Norway Svalbard meteor radar. The scientific teams of NASA's TIMED SABER and EOS Aura MLS satellite missions have put down huge efforts for preparing these great data for public access – thank you!

The middle- and upper atmospheric research group at UNIS was a great place to work. In addition to Fred - Dag Lorentzen, Kjellmar Oksavik, Åsmund Skjæveland and Jeff Holmes were my fellow companions on many "optical meetings", the eight-thirty (ehh.. nine-ish...) coffee breaks and trips to the Auroral station and KHO. A special thanks to Jeff for keeping up with my many calls when I was stuck with some simple problem out there, and for being my friend! During the many hours at the optical observatories, I was fortunate to meet a lot of interesting and nice visiting scientists who inspired me a lot. I'm also grateful to the rest of the people at UNIS for making it a great place to work and for helping with practical matters.

I would also like to thank my fabulous family and good friends for being there for me. My "closest girl friends" deserve special mention for keeping me sane and I'm fortunate to have a bunch of them: Ingvild, Ellen and Annett (UiO-girls and

partners in “girls-not-feeling-that-smart-doing-phd-crime”..), Malin, Hilde, Monica, Liv Mari, Ellen, Marina, Stine, Ingvild “i“, Elise, Helen and Anja (fantastic Longyearbyen chicks), and Åshild x 2, Karianne, Kristine, Veronica, Gro Anita, Siv, Ellen Mari, Christina and Målfrid (my “good old” friends).

I feel very fortunate to have been able to live on Svalbard for many years and experience the wonderful wildlife and people here. When in a bad mood, all I have to do is go down to the dog yard and see their happy faces and my worries seem to disappear. My dogs help me disconnect and just be.

Last and most importantly I would like to thank my darling Urban for loving me. I love you too!

*Margit :o)*

## Preface

The work on this thesis started in August 2005 and has been funded by The University Centre in Svalbard (UNIS) through their grant from the Norwegian Ministry of Education and Research. The major part of the research has been carried out at UNIS in Longyearbyen, but much time has also been spent at the optical observatories located close by: the *Auroral Station in Adventdalen* (August 2005 to September 2007) and the *Kjell Henriksen Observatory (KHO)* (September 2007 to September 2009).

The main object of this work has been to measure temperatures in the mesopause region by utilizing the infrastructure already present at Svalbard and combine with data from satellites to improve these temperature estimates. The project also includes investigation of atmospheric dynamics inferred from the temperature series and airglow spectra.

In addition to the work done in direct relation to my PhD project, I have participated in several other projects. Some of these have resulted in publications that are not part of this thesis. The papers are listed below.

- Sigernes, F., J. M. Holmes, M. Dyrland, D. A. Lorentzen, , S. A. Chernouss, T. Svenoe, J. Moen and C. S. Deehr (2007), Absolute calibration of optical devices with a small field of view, *Journal of Optical Technology*, 74, 669-674.
- Sigernes, F., J. M. Holmes, M. Dyrland, D. A. Lorentzen, T. Svenoe, K. Heia, T. Aso, S. Chernouss, and C. S. Deehr (2008), Sensitivity calibration of digital colour cameras for auroral imaging, *Optics Express*, 16(20), 15623-15632.
- Hall, C. M., J. Röttger, K. Kuyeng, M. Tsutsumi, M. Dyrland, and J. L. Chau (2009), Polar mesospheric summer echoes at 78°N, 16°E, 2008: First results of the refurbished sounding system (SOUSY) Svalbard radar, *J. Geophys. Res.*, 114, D11111, doi:10.1029/2008JD011543.



## **Abstract**

The polar mesopause region (80-100 km) is one of the most dynamic regions of the Earth's atmosphere. It may hold important clues to understand the Earth's energy and climate balance. This thesis uses a multi-instrument approach to gain new insight into the relation between temperature and airglow variations and dynamical processes occurring in the mesopause region above Svalbard (78°N, 16°E).

A daily rotational temperature series derived from ground-based spectral measurements of hydroxyl (OH) airglow emissions from 1980-2001 has been updated until February 2005, and analyzed for short time periodicities and long term trends. Temperatures from the unusually warm 2003-2004 winter were compared to temperatures measured by SABER (Sounding of the Atmosphere using Broadband Emission Radiometry) on the TIMED (Thermosphere Ionosphere Mesosphere Energetics and Dynamics) satellite. Studies of OH volume emission rates measured by SABER reveal that the assumption of a constant height for the OH layer is a strong simplification for the data from Svalbard. The observed lowering of the peak altitude of the order of ~10 km may explain up to 30% of the temperature increase observed during 2003-2004. A strong linear correlation was found between SABER measurements of OH temperatures and peak altitudes and meridional mesopause region winds measured by the Nippon/Norway Svalbard Meteor Radar (NSMR). This implies a strong coupling between the meridional wind strength, vertical transport and temperature on a local scale.

Knowledge of the peak altitude of the OH layer may be crucial for assessing variabilities observed in OH temperatures. By comparing simultaneous measurements of OH layer emissions made by SABER and the ground-based spectrometer, an empirical relationship was found between the OH layer peak altitude and brightness. This enables us to assign peak altitudes to ground-based measured OH spectra even when no satellite measurements are available.

While the retrieval of OH rotational temperatures depends on the observing conditions, the NSMR radar can measure meteor echoes during the whole day and year. The results using temperatures measured by the satellite instrument Aura MLS (Microwave Limb Sounder) to calibrate the initial temperatures obtained by the radar are presented. We argue that we obtain a better estimate for the neutral air temperature at 90 km than previously analyzed data from the NSMR radar.



# Contents

This thesis is based on four papers. All of them are attached in *manuscript form* although with figures embedded in the text. They will be referred to in the text by their numbers. In the introductory part, the motivation and background for the studies – as well as a synthesis of the analysis and results - are presented.

<b>1. Introduction</b>	<b>1</b>
1.1 Atmosphere and climate .....	1
1.2 Unresolved scientific issues .....	2
1.3 Structure of the thesis .....	3
<b>2. Middle atmosphere dynamics</b>	<b>5</b>
2.1 The mesopause region defined .....	5
2.2 Large-scale circulation .....	7
2.3 Heating and cooling processes .....	9
2.4 Sudden stratospheric warming and mesospheric cooling .....	9
2.5 Short and long term variability .....	11
<b>3. Site and instruments</b>	<b>13</b>
3.1 Site description .....	13
3.2 The Ebert-Fastie spectrometer .....	14
3.3 The NSMR meteor radar .....	15
3.4 TIMED SABER .....	16
3.5 Aura MLS .....	17
<b>4. Remote sensing of hydroxyl airglow</b>	<b>19</b>
4.1 Airglow emissions .....	19
4.2 Mechanism for hydroxyl airglow .....	20
4.3 OH molecular spectra and the rotational temperature .....	21
4.4 Data handling .....	24
4.5 Choice of transition coefficients .....	26
4.6 Calibration .....	27

4.7	Uncertainties .....	28
<b>5.</b>	<b>Temperatures and winds from meteor trails</b>	<b>31</b>
5.1	Formation and diffusion of meteor trails .....	31
5.2	Meteor radar temperatures .....	32
5.3	Zonal and meridional winds from meteor echoes .....	33
5.4	Uncertainties .....	35
<b>6.</b>	<b>Remote sensing from satellites</b>	<b>37</b>
6.1	Limb scanning .....	37
6.2	SABER temperatures and OH volume emission rates .....	37
6.3	Aura MLS temperatures .....	38
6.4	Uncertainties .....	39
<b>7.</b>	<b>Results</b>	<b>41</b>
7.1	Multi-instrument derivation of temperatures .....	41
7.2	Atmospheric coupling .....	45
7.3	OH layer altitude, radiance and temperature .....	46
7.4	Periodic variations and temperature trends .....	47
<b>8.</b>	<b>Concluding remarks and perspectives for the future</b>	<b>49</b>
	<b>References</b>	<b>51</b>

### Paper 1

Dyrland, M. E., and F. Sigernes (2007), An update on the hydroxyl airglow temperature record from the Auroral Station in Adventdalen, Svalbard (1980-2005), *Can. J. Phys.*, 85, 143-151, doi: 10.1139/P07-040. © 2007 Canadian Journal of Physics

### Paper 2

Dyrland, M. E., F. J. Mulligan, C. M. Hall, F. Sigernes, M. Tsutsumi, and C. S. Deehr (2009a), The response of OH airglow temperatures to neutral air dynamics at 78°N, 16°E during the anomalous 2003-2004

winter, *submitted to J. Geophys. Res.*, manuscript # 2009JD012726, June 2009. (*Revised version in press, J. Geophys. Res.*, Dec. 2009.

© 2009 American Geophysical Union)

### **Paper 3**

Mulligan, F. J., M. E. Dyrland, F. Sigernes, and C. S. Deehr (2009), Inferring hydroxyl layer peak heights from ground-based measurements of OH(6-2) band radiance at Longyearbyen (78°N, 16°E), *submitted to Ann. Geophys.*, manuscript # angeo-2009-119, June 2009. (*Revised version published, Ann. Geophys.*, 27, 4197-4205, Nov. 2009.

© 2009 Authors)

### **Paper 4**

Dyrland, M. E., C. M. Hall, and F. J. Mulligan (2009b), Improved estimates for neutral air temperatures at 90 km and 78°N using satellite and meteor radar data, *manuscript not yet submitted*, Sept. 2009. (*Revised version submitted to Radio Science*, Dec. 2009.)



# 1 Introduction

## 1.2 Atmosphere and climate

Understanding, predicting and eventually perhaps even modifying the processes related to climate change, have been some of the most important goals of the scientific communities around the world for the last couple of decades. Whether induced by human activity or not, the predicted changes of sea and atmospheric temperatures will have significant consequences for human society, economic activity and natural diversity as pointed out by the Intergovernmental Panel of Climate Change (IPCC) in their assessment reports (downloadable from <http://www.ipcc.ch/ipccreports/>). As a part of understanding the global energy budget of the Earth, knowledge about all sources, sinks and transport mechanisms of the atmospheric constituents is needed. Ground-based weather stations, tropospheric and stratospheric balloons, radars and satellites have provided input data to atmospheric models. However, there are limitations. Our globe is large and some geographical locations and atmospheric regions are less accessible than others.

One of these atmospheric regions is the mesosphere. Located between 50-100 km above ground, it is too high to reach by balloon and too low for in-situ satellite measurements. Rockets can fly through and measure atmospheric parameters in-situ, but these are expensive and few such measurements are available. Ground-based instruments do also have limitations. Radars depend on gradients and discontinuities in refractive indices that are usually not present in the mesosphere, and optical measurements suffer from variable transmission and cloud conditions. These difficulties have led to the mesosphere often being ironically referred to as “the igonorosphere”. Despite the somewhat pessimistic nickname, being able to model and measure the dynamics and coupling of this and other atmospheric regions from the surface and into the thermosphere, is considered highly important [Jarvis, 2001]. Large scientific resources have been and are still used to complete this task and to understand how atmospheric dynamics couple to solar and anthropogenic forcing [Haigh, 2006].

A fundamental parameter to monitor and understand the variation of is the temperature. The temperature of the uppermost part of the mesosphere can be

obtained from a variety of ground-based and satellite instruments monitoring phenomena occurring there [Beig *et al.*, 2003]. The upper part of the mesosphere is often referred to as the mesopause region (80-100 km). It has been highlighted as a key part of the atmosphere to monitor for climate change signals by The Network for the Detection of Mesopause Change (NDMC) (<http://wdc.dlr.de/ndmc/>). Many of the instruments measuring mesopause region properties are available at the Arctic archipelago Svalbard (~78°N). Since the early 1980s a spectrometer has been used to measure hydroxyl airglow spectra. From these spectra rotational temperatures have been derived and assigned as neutral air temperatures at the assumed peak of the hydroxyl layer at ~87 km [Sigernes *et al.*, 2003]. Temperatures at 90 km have also been deduced from measurements of meteor echo decay times made by a meteor wind radar at Svalbard [Hall *et al.*, 2006]. However, as we shall argue, both of these techniques have their limitations. Data from satellites provides a new perspective useful for assessment and validation of earlier studies and results. With our multi-instrument approach we aim to contribute to solve some of the unresolved scientific issues in this field of research.

## 1.2 Unresolved scientific issues

There are two main motivations for measuring and analyzing temperatures and airglow spectra from the polar mesopause region:

- 1) One of them is to look for trends that can be attributed to climate change, either naturally or anthropogenically induced. The observed increase of temperatures in the troposphere is expected to have its counterpart in a decrease of temperatures in the middle atmosphere (stratosphere and mesosphere) [Akmaev and Fomichev, 2000]. Models have predicted that a trend would be largest in the polar regions and that an observed temperature decrease there could be considered a signal of future climate change in other regions [Olivero and Thomas, 2001]. Beig *et al.* [2003] compiled estimates of mesospheric temperature trends from a variety of observations from ground-based instruments, rocketsondes, satellites, lidars etc, looking for such a trend. They did not find a consistent picture and many of the reported time series showed no significant temperature trend. Updated chemistry climate models (CCMs) which extend to above the mesopause region and in which influence from the 11-year solar cycle as well as anthropogenic forcing are incorporated, have been developed and evaluated [Schmidt *et al.*, 2006; Yuan *et al.*,

2008, and references therein]. Several of these confirm the existence of a near zero temperature trend at mesopause level [e.g. *Garcia et al.*, 2007]. Still, ground based and satellite measurements show large spatial and temporal asymmetry in the response of both the middle- and upper atmosphere to the forcing [e.g. *Chanin et al.*, 2006]. The question of the value and sign of a possible temperature trend is still not fully answered. These inconsistencies are the motivation for performing trend analyses of the long term time series of mesopause region temperatures from Svalbard and other places around the world. Our results are presented in *Paper 1*.

2) The second and main motivation for studies of mesopause region temperatures and airglow characteristics is simply to be able to parameterize and understand the state and dynamics of the Earth's atmosphere. Especially for the high Arctic winter ( $>75^{\circ}\text{N}$ ), models and measurements of parameters such as wind and temperature, diverge from each other [*Schmidt et al.*, 2006; *Hall et al.*, 2006]. The polar mesopause region is highly dynamic with large gradients in temperature and large variability in vertical, zonal and meridional circulation resulting from waves passing and breaking [*Holton*, 1983]. Analyses of periodicities in the temperature dataset can give clues about the connection towards variable solar input (*Paper 1*). Comparisons between data sets are highly useful for data validation purposes (*Papers 2 and 4*). Correlations with wind strength and direction indicate coupling mechanisms between atmospheric regions, and allow us to identify the processes responsible for observed temperature changes (*Papers 2 and 3*).

### **1.3 Structure of the thesis**

In addition to presenting our results we will also establish a background for the themes in this thesis.

Terms and concepts associated with the dynamics of the mesopause region, are presented in Chapter 2. Chapter 3 describes our site and the instruments used in our studies. In Chapter 4 we provide the background and theories for remote sensing of hydroxyl emissions and rotational temperatures. The basis for deriving mesopause region temperatures and winds from meteor radar measurements are given in Chapter 5. The satellite data are briefly described in Chapter 6. Chapter 7 summarizes the results and we discuss them in the context of previous work. Concluding remarks and perspectives for the future are given in Chapter 8. Finally,

the four papers that constitute the basis of this thesis are attached in manuscript form.

## 2 Middle atmosphere dynamics

### 2.1 The mesopause region defined

According to its characteristics at different altitudes, the atmosphere has been divided into different regions. Figure 1 shows a schematic of the mean thermal structure of the atmosphere and processes occurring there. The main divide is between the homosphere and heterosphere. The homosphere consists of mainly neutral constituents, while the heterosphere is ionized [Wayne, 2000]. The troposphere, stratosphere and mesosphere comprise the homosphere. In the homosphere gases are mixed by turbulent diffusion. The result is that molecules and atoms produce a homogeneous gas with even concentration and gradually varying temperature. In the heterosphere (thermosphere and exosphere) the mean free path between the gas molecules becomes large enough for molecular diffusion to control the vertical gas distribution. Gravitational effects separate the different gases from each other. Heavy gases accumulate at lower altitudes, while lighter gases become dominant at higher altitudes. Thus the mean molecular mass varies with altitude while in the homosphere it is constant [c.f. *Mueller-Wodarg et al.*, 2008]. The stratosphere and mesosphere are often termed the middle atmosphere. It is the middle atmosphere that is the study area of this thesis, and in particular we study the so-called mesopause region.

The mesopause is the boundary between the mesosphere and the thermosphere and it is the place where the atmospheric temperature is at its minimum. It is often referred to as a region rather than a certain altitude, since the actual mesopause changes height both on shorter (diurnal) and longer (seasonal and annual) time scales. The temperature minimum can also be two-leveled [e.g. *Thulasiraman and Nee*, 2002, and references therein]. In the following we will consider the altitude range 80-100 km as the mesopause region. At these heights the atmospheric pressure varies from approximately 0.01 hPa (80 km) to 0.001 hPa (97 km) [Wayne, 2000].

Some of the most important processes occurring in this region are illustrated in Figure 1. Two of these will be used as tracers of mesopause region dynamics in our study. These are the formation of the hydroxyl (OH) airglow layer at ~87 km and the ablation of meteors occurring at heights 70-110 km.

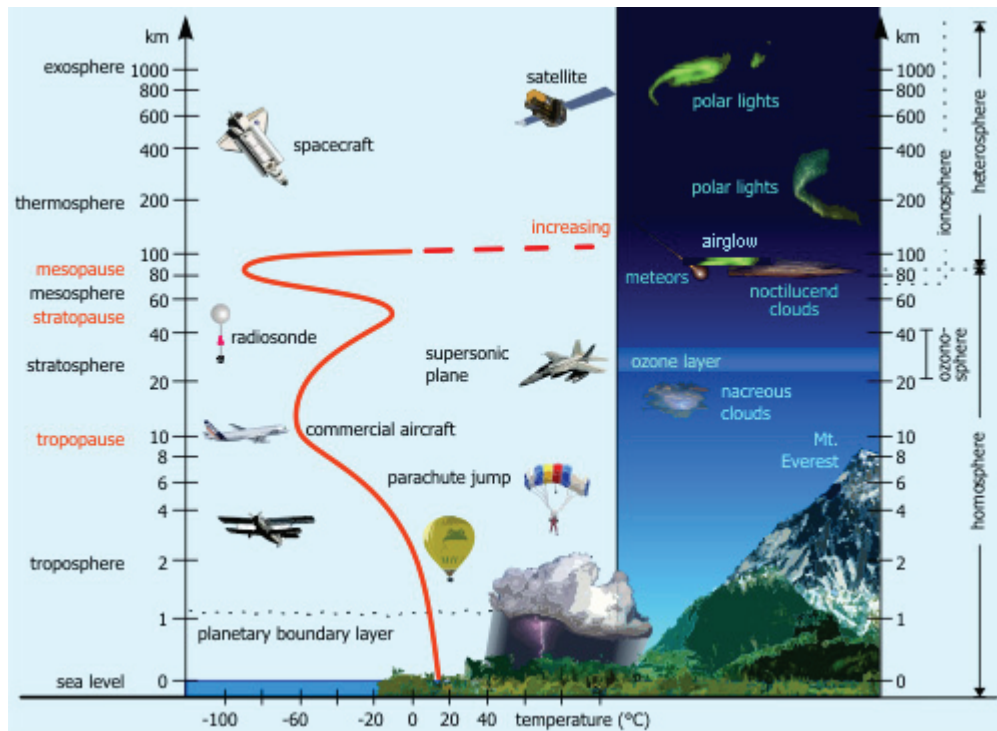


**Figure 1.** Illustration of the different regions of the Earth’s atmosphere and processes occurring at different altitudes (courtesy of Michael Wößner).

From remote sensing of these phenomena, parameters such as temperature and winds can be derived. These phenomena will be discussed more thoroughly in Chapters 4 and 5. The mesopause region is also home to noctilucent clouds (NLC) also known as polar mesospheric clouds (PMC), which occur during the polar summer when the mesopause region temperatures are very low [Gadsden and Schröder, 1989]. The associated polar mesospheric summer echoes (PMSE) can be detected by radars and their occurrences have been studied from Svalbard [Hall et al., 2009]. There are several scientific problems that can be addressed by studying NLC’s and PMSE. However, these will not be a subject of this work. The mesopause region is also a place where gravity- and planetary waves break and deposit energy [c.f. Holton, 1983] and precipitation of energetic particles during so-called solar proton events (SPEs) can also influence the composition and dynamics of the upper mesosphere strongly [Jackman et al., 2001].

## 2.2 Large-scale circulation

Latitude-height cross sections of zonal-mean temperature (upper panel) and wind (lower panel) for solstice are shown in Figure 2. The tropopause, stratopause and mesopause are marked by dashed lines. In the stratosphere there is a relatively uniform decrease of temperature from the summer to the winter pole, as expected by radiative equilibrium conditions [Holton, 2004].

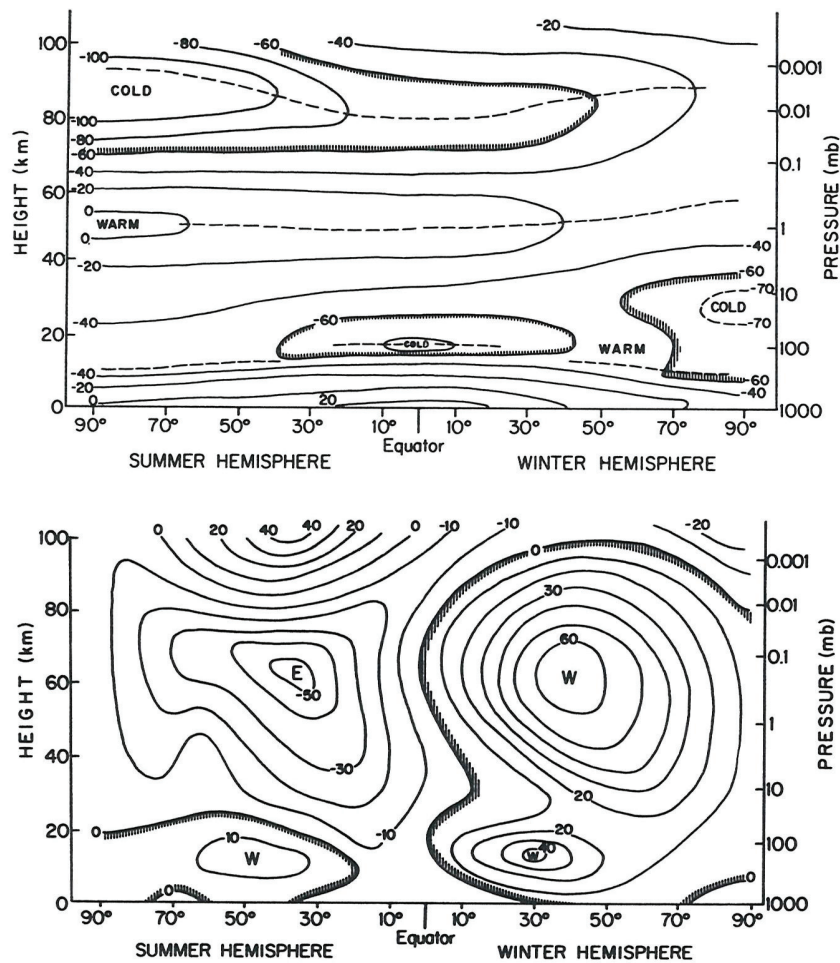


**Figure 2.** Schematic latitude-height cross sections of zonal mean temperatures ( $^{\circ}\text{C}$ ) (upper panel) and zonal mean wind ( $\text{ms}^{-1}$ ) (lower panel) for solstice conditions. Dashed lines indicate tropopause, stratopause and mesopause levels. W and E designate centers of westerly (from west) and easterly winds (from east), respectively (from *Andrews et al.*, 1987).

Above 60 km the sign of the gradient changes - the summer mesopause region is colder than the winter mesopause region (upper panel in Figure 2). The main features for the winds are an easterly (i.e. from the east or westward) jet in the summer hemisphere and westerly (i.e. from the west or eastward) jet in the winter hemisphere at 60 km (lower panel in Figure 2). At the lower stratosphere a cold region is seen poleward of 70°N for winter. This is the so-called polar vortex and its origin is the lack of solar radiation during polar night. The rapid decrease of temperature poleward of 45°N in winter requires a zonal vortex with strong westerly shear with height [Holton, 2004].

The mean zonal flow shown in the lower panel of Figure 2 arises from the balance between the pressure gradient force and the Coriolis force acting on parcels of air. If an air mass is transported upwards from its equilibrium level it will adiabatically adjust to the surrounding pressure by expanding its volume. The work required decrease the temperature of the air. This process is called adiabatic cooling. The opposite happens when air subsides. It is compressed and the temperature increases. This is called adiabatic warming.

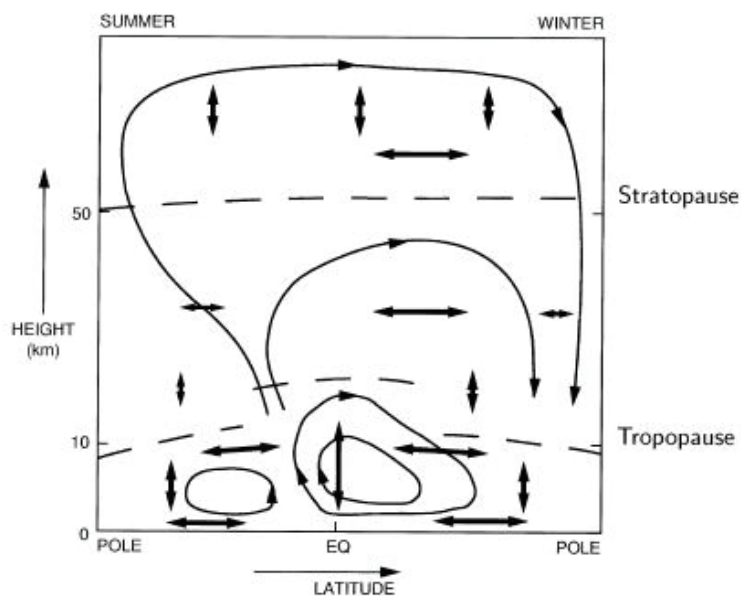


**Figure 3.** Schematic of the meridional circulation in the atmosphere (illustration by WMO 1985, adapted from Hoppe, 2001).

Due to the temperature/pressure gradients between the equator and higher latitudes, air will move northward from the Equator and the Coriolis force will induce a counterclockwise/eastward rotation in the northern hemisphere and oppositely in the southern hemisphere [e.g. *Andrews et al.*, 1987].

The departure from radiative equilibrium for the temperatures above 60 km altitude is caused by vertically propagating internal gravity waves which transfer momentum from the troposphere into the mesosphere. When the waves break they produce a strong zonal forcing which alters the strength of the zonal jet. By continuity this induces a meridional flow from the summer to the winter pole at mesospheric level [*Andrews et al.*, 1987]. Figure 3 shows a schematic of the meridional circulation in the atmosphere.

### **2.3 Heating and cooling processes**

We have already mentioned some of the processes responsible for heating or cooling certain parts of the atmosphere. Transport of air leads to adiabatic heating/cooling. In addition to ozone ( $O_3$ ) absorbing UV and warming the stratosphere, other atmospheric molecules and atoms also contribute to the thermal structure. Molecular oxygen ( $O_2$ ) causes heating by absorbing UV radiation in the upper mesosphere. The heating is balanced by radiative cooling mainly caused by vibrational relaxation in the infrared 15  $\mu\text{m}$  band of carbon dioxide ( $CO_2$ ) [*López-Puertas et al.*, 1992]. Water vapor ( $H_2O$ ) also adds to the cooling, but to a smaller degree compared to  $CO_2$  and  $O_3$  [*Kuhn and London*, 1969].

### **2.4 Sudden stratospheric warming and mesospheric cooling**

Figure 4 shows a schematic of the Arctic polar vortex. The temperature is low in the lower stratosphere vortex core, and it increases with radius from the axis of rotation. In the upper stratosphere and lower mesosphere vortex core, the temperature decreases by radius relative to a mean vertical temperature from 0-60 km [*Gerrard et al.*, 2002]. The low temperatures in the lower stratosphere are associated with radiative cooling during the polar night, while the high temperatures in the upper stratosphere and lower mesosphere are due to subsidence of air and adiabatic warming [*Duck et al.*, 1998]. The westerly (eastward) jet is shown as a green arrow.

Occasionally the polar stratospheric vortex breaks down over the course of a few days. This is accompanied by large-scale warming of the polar stratosphere known as a sudden stratospheric warming (SSW) [Schoeberl, 1978]. If both the zonal wind direction and temperature gradient at 10 hPa and 60°N reverse, the SSW is termed a *major* SSW. Major SSWs do not occur every year, but for the last decade they have been frequent. They occurred in 1999, 2001, 2002, 2003, 2004, 2006 and 2009 [Manney *et al.*, 2005; Manney *et al.*, 2009]. Studies show that enhanced propagation of planetary waves from the troposphere, especially zonal wave numbers 1 and 2, are closely associated with the SSWs [e.g. Shepherd *et al.*, 2007]. The planetary waves distort the polar vortex which may lead to a break-up or splitting of it. Sudden stratospheric warmings have been shown to be closely associated with negative temperature gradients in the mesosphere [e.g. Labitzke, 1972; Walterscheid, 2000; Pancheva *et al.*, 2008].

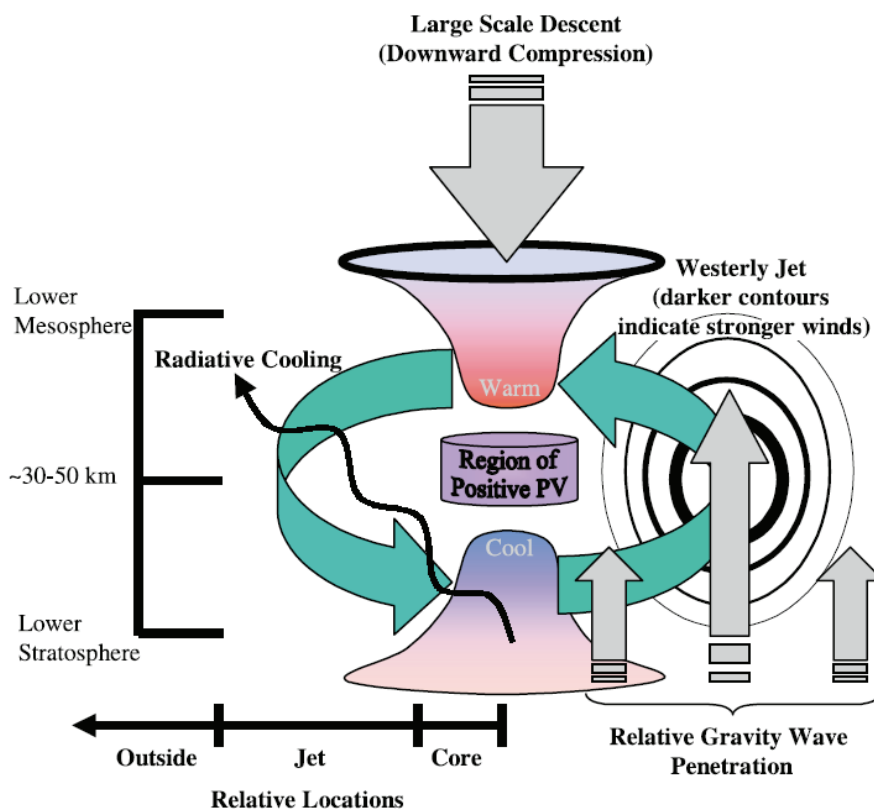


**Figure 4.** Schematic of the overall configuration of the Arctic polar vortex (from Gerrard *et al.*, 2002).

*Liu and Roble* [2002] studied SSWs in a model and concluded that the likely explanation for the temperature decrease is that the weakening and reversal of the polar vortex allows more propagating gravity waves into the mesosphere, forcing the meridional circulation to turn equatorward and thus leading to adiabatic cooling.

## 2.5 Short and long term variability

Following the nomenclature of *Azeem et al.* [2007] the temperature varies with time according to a number of reasons:

$$\begin{aligned} \text{Temperature} = \{ & \text{Solar cycle in temperature} \\ & + \text{annual variation in temperature} \\ & + \text{semi-annual variation in temperature} \quad (1) \\ & + \text{periodic terms} \\ & + \text{long-term trend in temperature} \\ & + \text{residual} \} \end{aligned}$$

The 11-year cyclic activity of the Sun has a large impact on the variability of Earth's environment and is also believed to influence the temperature of the middle atmosphere. Some studies have found a correlation between f10.7 solar flux and mesopause region temperature [e.g. *Azeem et al.*, 2007, and references therein], but other have found no dependence [e.g. *Sigernes et al.*, 2003]. In addition to the 11-year solar flux period there is also a shorter-term variation of solar flux due to uneven distribution of active regions on the Sun. These periods are close to the 27 day rotation period of the Sun [*Hall et al.*, 2006; *Paper 1*; *Höppner and Bittner*, 2009].

Temperatures in the mesopause region exhibit annual and semi-annual variations. In the northern hemisphere the temperature is warm during the winter and cold during the summer. The variation is quite close to a sinusoidal variation [e.g. *Hall et al.*, 2006; *Paper 4*], although with shorter periods imposed, especially during the winter. These sub-semi-annual periods of less than 6 months define the periodic terms. Long-term temperature trends also influence the temperature and the residual is the unexplained variability of the temperature time series. The cause of these can be gravity or planetary waves, diurnal or semi-diurnal tides or as we

show in *Paper 2*, meridional circulation variations. This way to parameterize the different variations in a time series also applies to the observed time series of other parameters, e.g the airglow emission rate [*Shepherd et al.*, 2006; *Paper 3*].

### 3 Site and instruments

#### 3.1 Site description

This study has utilized data from instruments mainly located at the high-latitude location Longyearbyen (78°N, 16°E) at the Svalbard archipelago (see Figure 5). Being located in the so-called High Arctic, Svalbard is a unique place for atmospheric studies. No other place in the world at such high latitude has a similar well developed research infrastructure, reasonable climate and is at the same time available for anyone by regular air traffic. Svalbard has historically been a site for scientific research.



**Figure 5.** Map of the Svalbard archipelago. Longyearbyen is marked as a red bullet. Svalbard's location in the Arctic is indicated to the right.

Measurements of the auroral spectrum were conducted as early as 1872 [Wijkander, 1874]. Since the late 1970s a series of optical instruments have been deployed close to Longyearbyen to measure the characteristics of the aurora and airglow. In the later years (late 1990s and early 2000) several radars were also put up at the same site, making multi-instrument studies possible [Röttger, 2000; Hall *et al.*, 2004]. In the beginning of this century a number of satellites were sent up and they have brought a new perspective and new knowledge of the mesopause region. In the following sections a very brief description is given of each instrument that is used in this thesis. More details may be found in *Papers 1-4*, and references therein.

### **3.2 The Ebert-Fastie spectrometer**

The Ebert-Fastie spectrometer was constructed by W. G. Fastie at John Hopkins University, Maryland at the beginning of the 1970s. The original design for the spectrometer was developed by Hermann Ebert in 1889, but since Fastie made significant improvements, the spectrometers were named after both and hence were from then on referred to as Ebert-Fastie spectrometers. In 1978 the Ebert-Fastie spectrometer named “1 m Silver Bullet” was brought to the Auroral Station in Longyearbyen from the Geophysical Institute, University of Alaska Fairbanks. Since 1983 it has been used to measure hydroxyl airglow spectra. Temperatures and intensities measured by the instrument have been extensively studied [Sigernes *et al.*, 2003, and references therein]. In the autumn of 2007 it was moved to the new optical observatory: The Kjell Henriksen Observatory (KHO).

Figure 6 shows the experimental setup of the 1 m focal length Ebert-Fastie spectrometer used for the OH measurements in this study and a picture of the instrument. Inside the instrument a 1 m focal length spherical mirror is placed at the bottom of the instruments. It reflects and collimates light from the entrance slit onto the plane reflective diffraction grating. The grating has 1200 grooves/mm. The diffracted light from the grating is focused by the mirror onto the exit slit. Both the entrance and exit slits are curved to remove the effect of astigmatism by the mirror and to improve the spectral resolution of the system [Fastie, 1952]. The spectrometer has a fixed field of view of approximately  $5^\circ$  centered on geographical zenith.

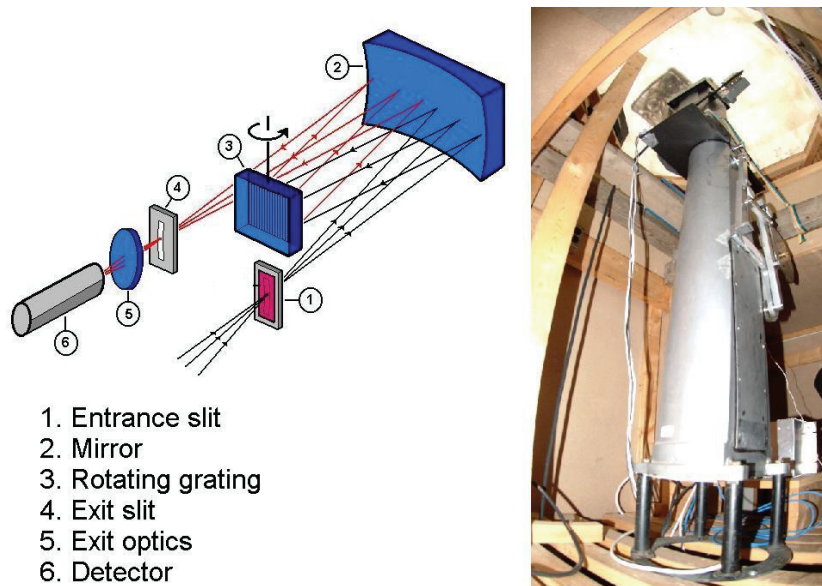


**Figure 6.** Photograph and schematic of the Ebert-Fastie spectrometer used in this study (courtesy of F. Sigernes).

Examples of OH spectra measured by the instrument and other specifications are given in Chapter 4 and in *Papers 1, 2 and 3*. The relative intensity of the observed OH airglow lines can be used to derive the temperature at the height of the OH layer [Kvifte, 1961]. These temperatures are referred to as rotational hydroxyl temperatures. The theory and practice behind the retrieval are thoroughly described in Chapter 4.

### 3.3 The NSMR meteor radar

The Nippon/Norway Svalbard Meteor Radar (NSMR) is located a few kilometers away from the optical site near Longyearbyen. It is owned by the National Institute of Polar Research (NIPR) in Japan and operates on an automated basis all year round. Figure 7 shows a picture of the radar.

The radar has been described in several papers [e.g. *Hall et al.*, 2004; *Hall et al.*, 2006]. The Nippon/Norway Svalbard Meteor Radar (NSMR) consists of one transmitter antenna and five receivers. Echoes from meteor trails illuminated at 31 MHz are detected by the 5-antenna interferometer array.

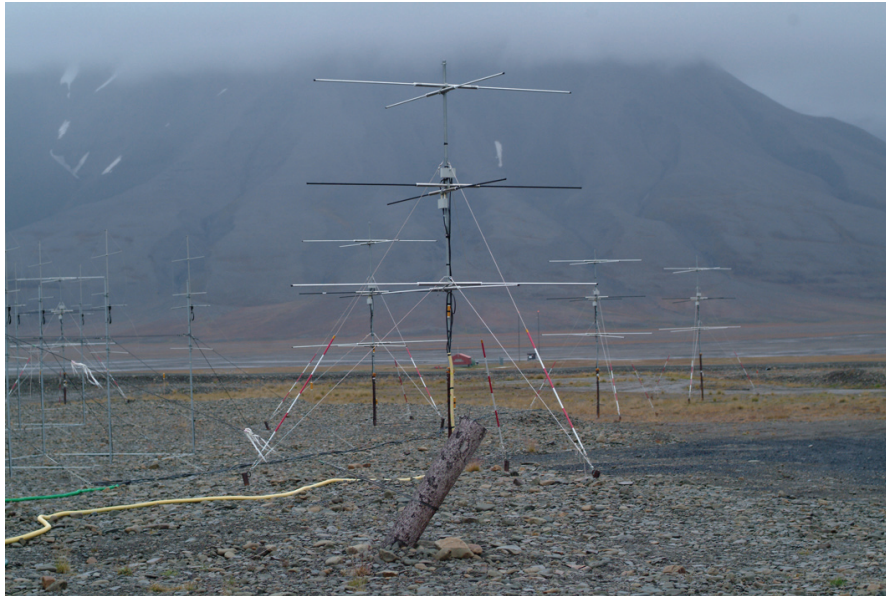


**Figure 7.** The Nippon/Norway Svalbard meteor radar (NSMR) located in Adventdalen, Svalbard. Part of the Sounding System radar (SOUSY) can be seen in the background (photo: F. Sigernes).

The phase differences of the signals received by the receiving antennas are used to determine the location of the meteor in the sky. The range resolution is 1 km, and the height resolution is therefore of the same order, depending on the spatial distribution of echoes within the field of view. The fading times of echoes measured by the radar are employed for estimation of the ambient neutral air temperature at 90 km altitude. Doppler shift of the echoes measured by the five receiving antennas provides zonal and meridional winds. The basis for the temperature and wind retrieval is given in Chapter 5. Winds and temperatures measured by NSMR are used and discussed in *Papers 2* and *4*.

### **3.4 TIMED SABER**

The satellite TIMED (Thermosphere Ionosphere Mesosphere Energetics and Dynamics) was launched in 2001. It has a circular orbit at an altitude of 625 kilometers. The SABER (Sounding of the Atmosphere using Broadband Emission Radiometry) instrument is a ten channel multi-channel radiometer (1.27-16.9  $\mu\text{m}$ ). Once every 58 seconds SABER scans up and down Earth's horizon and data from

an altitude range of ~180 kilometers are obtained [Russell *et al.*, 1999]. Figure 8 show where the SABER instrument is located at the TIMED spacecraft.

Temperatures and hydroxyl volume emission rates are two of the data products that are obtained from these scans and that we have made use of. Further descriptions of the instrument and data are given in Chapter 6 and in *Papers 2, 3* and *4*.

### 3.5 Aura MLS

The Microwave Limb Sounder (MLS) was launched on the Earth Observing System (EOS) Aura spacecraft in 2004. From its orbit at ~705 km it measures microwave thermal emissions centered near 118, 190, 240, 640 and 2250 GHz from the limb (edge) of Earth's atmosphere. It views forward along the flight direction of Aura [Schoeberl *et al.*, 2004].

The 118 Hz radiometer provides temperatures which is the data product used in our study. In the following chapters and in *Paper 4* we refer to the instrument as Aura MLS.

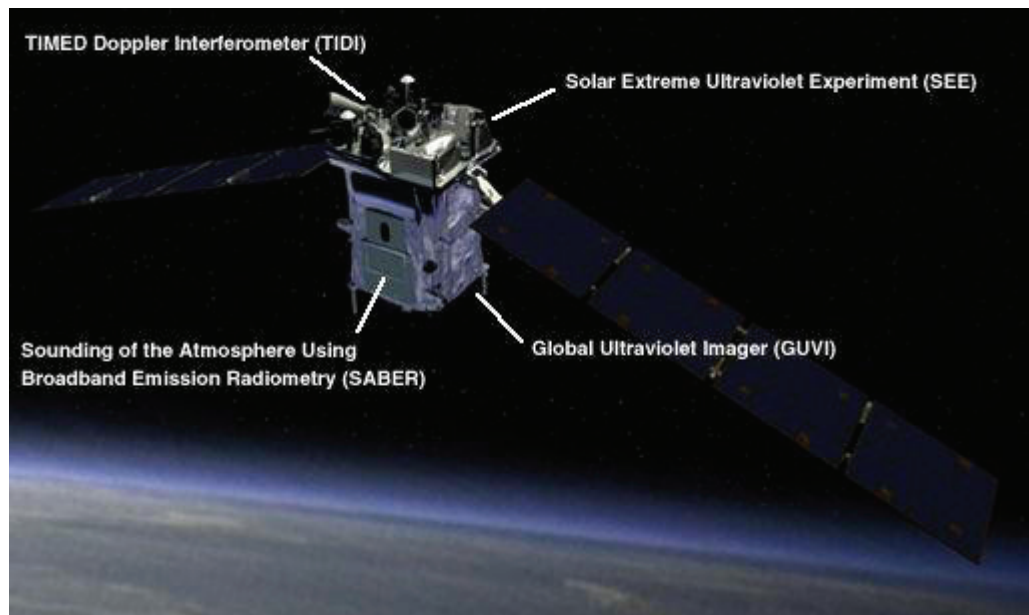


**Figure 8.** Artist rendering of the TIMED spacecraft. The position of SABER on the satellite is shown down to the left (credit: NASA).

This is done to avoid confusion with its predecessor UARS MLS (Upper Atmosphere Research satellite Microwave Limb Sounder) which operated between 1991 and 2001. Figure 9 shows a schematic of the field of views of the different instruments on board Aura. The MLS instrument parts are shown to the right. Temperatures retrieved from Aura MLS are used extensively in *Paper 4*. A brief description of the data retrieval is given in this paper and in Chapter 6.

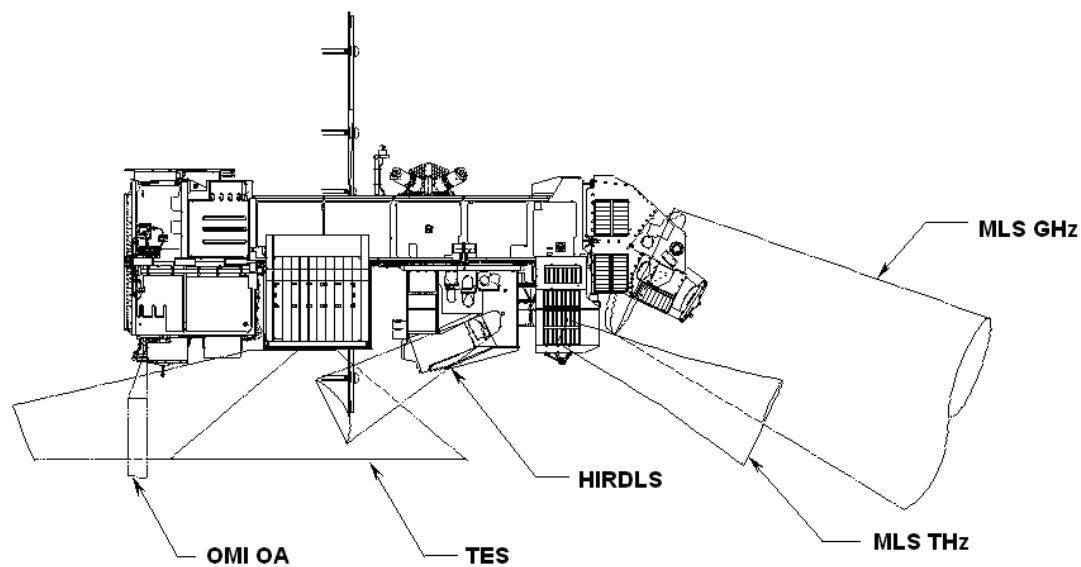


**Figure 9.** Schematic of the Aura instrument's field of views. MLS instruments are located at the right (credit: Aura @ NASA ).

## 4 Remote sensing of hydroxyl airglow

### 4.1 Airglow emissions

Airglow is the common name of weak emissions of light from the sky having its origin in atmospheric photochemical processes. According to the time of day that airglow is observed, it is termed dayglow or nightglow [Chamberlain, 1961]. There are three major classes of visible nightglow emissions in the mesopause region: (1) the atomic and molecular emissions of oxygen, (2) the emissions of metallic atoms such as sodium, calcium, potassium and magnesium, and (3) emissions from the vibrational-rotational bands of hydroxyl ( $\text{OH } X^2\Pi$ ). The energy source for these emissions is the absorption of solar UV radiation by molecular oxygen which produces atomic oxygen. Diffusion processes bring the atomic oxygen down to the mesopause region, where reactions form ozone, OH and active states of molecular oxygen [c.f. Meriwether, 1989]. Figure 10 shows an image of red and green oxygen airglow photographed from the International Space Station (ISS).

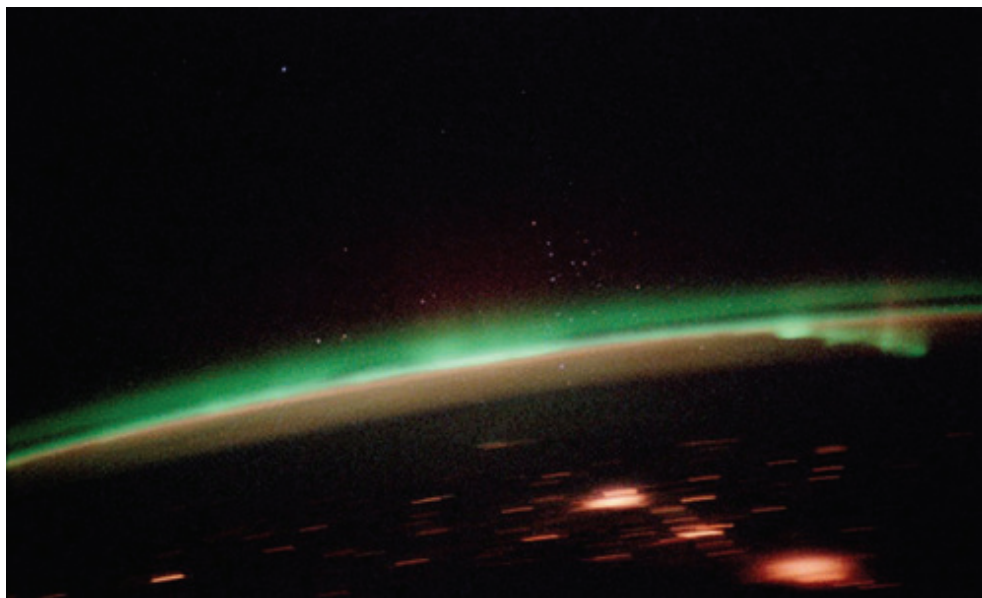


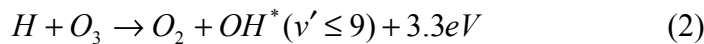
**Figure 10.** Green and red airglow emitted by excited oxygen photographed from the International Space Station (ISS). The blurry orange-red lights are city lights from Earth (photo: Don Pettit, ISS-6, NASA).

The green oxygen line has been known as a nightglow radiator for nearly 150 years [*Ångström*, 1869]. The airglow emissions in the non-visible infrared wavelength range were not observed until the 1930s [*Herzberg*, 1934, and references therein]. The airglow spectra investigated in this thesis are nightglow spectra emitted by vibrationally excited hydroxyl radicals and the wavelength range studied is in the near-infrared part of the spectrum ( $\sim 8400$  Å). Following *Sivjee* [1992] we denote them  $OH^*$  clarifying that we are talking about the vibrationally excited OH X<sup>2</sup>Π ground state. Unfortunately, this has not been done consistently throughout the papers. When we refer to airglow in the following, we mean nightglow emissions and we will use the terms *hydroxyl*-, *OH*- and *OH\** *airglow* semi-randomly.

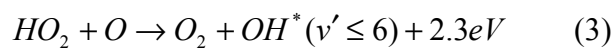
The theories behind the formation of these spectra are the basis for the retrieval of rotational hydroxyl temperatures. These are the key data in our *Papers 1, 2* and *3*. In the following paragraphs we therefore present the theoretical background and discuss the approach we have used to obtain these temperatures.

## 4.2 Mechanism for hydroxyl airglow

The hydroxyl airglow was first identified by *Meinel* [1950] and is referred to as the Meinel bands of OH. They consist of several wavelength bands between 3800-50000 Å. *Bates and Nicolet* [1950] identified the main mechanism for the production of vibrationally excited  $OH^*(v')$  near the mesopause:



$v'$  indicates the upper vibrational level. This is the main mechanism for hydroxyl airglow [*Sivjee*, 1992], but a second mechanism is also important in the polar night above Svalbard according to *Sivjee and Hamwey* [1987]. Based on observed differences in OH(6-2) intensities observed above Svalbard compared to lower latitudes [*Llewellyn et al.*, 1978] they suggest that the  $HO_2$  abundance is higher at higher latitudes where there is no photodissociation of molecular minor constituents. Thus the following reaction may be the source of up to half of the  $OH^*(v' = 6)$  in polar night regions:



The production of  $OH^*$  has a peak at altitudes of 80-90 km above ground. Above this height the production is limited by the rapid fall off in ozone concentration and below it is limited by the onset of rapid quenching of the excited products by collisions more frequent at the higher atmospheric pressures [Chamberlain, 1961]. The balance between the two processes creates the narrow OH airglow layer. Rocket measurements have found a normal peak altitude of ~87 km and a width of 8 km [e.g. Baker and Stair, 1988]. Ground-based instruments measure column integrated emission rates from the full atmospheric layer they view through, and thus no height information is available. Liu and Shepherd [2006] developed an empirical model for the altitude of OH airglow emissions based on simultaneous satellite and ground-based measurements of OH volume emission rates. The result was a model that may be applied to ground station observations. However, since the satellite they used only covered the latitude range 40°S-40°N, this is also the assumed valid range of that empirical model. Therefore it is customary to use the value of Baker and Stair [1988] as the altitude of the OH emissions.

### 4.3 OH molecular spectra and the rotational temperature

The hydroxyl molecule is a so-called diatomic molecule formed by two atoms. The theory behind the formation of the emission spectra of diatomic molecules is described by Herzberg [1950]. The energy of a diatomic molecule is a total of the energy of the electronic configuration ( $E_e$ ), the nuclear vibration ( $E_v$ ) and the nuclear rotation ( $E_R$ ). Each of these are quantized and light is emitted as a result of vibrational-rotational transitions at certain levels. The energy difference of a transition between an upper and lower molecular state determines the wavelength of the emission and can be expressed as:

$$\Delta E = hc / \lambda = \Delta E_e + \Delta E_v + \Delta E_R. \quad (4)$$

Since the OH in the upper mesosphere is in its translational ground state  $X^2\Pi$ , the wavelength of the emission can be formulated [Herzberg, 1950]:

$$\lambda = \frac{hc}{E_{v'} - E_{v''} + E_{v''} - E_{v'}} = (G(v') - G(v'') + F(J', v') - F(J'', v''))^{-1}, \quad (5)$$

where  $G(v)$  is defined as the vibrational term in vibrational state  $v$  and  $F(J, v)$  is the rotational term in rotational state  $J$  and vibrational state  $v$ . The single prime indicates the upper state and the double prime indicates the lower state. The vibrational term is determined from the formula:

$$G(v) = \omega_e(v+1/2) - \omega_e x_e (v+1/2)^2 + \omega_e y_e (v+1/2)^3 - \omega_e z_e (v+1/2)^4 + \dots \quad (6)$$

$\omega_e$  is and  $x_e$  are the vibrational constants calculated by *Chamberlain and Roesler* [1955]. They are given in Table 1.

**Table 1.** Vibrational constants from (from *Chamberlain and Roesler* [1955]).

$\omega_e$	$\omega_e x_e$	$\omega_e y_e$	$\omega_e z_e$	$\omega_e q_e$
3737.90	85.965	0.5398	0.01674	-0.001637

There are two different rotational terms. Those come from the fact that the electron spin can be either up or down, and they are designated  $X^2\Pi_{3/2}$  and  $X^2\Pi_{1/2}$ . There is also a splitting due to so-called  $\Lambda$ -doubling which is an effect of the rotation of the nuclei [*Krassovsky et al.*, 1962]. Due to the limited band pass of the spectrometer used, this is of little importance for the analysis of our measurements.  $\Lambda$ -doubling is therefore neglected. The two rotational terms important are thus:

$${}^2\Pi_{3/2} : F_1(J) = B_v \left[ (J+1/2)^2 - 1 - 1/2 \sqrt{4(J+1/2)^2 + Y_v(Y_v - 4)} \right] - D_v J^4 \quad (7)$$

$${}^2\Pi_{1/2} : F_2(J) = B_v \left[ (J+1/2)^2 - 1 + 1/2 \sqrt{4(J+1/2)^2 + Y_v(Y_v - 4)} \right] - D_v J^4 \quad (8)$$

$B_v$ ,  $Y_v$  and  $D_v$  are functions of the vibrational state. These are calculated by *Hill and van Vleck* [1928] and the numbers relevant for the OH(6-2) transitions are given in Table 2 (from the paper by *Krassovsky et al.* [1962]).

Transitions between different vibrational levels are denoted  $OH(v' - v'')$  bands, where  $v'$  is the upper state and  $v''$  the lower. Only certain rotational transitions are possible. The selection rules limits them to transitions where  $\Delta J = -1, 0$  or  $1$ . These transitions give rise to the P-, Q- and R-branches of the vibrational bands.

**Table 2.** Rotational constants from *Krassovsky et al.* [1962].

Rotational constants	$v=6$	$v=2$
$B_v$ (cm <sup>-1</sup> )	14.349	17.108
$D_v$ (cm <sup>-1</sup> )	0.0018	0.0018
$Y_v$	-9.795	-8.214

Rotational transitions in the X<sup>2</sup>Π<sub>3/2</sub> state are identified with subscript 1 (P<sub>1</sub>, Q<sub>1</sub> and R<sub>1</sub> lines), while those in the X<sup>2</sup>Π<sub>1/2</sub> state are called P<sub>2</sub>, Q<sub>2</sub> and R<sub>2</sub> lines.

The intensity of a line in photons/s is a product of the number of molecules in the upper state  $N$  and the transition probability  $A$  to end up in the lower state:

$$I_{v',J' \rightarrow v'',J''} = N_{v',J'} A(v',J' \rightarrow v'',J'') \quad (9)$$

Assuming that the OH\* molecules are in thermodynamical equilibrium the distribution of rotational levels in a certain vibrational state  $N_{v',J'}$  can be defined by the Boltzmann distribution. This assumption is validated by the relatively long radiative lifetime of OH\* allowing the molecules to undergo several collisions and be thermalized at the kinetic temperature [Sivjee, 1992]. In thermodynamical equilibrium, the number of molecules in the upper state can be expressed like this:

$$N_{v',J'} = \frac{N_0(v') 2(2J'+1) e^{-\frac{F(J')hc}{kT_{rot}}}}{Q_R}, \quad (10)$$

where  $N_0$  is the population of the lowest rotational level,  $k$  is the Boltzmann constant,  $c$  is the speed of light,  $h$  is the Planck constant,  $T_{rot}$  is the rotational temperature,  $Q_R$  is the partition function and  $F(J')$  is the upper rotational term. Combining Equations 9 and 10 and taking the logarithm gives:

$$\ln \left\{ \frac{I_{v',J' \rightarrow v'',J''}}{2(2J'+1) A_{v',J' \rightarrow v'',J''}} \right\} = \ln(N_0 / Q_R) - \frac{F(J')hc}{kT_{rot}} \quad (11)$$

$A_{v',J' \rightarrow v'',J''}$  is the transition probability between the states producing the particular line, also known as Einstein coefficients.

$Q_R$  can be expressed as:

$$Q_R = 1 + 3 \exp\left(\frac{-2B_v hc}{kT_{rot}}\right) + 5 \exp\left(\frac{-6B_v hc}{kT_{rot}}\right) + \dots = \frac{kT_{rot}}{B_v hc} \quad (12)$$

So both  $N_0$  and  $Q_R$  are functions of the rotational temperature, but constant for all the lines in a band. Plotting  $\{I/2(2J'+1)A\}$  against  $F(J')$ , where  $I$  and  $A$  are the measured intensity and transition probabilities for the different rotational lines should yield a straight line and is referred to as a Boltzmann plot (c.f. *Paper 1*).

Note that the assumption of thermodynamical equilibrium might be false for rotational levels above  $J'=5$  [Pendleton *et al.*, 1993]. Recent analysis of high-resolution night-sky spectra from the telescope Keck show that rotational temperatures derived from low- $J$  emission intensities show a strong dependence on vibrational level [Cosby and Slinger, 2007]. Care should therefore be taken before interpreting the OH temperatures from any band as absolute neutral air temperatures.

#### 4.4 Data handling

The OH(6-2) band are the emissions resulting from the transition from vibrational level  $v' = 6$  to  $v'' = 2$ . The emissions of this band are in the range from 8280-8600 Å. The temperature retrieval algorithm has been described in earlier papers [Sigernes, 2003] and *Papers 1, 2* and *3*. However, we will present some more details and discussions here.

The top panel of Figure 11 shows a typical raw spectrum for the Ebert-Fastie spectrometer when there are few clouds and relatively low auroral activity. The bulge close to the  $P_2(4)$  line is the auroral line OI 8446, but here it is very weak. The bulge around 8200 Å results from scattered city lights from Longyearbyen nearby. A single spectrum is obtained each 25 seconds and the integration time per bin is 65.54 msec. Due to limited data storage capacities, the data used in this thesis were stored as averages of 10 scans. The temperature retrieval starts with the process of hourly averaging the spectra, i.e. all spectra obtained during one hour are averaged and a resulting counts/integration time spectrum is the result. This is done to get the noise as low as possible. This is accordance with Bittner *et al.* [2002] who argue that 0.5-1 hour time intervals for integration are optimal. Before the

temperature retrieval, poor spectra are removed. Poor spectra may result from times when the background is extremely high due to light scattered by clouds or during high auroral activity [Myrabø *et al.*, 1987]. Some spectra may also have noise spikes that make temperature retrieval from them impossible. The spikes are probably due to strong electric pulses coming through the electrical system, or even cosmic rays.

The first step in the procedure is to wavelength calibrate the measured spectrum. The temperature retrieval continues by interpolating the raw spectrum to 1 Å resolution. The resulting spectrum is seen in the lower panel of Figure 11. The interpolation is done to match the resolution of the synthetic and measured spectrum. The wavelength range we analyze is indicated by a pink dashed rectangle in both panels. The bandpass of the spectral lines of the synthetic fit is chosen after visual inspection of one of the good quality raw spectra. The temperature from the last run of the program is used to construct an initial synthetic spectrum.

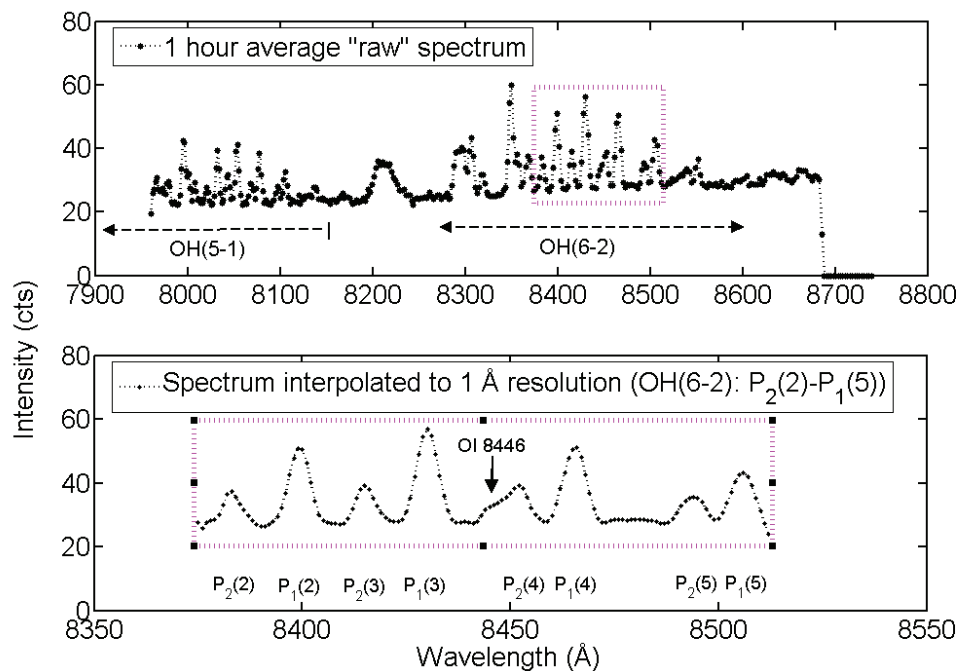


**Figure 11.** Top panel: An hourly averaged “raw” spectrum from the spectrometer. Bottom panel: The measured spectrum after being interpolated to 1 Å resolution. The bulge close to the P<sub>2</sub>(4) line is contamination by the auroral line OI 8446.

The background points are chosen as those not part of the wavelength ranges of the different rotational lines. Next, a linear fit to the background values is found which is used to subtract the background from the peak values of the rotational lines. The resulting intensities of the P<sub>1</sub> and P<sub>2</sub> lines are plotted in a Boltzmann plot. The temperature is found from the slope of the best fit to the P<sub>1</sub> intensities. The output values of our analysis program are hourly averaged temperatures, background level and slope, covariance between the measured and synthetic spectrum, variance of P<sub>1</sub> and P<sub>2</sub> lines from the linear fit of the Boltzmann plot (*Paper 1*) and the relative intensity (*Paper 3*). Based on criteria specified in *Papers 1-3*, certain hourly averaged spectra were considered “good quality data”. The rest was discarded from further analysis.

#### 4.5 Choice of transition coefficients

There are several sets of transition coefficients available for the OH Meinel system. For temperature retrieval from spectra measured in Longyearbyen, Svalbard (78°N), the Mies-values [*Mies, 1974*] have been used since the early 1980s for the purpose of trend analysis. However, these have by several authors been shown to yield the wrong absolute temperature, but since the original spectra up until 1991 are missing, they are still used since the object has been to look at relative variations anyway.

Sometimes it is useful to look at “absolute” temperatures, e.g. when comparing or validating data from other instruments and it is therefore a goal to identify the set of coefficients that is “most accurate” to date. *Cosby and Slanger [2007]* made a thorough comparison of the transition coefficients of *Mies [1974]* (Mies), *Langhoff et al. [1986]* (LWR), *Turnbull and Lowe [1989]* (TL), and *Goldman et al. [1998]* (GSG), and found the coefficients of *Goldman et al. [1998]* are to be preferred for  $J < 10$ . However, other papers have concluded differently. *French et al. [2000]* concluded the LWR fits the experimental OH(6-2) data best.

The question of which set is the best has not been a major theme for this thesis. However, we did a very basic test of just choosing an OH-spectrum with a minimum of auroral contamination. Table 3 shows the result using the different sets of transition coefficients in our temperature analysis program. In addition to those tested by *Cosby and Slanger [2007]*, we also included a recent set of coefficients by *van der Loo and Groenenboom [2007]* (LG).

**Table 3.** The fit parameters for the OH(6-2) hourly averaged spectrum from 31.1.2004

Coefficient set	Covariance	Variance $P_1$	Variance $P_2$	$T_{rot}$ (K)
Mies	0.97203	0.00075	0.00916	235
LWR	0.97205	0.00090	0.00895	230
TL	0.97183	0.00075	0.00619	243
GSG	0.97203	0.00078	0.00855	236
LG	0.97207	0.00084	0.01529	243

The spectrum chosen was from 31 January 2004 and it was an ~hourly averaged spectrum from ~01 UT. All the sets yielded relatively good fits. The *covariance* is the fit between the measured and synthetic spectrum. *Variance  $P_1$*  and  *$P_2$*  is the variance of the  $P_1$  and  $P_2$  values from the linear fit in the Boltzmann plot.  $T_{rot}$  (K) is the rotational temperature obtained from the slope of the line in the Boltzmann plot.

Panel a) of figure 12 shows the measured spectrum and the various synthetic spectra computed with the different transition coefficients. Panel b) shows the top of the  $P_2(3)$  line (inside the pink dashed square in panel a) to visualize the difference between the transition coefficients, which is not so obvious in panel a).

## 4.6 Calibration

The calibration procedure and functions are thoroughly described in *Paper 1*. Intensity calibrations were performed approximately every two years after 2001, however it should be emphasized here that the OH temperatures reported in *Papers 1-3* were all retrieved from spectra that were not adjusted according to the intensity calibration. In *Paper 1* calibration coefficients from 1980, 2002 and 2004 were shown to re-assure that the instrument sensitivity was relatively stable, and an error relating to the non-stability of the instrument was estimated (3%). This is the same approach that *Sigernes et al.* [2003] used when analyzing the former part of the time series.

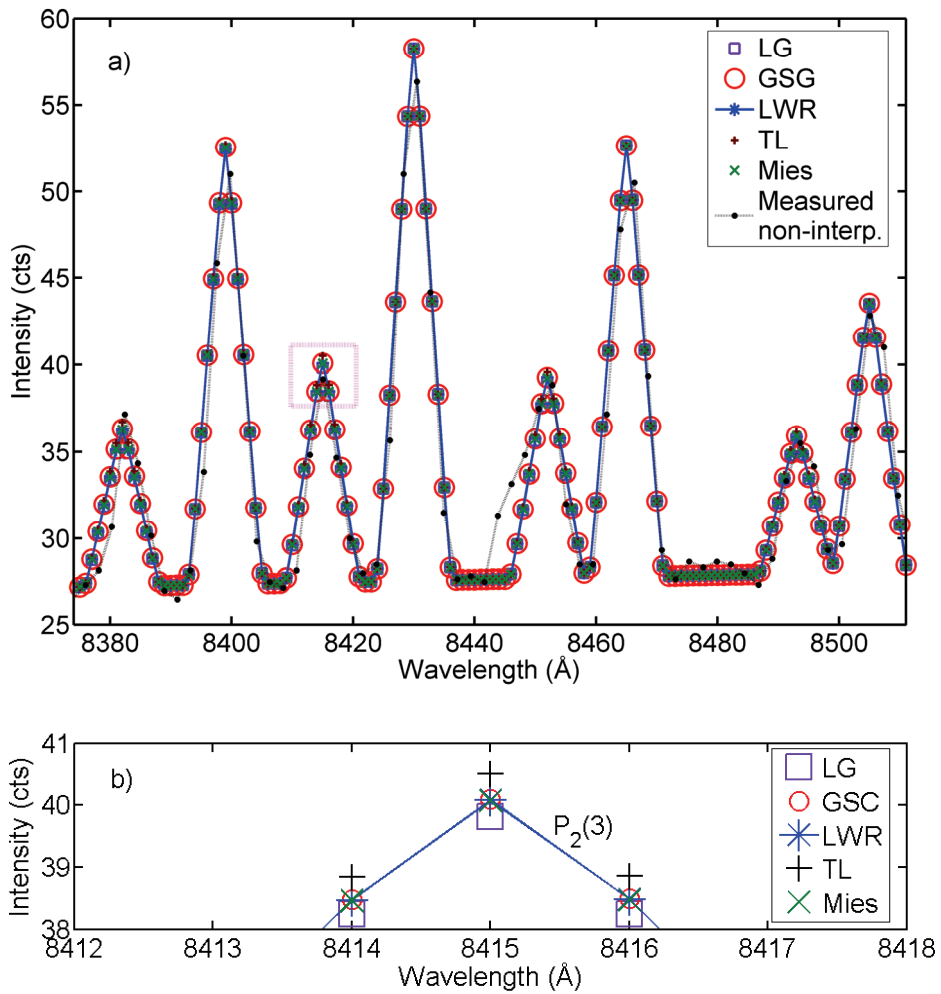


**Figure 12.** Panel a) Synthetic spectrum calculated by the use of different transition coefficients and with the background values from the measured hourly averaged spectrum from 31 January 2004 at 01 UT. Van der Loo and Groenenboom – purple squares; Goldman et al. – red circles; Langhoff et al. – blue stars and line; Turnbull and Lowe – black plusses; Mies – green crosses; measured raw spectrum – black bullets and dotted line. Panel b) Same as above, but zoomed in on the  $P_2(3)$  line (inside the pink dashed square in panel a) to visualize the difference between the transition coefficients.

The choice is reasonable since the temperatures are retrieved from the relative intensities of the OH(6-2) lines. As long as the calibration function is relatively constant throughout the wavelength interval and the slope of the calibration function does not change much over the years, we conclude that the instrument is operating stably.

#### 4.7 Uncertainties

The uncertainties of the temperature retrieval technique described above have been evaluated by previous authors studying the rotational OH(6-2) temperatures from Svalbard. *Myrabø* [1986] estimated it to be  $\pm 3\text{K}$  due to uncertainties in determining the background continuum. Those estimates were made using a 1/2m focal length spectrometer and with a setup corresponding to a spectral resolution of  $7 \text{ \AA}$ . The band pass of the raw data used in our study (data from 2001-2005) is  $\sim 6 \text{ \AA}$ . Thus we adopt *Myrabø's* value for the estimate of the uncertainty in determining the background.

*Sivjee and Hamwey* [1987] discussed the mechanisms that can be responsible for the deviation of the temperatures from an observed mean. Potentially they are: (1) errors in the relative transition probabilities, (2) errors related to relative instrument response, relative atmospheric transmission, relative level of background light intensity and statistical variations in rotational line intensities, and (3) periodic variations in temperature due to tides and gravity waves, and long term variations due to other atmospheric effects. We have not considered all of these in detail. However, we ran some tests with the spectra being calibrated and non-calibrated. It should also be noted that the calibrations were performed outside and not always under optimal weather conditions and this gives large uncertainties in these numbers. This is especially relevant for the 2002 calibration. *Sigernes et al.* [2003] state that the uncertainty in the calibration procedure is 5%. The fractional difference between calibrated and non-calibrated values are of the same order if we compare the calibration functions for 2002 and 2004 displayed in Figure 2 in *Paper I* to one where the slope and intercept is 1. The slope of the calibration functions gives rise to a up to 10 K difference in temperature when using our analysis program on calibrated and non-calibrated data. We will consider this a reasonable estimate for the uncertainty associated with the relative instrument response.

To estimate the total uncertainty of rotational OH(6-2) temperature we take the root-mean-square of the differences found in the sections above. The resulting uncertainty is of the order of  $\pm 10\text{K}$ . It should be noted that this is an estimate valid for the temperatures used in this thesis, i.e. data from 2001-2005, not before or later when other setups of the instrument have been used.

## 5 Temperatures and winds from meteor trails

### 5.1 Formation and diffusion of meteor trails

Meteors are small fragments of sand and dust and occasionally larger objects, entering the Earth's atmosphere at speeds of 12-72 km/s. Their source is debris floating around the solar system such as remnants of long-gone comets or asteroids. Most meteors are very small, typical grains span just a few tenths of a millimetre and weigh less than  $10^{-4}$  grams. When a meteor impinges on the Earth's atmosphere, it interacts with the neutral atmosphere and ablates meteor atoms. Collisions between the ionized atoms and atmospheric molecules are frequently repeated to slow the ions down to the thermal velocities of the environment neutral atmosphere within less than a millisecond [McKinley, 1961].

The resultant ionized trail has an initial radius,  $r_0$ , that can be approximated based on results from simultaneous multi-frequency radar studies [Cervera and Elford, 2004]:

$$\log_{10} r_0 = 0.0194h - 1.96 + 0.6 \log_{10}(V / 40), \quad (13)$$

where  $r_0$  is in meters, and  $h$  and  $V$  are altitude in km and initial velocity in km/s.  $r_0$  is 0.61 at 90 km at 40 km/s. The higher the trail lies, the larger the initial radius becomes because of fewer collisions.

Meteors are characterized according to the number of electrons per unit length along the trail - the so-called line-density denoted  $q$  [McKinley, 1961]. Meteors with line densities  $q < 10^{14}$  per meter are called underdense meteors and are the ones analyzed in this study. The ionized trail of an underdense meteor has a plasma frequency that is higher than the frequency of a radio wave. The radio wave can thus penetrate into the meteor trail and be scattered by each electron. Underdense echoes show fast rise times ( $< 0.1$  seconds), generally exponential decay and have lifetimes less than  $\sim 0.4$  s. Overdense echoes have line densities  $q > 10^{15}$  per meter. Radio waves are reflected off the surface of the trail and they have lifetimes that exceed 0.4 seconds, often leading to a oscillatory type of decay and they are not so useful for scientific purposes (Hocking, lecture notes).

After their formation meteor trails expand in the radial direction mainly due to ambipolar diffusion. Ambipolar diffusion is diffusion of positive and negative particles in a plasma at the same rate due to their interaction via the electric field. The meteor trail is further moved by wind motion of the ambient neutral atmosphere. There are also other factors that influence the diffusion of meteor trails and we will discuss them in Section 5.4. The free electrons of the meteor trail scatter incident radiation through the trail. An expression for the amplitude of the scattered radiation is given by *McKinley* [1961]:

$$A \propto 2\pi \int_0^{\infty} n_e(r,t) r J_0\left(\frac{4\pi r}{\lambda}\right) dr, \quad (14)$$

where  $n_e(r,t)$  is the density of the free electrons in the trail,  $r$  is the distance from the axis of the trail,  $t$  is the time since the trail formed,  $\lambda$  is the wavelength of incident radiation, and  $J_0$  is a zero-order Bessel function. Assuming the ionized trail diffuse outward at a rate determined by the local temperature and pressure, the backscattered radio amplitude from an underdense trail decreases exponentially with time. This is called ambipolar diffusion. Assuming a Gaussian initial distribution of electrons, the decay of the signal amplitude can be expressed as:

$$A(t) = A_0 \cdot e^{\left(-\frac{16\pi^2 D_a t}{\lambda^2}\right)} \quad (15)$$

$D_a$  is the ambipolar diffusion coefficient,  $\lambda$  is the radar wavelength and  $t$  is time. The equation shows that the duration becomes dramatically longer by using a radar with a lower radio frequency.

Meteor trails often drift due to high altitude winds, which cause a Doppler shift of the reflected signal. This Doppler shift can be used to measure wind direction and strength.

## 5.2 Meteor radar temperatures

The decay of the radar signal can be used to infer the temperature of the neutral atmosphere. For the most common meteors, the underdense meteors, the temporal variation in amplitude varies according to Equation 15.

The signal decay can also be expressed as:

$$A(t) = A_0 \cdot e^{\left(-\frac{t}{\tau}\right)} \quad (16)$$

Where  $t$  is time and  $\tau$  is the time for the amplitude to fall to  $1/e$  of its maximum value. From the two expressions we get one for the ambipolar diffusion coefficient:

$$D_a = \lambda^2 / 16 \pi^2 \tau \quad (17)$$

This coefficient has also been shown to depend on atmospheric temperature and pressure [*Mason and McDaniel, 1988*]:

$$D_a = K_{amb} \cdot \frac{T^2}{P} \quad (18)$$

$$K_{amb} = 6.39 \cdot 10^{-2} K_0 \quad (19)$$

$K_0$  is the zero-field mobility of the plasma in the meteor trail, and depends on the species of ions assumed to comprise the meteor trail. We use  $K_0 = 2.4 \cdot 10^{-4} m^{-2} s^{-1} V^{-1}$  in accordance with *Cervera and Reid [2000]*, and references therein.

Measuring decay times with a radar and calculating corresponding ambipolar diffusion coefficients  $D_a$  will provide an estimate of  $T^2/P$ . Input of pressures from measurements or models allows us to find the corresponding temperature [*Holdsworth, 2006*].

### 5.3 Zonal and meridional winds from meteor echoes

To be able to determine the winds guiding the motion of the meteors, the cross-correlation between the complex data recorded on each receiver must be found and then the phase differences at zero lag is used to deduce the angle of arrival. The rate of change of phase gives the radial velocity [*Hocking, 2001*]. Once a large number of radial velocities have been collected, it is necessary to use these data to determine zonal and meridional winds. Usually this is done by clustering the radial velocities into groups – in our case 30-minute bins, and 1 km height bins for the

raw data. Then a least-squares fitting procedure are applied to determine mean wind components for this height-time bin. Finally the bin is shifted by half its size and the calculation repeated [e.g. *Tsutsumi et al.*, 1999]. This 4-bit complementary code means that the neighboring height influences the measurement at the main altitude bin.

Figure 13 and 14 shows the mean zonal and meridional wind from 2001-2009 measured by NSMR from 80-100 km altitude. The transition from eastward winds during the winter to westward winds during summer is identified in Figure 13 around day 100 (10 April). The mean meridional winds in Figure 14 are as expected weaker in magnitude, but the feature of mean northward meridional winds during winter and southward winds during summer are clearly visible. The zonal and meridional wind measurements we utilized in *Paper 2* were daily averages over 2 km height bins to make them in a more useful format to be compared to our daily averaged rotational OH temperatures.

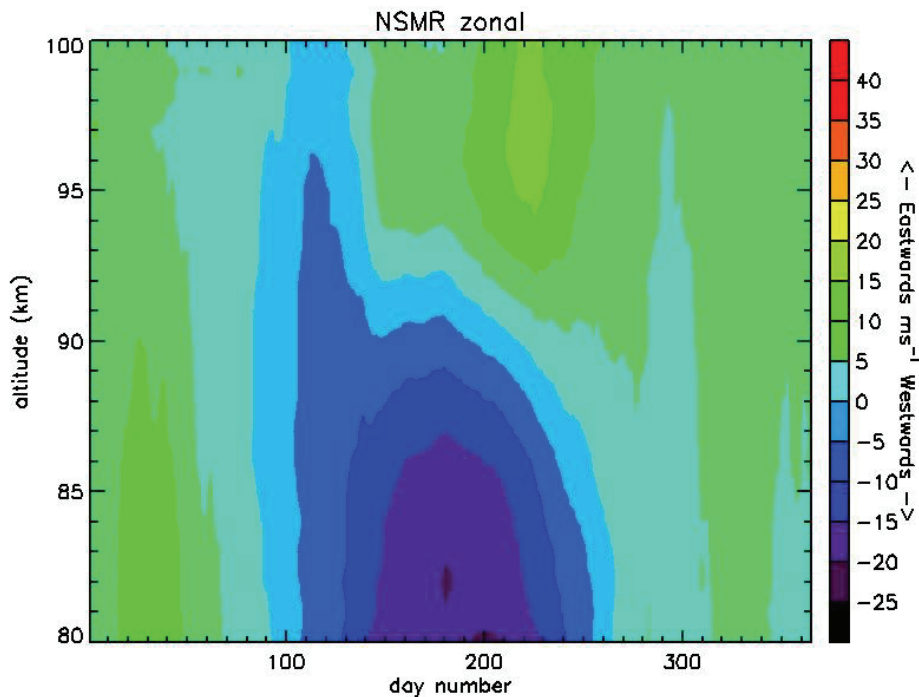


**Figure 13.** Mean zonal winds measured at 90 km by the NSMR meteor radar from 2001-2009. Contour levels are at 5 m/s (courtesy of Chris Hall).

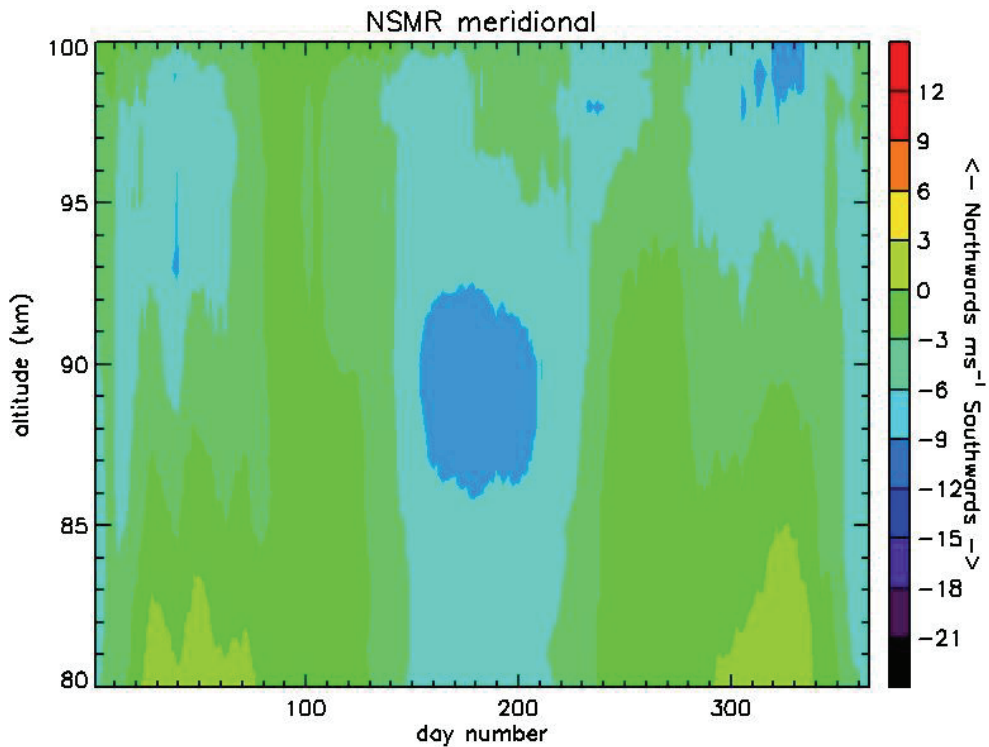


**Figure 14.** Mean meridional winds measured at 90 km by the NSMR meteor radar above Svalbard from 2001-2009. Contour levels are at 3 m/s (courtesy of Chris Hall).

## 5.4 Uncertainties

Roughly above 95 km, the motion of electrons becomes increasingly magnetically dominated due to fewer collisions with the neutral atmosphere [Dyrud *et al.*, 2004]. The diffusion of meteor trail has been shown to be anisotropic and also showing a distinct diurnal variation probably being related to tidally driven variations of the electric field [Hocking, 2005]. Below 90 km collisions with neutral molecules damps the motions of ions and electrons [Dyrud *et al.*, 2001]. Results from a study by Havnes and Sigernes [2005] show that the meteor decay time can decrease up to 10% for a trail affected by absorption of trail electrons by dust compared to one where there is no absorption by dust. Singer *et al.* [2008] studied the above mentioned effects on diffusion rates measured from Andøya 67°N and found that

for altitudes below 88 km weak meteor echoes were correlated with reduced decay times (increased diffusion rates). They also found that for summer the decay times were further reduced at Andøya, however not at lower latitudes. This is probably related to the presence of larger icy particles (NLC particles) in the lower part of the cold summer mesopause region. Their measurements also confirmed that anomalous/anisotropic diffusion rates can be ruled out at height below 91 km. Based on this we argue that our choice of using only the 90 km echoes for the temperature retrieval in *Papers 4* is reasonable. These effects are not believed to influence the wind measurements, since the total motion of the meteor trails are still determined by the collisions of ions and the neutral atmosphere [Tsutsumi *et al*, 1999].

Uncertainties in the altitude determination of meteor echoes are of the order of 1 km. The relative uncertainty in the raw temperature estimates used in our papers is based on the derivation from uncertainties in the ambipolar diffusion coefficients (obtained from M. Tsutsumi, personal communication). Typical values are ~2 K, but at times reaching up to 10 K. The total uncertainty after calibration with Aura MLS data is probably in the order of ~7 K (*Paper 4*).

## 6 Remote sensing from satellites

### 6.1 Limb scanning

Both Aura MLS and SABER are limb sounders, meaning their field of view through the atmosphere is at an angle to the underlying atmosphere, not straight down towards Earth like nadir viewing satellites. Aura MLS scans at off-nadir angles of  $\sim 66^\circ$  and has a narrow beam width. SABER observes the atmosphere in a longer path centered at a tangent point where most of the signal comes from. Having a narrower field of view than Aura MLS, the vertical resolution is much better for SABER. 2 km as opposed to the down to 13 km for Aura MLS at  $\sim 97$  km [Remsberg *et al.*, 2008; Schwartz *et al.*, 2008]. Since we have not been involved in the actual temperature retrieval for the satellite data, we will only give a brief overview of the temperatures retrieval and the assumptions made in the following paragraphs.

### 6.2 SABER temperatures and OH volume emission rates

SABER temperatures and pressures in the mesosphere are retrieved from observed radiances of CO<sub>2</sub> 15  $\mu\text{m}$  limb emissions. Above 40 km CO<sub>2</sub> is believed to be in a non-local-thermodynamical equilibrium (NLTE) state and the NLTE algorithm described by Remsberg *et al.* [2008] is used for the temperature retrieval. The retrievals of temperatures in the upper mesosphere for NLTE conditions depend on the knowledge of the decrease of CO<sub>2</sub> and its assumed uncertainties. Version 1.07 data which are used in *Papers 2, 3 and 4*, obtains average day and night profiles from the Whole-Atmosphere Community Climate Model (WACCM) and adjusts them to the CO<sub>2</sub> retrieved using the LTE model.

In addition to the kinetic temperatures obtained from SABER (*Paper 4*), we used so-called SABER OH\* brightness temperatures in *Papers 2 and 3*. These were obtained by fitting a Gaussian to the measured OH 1.6  $\mu\text{m}$  volume emission rate (VER) of the OH\* vibrational bands: (4-3) and (5-3) [Mulligan and Lowe, 2008]. From the OH\* VER profiles measured, the altitude of the emission layer and the integrated rate of emission was also computed. The peak altitude was chosen to be the peak altitude of the Gaussian that best fitted the measured OH\* VER profile,

following the method of *Liu and Shepherd* [2006]. The corresponding integrated emission rate was obtained by computing the integral of the area under the OH VER profiles.

Version 1.07 kinetic temperatures from CO<sub>2</sub> and OH VER profiles were obtained from NASA at the website: <http://saber.gats-inc.com>. Data were downloaded via anonymous login at: [ftp://saber.gats-inc.com/Version\\_07](ftp://saber.gats-inc.com/Version_07). We selected SABER profiles with tangent points at an altitude of 90±10 km and geographic coordinates within 78±5°N, 16±10°E (circle of ~600 km from the ground-based instruments). The field-of-view of SABER is such that its measurements come from different times of the day throughout the year (see *Paper 4*).

### **6.3 Aura MLS temperatures**

Temperatures from Aura MLS has been thoroughly described and validated by *Schwartz et al.* [2008]. The temperatures used in this study are retrieved from thermal emissions near the 118 GHz O<sub>2</sub> and 234 GHz O<sup>18</sup>O spectral lines. Emissions in these spectral regions are dominated by oxygen and are used to infer limb tangent-point pressures of MLS observations and to retrieve temperatures and geopotential heights. The resolution in the 80-100 km region is only ~13 km. Temperatures at 90 km were thus found by interpolation between points covering these altitudes.

The version 2.2 temperatures used in this study were acquired as a part of the activities of the NASA Earth-Sun System Division, and are archived and distributed by the Goddard Earth Sciences (GES) Data and Information Services Center (DISC) ([http://disc.sci.gsfc.nasa.gov/Aura/data\\_holdings/MLS](http://disc.sci.gsfc.nasa.gov/Aura/data_holdings/MLS)). Only scans fulfilling the data-quality criteria specified by *Schwartz et al.* [2008] were selected. For comparison with our ground-based data only scans with tangent points at geographic coordinates within (78±5°N, 16±10°E) were selected (corresponds to ~600 km from observing station). The Aura MLS temperatures above Svalbard are measured at the same time of the day every day, from 02-11 UT (see *Paper 4*).

## 6.4 Uncertainties

The assumptions and uncertainties in the temperatures retrieval algorithms for SABER and Aura MLS data are thoroughly described by *Remsberg et al.* [2008] and *Schwartz et al.* [2008], respectively. We have discussed them in our *Paper 4*.

In short, SABER kinetic temperatures have a root-mean-square error of  $\sim 10\text{K}$  during the polar summer due to the uncertainty in the parameters for the NLTE algorithm. In the polar winter the uncertainty is reduced to  $\sim 5\text{K}$  [*Remsberg et al.*, 2008].

The accuracy of the Aura MLS temperatures is limited by the low vertical resolution near the mesopause region. A  $9\text{K}$  bias was observed compared to SABER temperatures [*Schwartz et al.*, 2008]. Given the bias and the  $\sim 2.5\text{K}$  precision in the technique itself, the root-mean square error is in the order of  $\sim 9\text{-}10\text{K}$ .



## 7 Results

In this chapter we summarize the results from the four papers that constitute the main part of this thesis. Instead of summing up the results from each paper separately, we will present and discuss the results within main scientific themes.

### 7.1 Multi-instrument derivation of temperatures

The title of this thesis is “Multi-instrument studies of polar mesopause region temperature and airglow variability”. Although we have not only studied the temperature, it was one of the main motivations to utilize much of infrastructure present at Svalbard to see the already reported temperature measurements from different perspectives. Comparisons between data sets were carried out to search for biases and the clue to which data set(s) are closest to the true neutral air temperature.

Figures 15, 16 and 17 show an overview of the temperature measurements available from the mesopause region above Longyearbyen/Adventdalen, Svalbard, from 2001-2003, 2004-2006, and 2007-2009, respectively. OH(6-2) temperatures are available from 2001-2006 and the time series is reported in *Paper 1*. The SABER temperatures in Figures 15, 16 and 17 are the OH\* brightness temperatures described in *Paper 2*. We calculated them for 2001-2008. Both the SABER and OH(6-2) temperatures represent the temperature of the OH layer which has been shown to vary a lot in altitude [Winick *et al.*, 2009; *Paper 2*; *Paper 3*]. This is why we have denoted the altitude of the OH temperatures with quotation marks, i.e. “87 km”, in the legends of these figures. When comparing these two temperature sets for the winter 2003-2004, we found a positive bias of  $14 \pm 9$  K in favor of the SABER temperatures.

The Aura MLS and MWR temperatures have year-round coverage and can be viewed as “spot” temperatures representative of 90 km temperatures. SABER also measures “spot” temperatures, but these are not shown in Figures 15-17, however they are presented and discussed in *Paper 4*. Aura MLS data are available from August 2004 to June 2009. The MWR temperatures were obtained from October 2001 to June 2009.

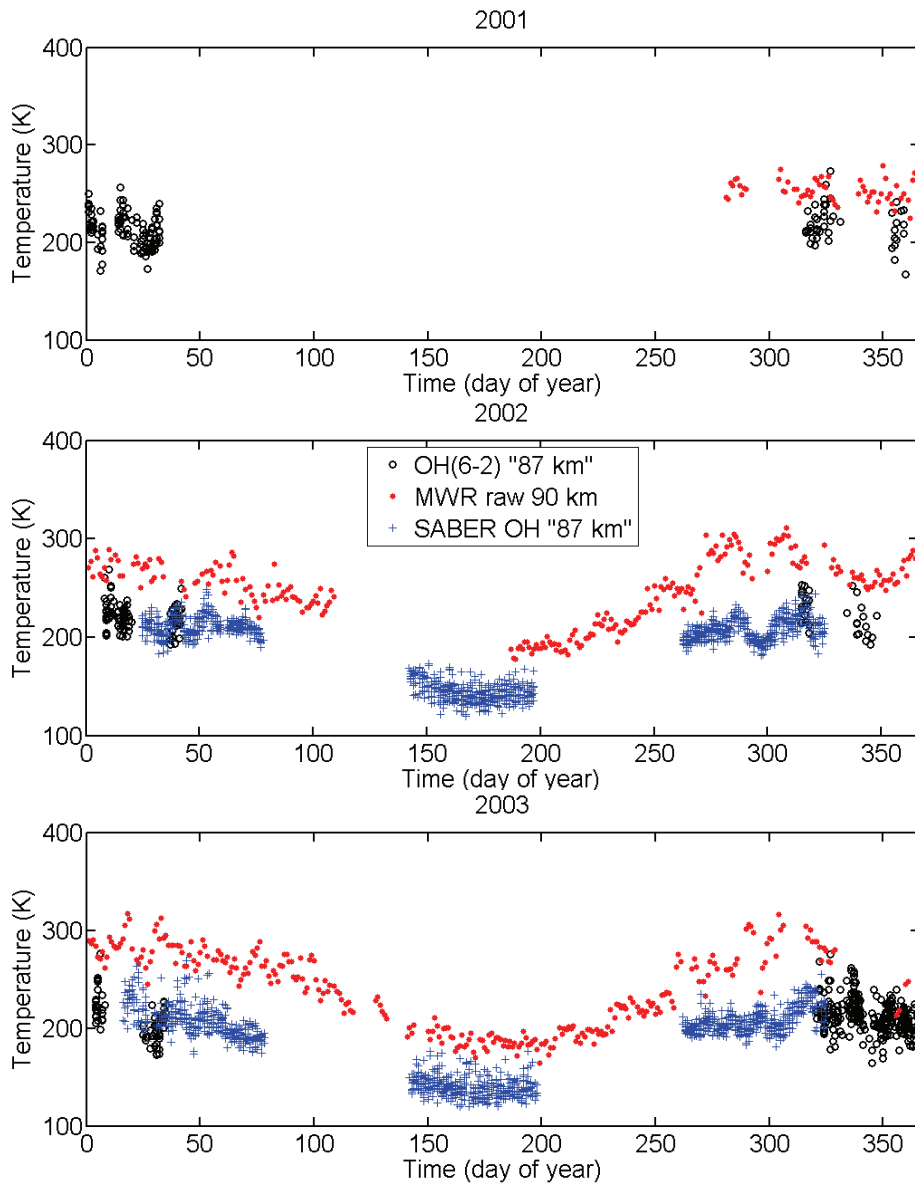


**Figure 15.** Mesopause region temperatures measured above Longyearbyen from 2001-2003. Black circles denote hourly averaged OH(6-2) temperatures measured by spectrometer. Red bullets denote daily averaged non-calibrated meteor radar temperatures. Blue plusses denote single-scan temperatures obtained from SABER.

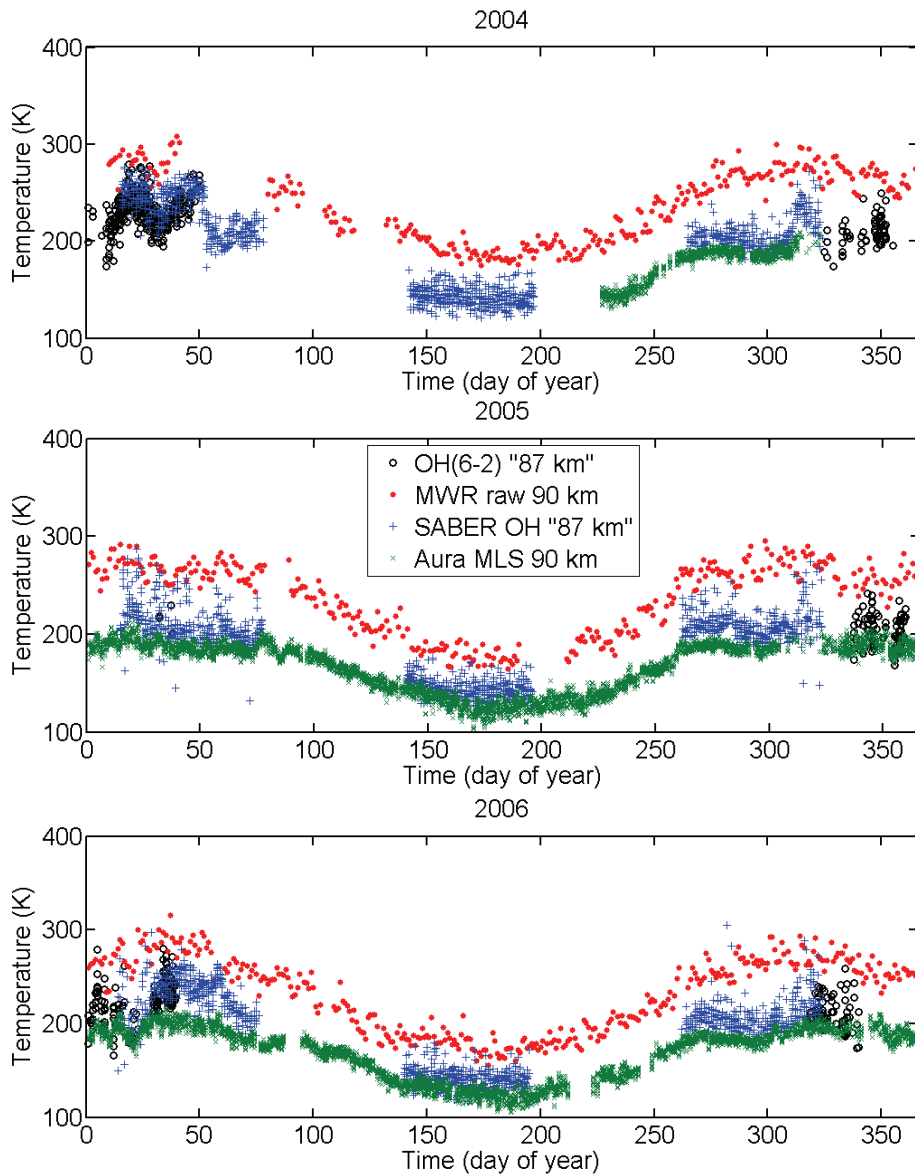


**Figure 16.** Mesopause region temperatures measured above Longyearbyen from 2004-2006. Black circles denote hourly averaged OH(6-2) temperatures measured by spectrometer. Red bullets denote daily averaged non-calibrated meteor radar temperatures. Blue plusses denote single-scan temperatures obtained from SABER and green crosses show 90 km temperatures obtained from Aura MLS.

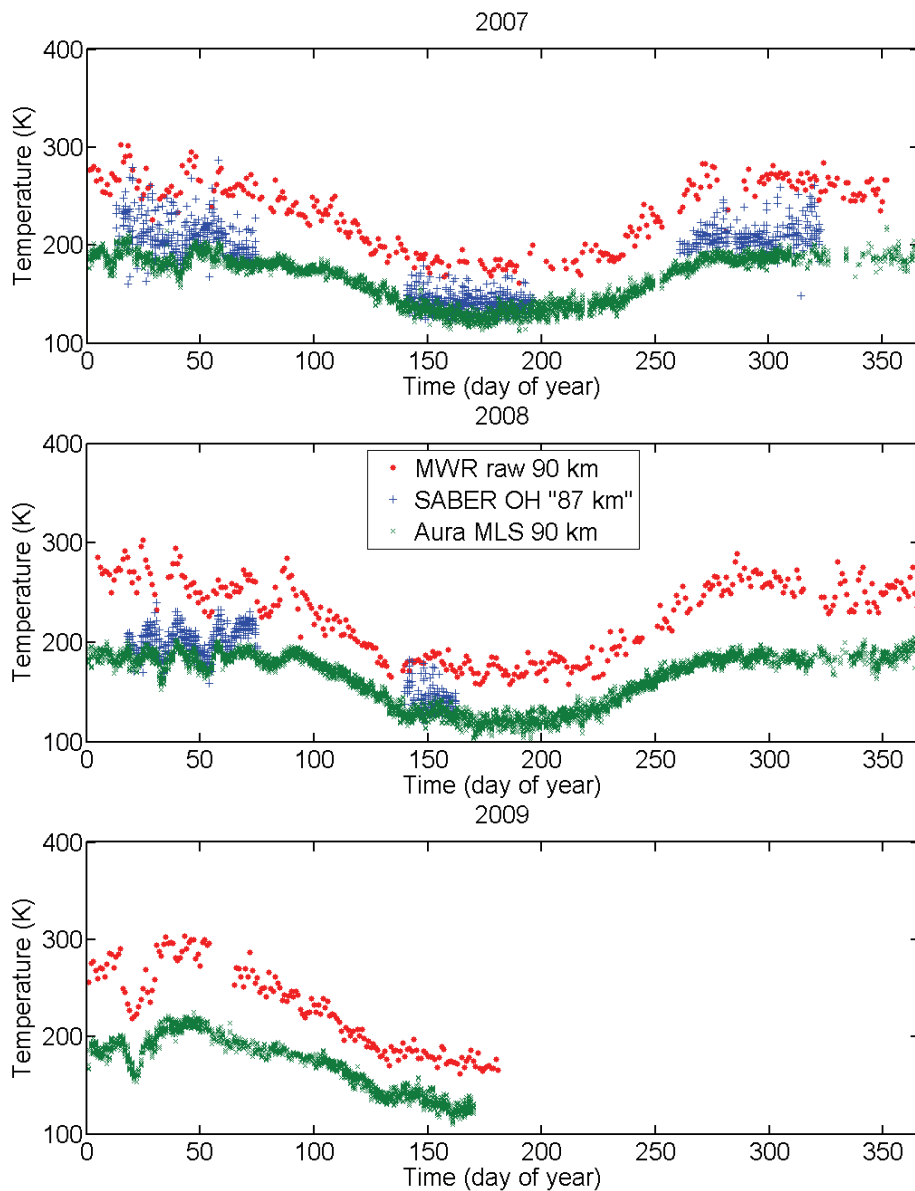


**Figure 17.** Mesopause region temperatures measured above Longyearbyen from 2007-2009. Red bullets denote daily averaged non-calibrated meteor radar temperatures. Blue pluses denote single-scan temperatures obtained from SABER and green crosses show 90 km temperatures obtained from Aura MLS.

The latter have the advantage that measurements can be made at all times of day and all year, but from the figures it is obvious that they need calibration/adjustment by another independent temperature measurement since they are clearly overestimated. In *Paper 4* we investigated which of the Aura MLS and SABER temperature sets that would be most suitable for acting as input in the calibration of the MWR temperatures and concluded that the Aura MLS was the best. The resulting time series after calibration was presented and discussed in *Papers 4*. The linear correlation coefficient between the Aura MLS and the raw MWR temperatures was found to be 0.94 with a probability of random occurrence very close to zero, when all coincident data from 2004-2009 were used. Choosing the Aura MLS temperatures as input in the MWR calibration routine instead of the OH(6-2) and K-lidar temperatures used in previous calibrations [Hall *et al.*, 2004] decreased the estimated uncertainty of the calibrated MWR temperatures from 17 K to 7 K. The resulting temperatures were shown to be lower than temperatures from the NRLMSISE-00 model [Picone *et al.*, 2002], but in accordance with the K-lidar measurements from summers 2001-2003. The previously reported cold bias of 9K for Aura MLS [Schwartz *et al.*, 2008] might also have introduced a cold bias in the calibrated MWR temperatures. The SABER 90 km “spot” temperatures were found to be consistently warmer than the Aura MLS temperatures for 2005. A mean difference of  $19 \pm 11$  K was found (*Paper 4*). The difference was larger for summer than winter. Future studies should aim to find the correct absolute temperature. We argue in *Paper 4* that although we have not determined which of the techniques from our studies comes closest to providing the true neutral air temperature, we have improved the estimate and reduced the uncertainty of the 90 km neutral air measured by the NSMR radar. The resulting time series will be a useful tool for future studies of mesopause region dynamics above the high-Arctic.

Figures 15-17 also reveal that all four temperature measurement algorithms are able to retrieve many of the same relative variations in the neutral air temperature, even though two are temperatures of the OH layer changing with height while the other two are assumed to be neutral air temperatures for a constant altitude.

## **7.2 Atmospheric coupling**

From Figures 15-17 several mesospheric cooling events are easily identifiable, e.g the most recent one in mid-January 2009 (see Figure 17) which is probably

associated with the strongest and most prolonged SSW on record [Manney *et al.*, 2009]. In Figure 16 we see a mesospheric cooling displayed as a “V-shape” around 1 February 2004 in both the SABER, OH(6-2) and MWR temperatures. This event is associated with a reported minor sudden stratospheric warming and is studied in *Paper 2*.

In our work preparing *Paper 1* we noticed that the winter season 2003-2004 was anomalous in the sense that exceptionally good observing conditions allowed many hourly averaged spectra to be saved for temperature retrieval and the temperatures observed were unusually high.

In *Paper 2* we investigated the SABER OH\* brightness- and OH(6-2) rotational temperatures and the NSMR wind data for the whole winter season 2003-2004. As expected we found a correlation between the reported major sudden stratospheric warming (SSW) event that took place in mid-January 2004 and reversals of mesopause region winds. We also found a strong and highly significant linear relationship between the strength of the meridional wind and the temperature and altitude of the OH layer. A similar relationship was found for Antarctic data by *Espy et al.* [2003]. SABER measurements show that the OH layer was very low during extended periods of the winter 2003-2004, especially right after the SSW. *Winick et al.* [2009] had also shown that the unusually high temperatures observed during January and February 2004 (240-250 K) corresponded with a very low and bright OH layer. Our data confirmed their measurements and support the theory that the high temperatures result from an anomalously strong upper stratospheric vortex which confined air to the polar regions, coupled to the meridional transport and led to a strong downwelling of atomic oxygen rich air thereby lowering the altitude of the OH layer. Our SABER data revealed that the reformation of the OH layer at approximately 78 km altitude accounted for an increase in temperature of approximately 15 K, while the remaining temperature increase (20-35 K) was attributed to adiabatic heating. Thus up to 30% of the total temperature increase can be attributed directly to the lowering of the OH layer.

### **7.3 OH layer altitude, radiance and temperature**

Motivated by the clear linear relationship between OH layer altitude and temperature found in *Paper 2* we wanted to see if there was also a clear relationship between OH emission radiance and altitude.

In paper 3 we adopted the method of *Liu and Shepherd* [2006] and investigated the relationship between OH emission radiance and OH layer peak altitude based on SABER measurements. In the SABER data for the period 2002-2008, the peak altitude of the OH layer ranged from a minimum near 76 km to a maximum near 90 km. A clear relationship between altitude and integrated volume emission rate (VER) was found. The overlap of SABER and ground-based spectrometer measurements of OH(6-2) band intensities during the 2003-2004 winter season allowed us to express radiance values in terms of the satellite integrated VER measurements. So although the OH(6-2) spectra measured by the ground-based Ebert-Fastie spectrometer were not intensity calibrated, the combination of these relationships provided a method for inferring an altitude of the OH emission layer over Longyearbyen from ground-based measurements alone. Such a method is required when SABER is in a southward looking yaw cycle.

The expression and coefficients needed for retrieving OH emission peak altitudes from radiance values measured by the ground-based spectrometer is given in *Paper 3*. The uncertainty in the inferred altitude of the peak emission, which includes a contribution for atmospheric extinction, was estimated to be  $\pm 2.7$  km.

## **7.4 Periodic variations and temperature trends**

In *Paper 1* we looked for short term and long term variations in temperatures. We performed Lomb-Scargle periodogram analysis on the hourly and daily averaged OH(6-2) times series. The analysis revealed  $\sim 24$  and  $\sim 26$  periods, that might be associated with the 27 day solar rotation period [*Hall et al.*, 2006]. *Höppner and Bittner* [2009] have found similar time periods in their OH rotational temperature data set from Germany. No consistent diurnal or semi-diurnal variations were identified by analysis of the hourly averaged data. However, for a limited subset a clear semi-diurnal period was found in accordance with what has previously been observed by e.g. *Walterscheid et al.* [1986].

An updated trend analysis of the yearly averaged OH(6-2) winter temperatures between 1983 and 2005 found a trend of  $+0.2 \pm 0.1$  K/year. This is on the verge of being statistically significant, however keeping in mind the results from *Papers 2* and *3* where we found that for 2003-2004 the OH layer altitude was down as low as below 80 km, we realize that the “true” trend might be masked by the large perturbations of the OH layer.



## **8 Concluding remarks and perspectives for the future**

In this thesis temperatures, airglow emissions and winds from the mesopause region (80-100 km) have been investigated by several ground-based and satellite instruments. The purpose and motivation was to learn more about the dynamics of this region and how it couples to other regions.

Our main tools for completing this task were the Nippon/Norway Svalbard Meteor Radar (NSMR) and a 1 meter focal length Ebert-Fastie spectrometer located within 5 km from each other in Adventdalen (78°N, 16°E). The first has the advantage of being able to make measurements of temperatures at 90 km throughout the full day and year, although independent calibration is necessary. The radar has been in operation since 2001. The spectrometer has been in use for 25 years and has provided one of the longest time series of hydroxyl rotational winter temperatures in the world. Although problems with decreased signal to noise ratio have made temperature retrieval problematic after 2006, this instrument will be upgraded and continue to make measurements of hydroxyl spectra from the Kjell Henriksen Observatory (KHO). Data from the satellites TIMED and Aura provided measurements that were highly useful for comparison with our ground-based data.

By combining satellite and ground-based measurements of hydroxyl airglow layer brightness, we were able to find a relationship between the hydroxyl layer peak height and the radiance for the winter 2003/2004. The satellite measurements revealed periods of very low hydroxyl layer peak heights during the winter 2004. A task for future studies of the time series should be to check if this relationship is also valid for the earlier and later data of the time series. Raw spectra are available from 1991, and TIMED SABER measurements from 2001.

When searching for a correlation with mesopause region zonal and meridional winds measured by meteor radar, we found a clear linear relationship between the variation of peak layer height and the strength of the meridional wind. That the response to wind changes was so evident was a surprise to us, although we were not the first to observe it. Since wind measurements are available from 2001 to present, it should be a task to check if this direct coupling is valid for other seasons than 2003/2004 for example by comparing measurements from SABER and

NSMR. Including observing stations from other latitudes and longitudes would be useful to test if the coupling is also valid on a global scale.

The long term trend analyses of the hydroxyl rotational temperature series have so far failed to reveal a significant trend. However, there are many different approaches for making trend analyses. This high latitude time series is unique, and further studies may include testing the effect the varying hydroxyl layer altitude has on the trend estimate. Since the temperature series from the meteor radar is close to the length of one solar cycle it would be very interesting to search for trends in this temperature series also. It does not suffer from variable observing conditions in the same way as the optical measurements do. A preliminary analysis suggests a negative trend of the order of  $\sim 8\text{K}$  per decade in both the summer and winter temperatures after solar cycle dependence have been subtracted. However, since this result strongly contradicts the recent general understanding of temperature trends in the mesopause region, a thorough analysis is necessary before conclusions can be made and published. This would include deseasonalizing the time series and estimating the significance of the linear trend. The trend analysis on this time series is therefore not included in this thesis, but will be published in a later paper.

## References

- Akmaev, R. A., and V. I. Fomichev (2000), A model estimate of cooling in the mesosphere and lower thermosphere due to CO<sub>2</sub> increase over 3-4 decades, *Geophys. Res. Lett.*, *27*, 2113-2117.
- Andrews, D. G., J. R. Holton, and C. B. Leovy (1987), Middle atmosphere dynamics, *2nd Ed.*, Academic Press, Inc., Florida.
- Ångström, A. J. (1869), Spektrum des nordlichts, *Pogg. Ann.*, *137*, 161-163.
- Azeem, S. M. I., G. G. Sivjee, Y.-I. Won, and C. Mutiso (2007), Solar cycle signature and secular long-term trend in OH airglow temperature observations at South Pole, Antarctica, *J. Geophys. Res.*, *112*, A01305, doi:10.1029/2005JA011475.
- Baker, D. J., and A. T. Stair Jr. (1988), Rocket measurements of the altitude distributions of the hydroxyl airglow, *Phys. Scr.*, *37*, 611-622.
- Bates, D. R., and Nicolet, M. (1950), The photochemistry of atmospheric water vapor, *J. Geophys. Res.*, *55*, 301.
- Beig, G., P. Keckhut, R. P. Lowe, R. G. Roble, M. G. Mlynczak, J. Scheer, V. I. Fomichev, D. Offermann, W. J. R. French, M. G. Shepherd, A. I., Semenov, E. E. Remsberg, C. Y. She, F. J. Lübken, J. Bremer, B. R. Clemesha, J. Stegman, F. Sigernes, and F. Fadnavis (2003), Review of mesospheric temperature trends, *Rev. Geophys.*, *41*(4), 1015, doi:10.1029/2002RG000121.
- Bittner, M, D. Offermann, H.-H. Graef, M Donner, and K. Hamilton (2002), An 18-year time series of OH rotational temperatures and middle atmosphere decadal variations, *J. Atmos. Sol. Terr. Phys.*, *64*, 1147-1166.
- Cervera, M. A., and I. M. Reid (2000), Comparison of atmospheric parameters derived from meteor observations with CIRA, *Radio Sci.*, *35*, 833-843.
- Cervera, M. A., and W. G. Elford (2004), The meteor radar response function: Theory and application to narrow beam MST radar, *Planet. Space Sci.*, *52*, 591-602.

- Chamberlain, J. W., and F. L. Roesler (1955), The OH bands in the infrared airglow, *Astrophys. J.*, *121*, 541.
- Chamberlain, J. W. (1961), Physics of the aurora and airglow, *Academic Press, New York*.
- Chanin, M. -L. (2006), Signature of the 11-year cycle in the upper atmosphere, *Space Sci. Rev.*, *125*, 261-272, doi: 10.1007/s11214-006-9062-5.
- Cosby, P. C., and T. G. Slanger (2007), OH spectroscopy and chemistry investigated with astronomical sky spectra, *Can. J. Phys.*, *85*, 77-99, doi: 10.1139/P06-088.
- Duck, T. J., A. Whiteway, and A. I. Carswell (1998), Lidar observations of gravity wave activity and Arctic stratospheric vortex core warming, *Geophys. Res. Lett.*, *25*, 2813-2816.
- Dyrud, L. P., M. M. Oppenheim, A. F. vom Endt (2001), The anomalous diffusion of meteor trails, *Geophys. Res. Lett.*, *28*, 2775-2778.
- Dyrud, L. P., K. Denney, J. Urbina, D. Janches, E. Kudeki, and S. Franke (2004), The meteor flux: It depends where you look, *Earth Moon Planets*, *95*, 89-100.
- Espy, P. J., R. E. Hibbins, G. O. L. Jones, D. M. Riggins, and D. C. Fritts (2003), Rapid, large-scale temperature changes in the polar mesosphere and their relationship to meridional flows, *Geophys. Res. Lett.*, *30*(5), 1240, doi: 10.1029/2002GL016452.
- Fastie, W. G. (1952), Image forming properties of the Ebert monochromator, *J. Opt. Soc. Am.*, *42*(9), 647-651.
- French, W. J. R., G. B. Burns, K. Finlayson, P. A. Greet, R. P. Lowe, and P. F. B. Williams (2000), Hydroxyl (6-2) airglow emission intensity ratios for rotational temperature determination, *Ann. Geophys.*, *18*, 1293-1303.
- Gadsden, M., and W. Schröder (1989), Noctilucent clouds, *Springer, Berlin*.
- Garcia, R. R., D. R. Marsh, D. E. Kinnison, B. A. Boville, and F. Sassi (2007), Simulation of secular trends in the middle atmosphere, 1950-2003, *J. Geophys. Res.*, *112*, D09301, doi:10.1029/2006JD007485.

- Gerrard, A. J., T. J. Kane, J. P. Thayer, T. J. Duck, J. A. Whiteway, and J. Fiedler (2002), Synoptic scale study of the Arctic polar vortex's influence on the middle atmosphere, 1, Observations, *J. Geophys. Res.*, *107*, D16, 4276, doi:10.1029/2001JD000681.
- Goldman, A., W. G. Schoenfeld, D. Goorvitch, C. Chackerian Jr., H. Dothe, F. Mélen, M. C. Abrams, and J. E. A. Selby (1998), Updated line parameters for OH X<sup>2</sup>I-X<sup>2</sup>I (v'',v') transitions, *J. Quant. Spectrosc. Radiat. Transfer*, *59*, 453-469.
- Haigh, J. D. (2006), Introduction, *Space Sci. Rev.*, *125*, 5-15, doi: 10.1007/s11214-006-9042-9.
- Hall, C. M., T. Aso, M. Tsutsumi, J. Höffner, and F. Sigernes, Multi-instrument derivation of 90 km temperatures over Svalbard (78°N, 16°E) (2004), *Radio. Sci.*, *39*, RS6001, doi: 10.1029/2004RS003069.
- Hall, C. M., T. Aso, M. Tsutsumi, J. Höffner, F. Sigernes, and D. A. Holdsworth, Neutral air temperatures at 90 km and 70°N and 78°N (2006), *J. Geophys. Res.*, *111*, D141105, doi: 10.1029/2005JD006794.
- Hall, C. M., J. Röttger, K. Kuyeng, M. Tsutsumi, M. Dyrland, and J. L. Chau (2009), Polar mesospheric summer echoes at 78°N, 16°E, 2008: First results of the refurbished sounding system (SOUSY) Svalbard radar, *J. Geophys. Res.*, *114*, D11111, doi:10.1029/2008JD011543.
- Havnes, O., and F. Sigernes (2005), On the influence of background dust on radar scattering from meteor trails, *J. Atmos. Sol. Terr. Phys.*, *67*, 659-664.
- Herzberg, G. (1934), Photography of the infra-red solar spectrum to wavelength 12,900 Å, *Nature*, *133*, 759-759, doi:10.1038/133759a0.
- Herzberg, G. (1950), Molecular spectra and molecular structure I: Spectra of diatomic molecules, 2<sup>nd</sup> ed., *D. Van Nostrand Reinhold, New York*.
- Hill, E., and J. H. van Vleck (1928), On the quantum mechanics of the rotational distortion of multiplets in molecular spectra, *Phys. Rev.*, *32*, 250-272.
- Hocking, W.K., Fuller, B., and B. Vandeppeer (2001), Real-time determination of meteor-related parameters utilizing modern digital technology, *J. Atmos. Sol. Terr. Phys.*, *63*, 155-169.

- Hocking, W. K. (2005), Experimental radar studies of anisotropic diffusion of high altitude meteor trails, *Earth Moon Planets*, doi:10.1007/s11038-005-3446-5.
- Holdsworth, D.A., R.J. Morris, D.J. Murphy, I.M. Reid, G.B. Burns and W.J.R. French (2006), Antarctic mesospheric temperature estimation using the Davis MST radar, *J. Geophys. Res.*, *111*, D05108, doi:10.1029/2005JD006589.
- Holton, J. R. (1983), The influence of gravity wave breaking on the general circulation of the middle atmosphere, *J. Atmos. Sci.*, *40*, 2497-2507.
- Holton, J. R. (2004), An introduction to dynamic meteorology, *Elsevier Academic Press, London, UK*.
- Hoppe, U-P. (2001), Stratospheric warmings – The quasi-biennial oscillation, *FFI/Rapport-2001/02263*.
- Höppner, K., and M. Bittner (2009), Detection of solar activity signatures in the OH\* temperature fluctuations possibly related to the differential rotation of the Sun, *J. Atmos. Sol. Terr. Phys.*, *71*(12), 1287-1292.
- Jackman, C., R. McPeters, G. Labow, E. Fleming, C. Praderas, and J. Russell (2001), Northern hemisphere atmospheric effects due to the July 2000 solar proton event, *Geophys. Res. Lett.*, *28*(15), 2883-2886.
- Jarvis, M. J. (2001), Bridging the atmospheric divide, *Science*, *293*(5538), 2218-2219, doi: 10.1126/science.1064467.
- Krassovsky, V. I., N. N. Shefov, and V. I. Yarin (1962), Atlas of the airglow spectrum 3000-12,400 Å, *Planet. Space Sci.*, *9*, 883-915.
- Kuhn, W. R., and J. London (1969), Infrared radiative cooling in the middle atmosphere (30-110 km), *J. Atmos. Sci.*, *26*(2), 189-204.
- Kvifte, G. (1961), Temperature measurements from OH bands, *Planet. Space Sci.*, *5*, 133-157.
- Labitzke, K. (1972), Temperature changes in the mesosphere and stratosphere connected with circulation changes in winter, *J. Atmos. Sci.*, *29*, 765-766.
- Langhoff, S. R., H-J. Werner, and P. Rosmus (1986), Theoretical transition probabilities for the OH Meinel system, *J. Molec. Spectrosc.*, *118*, 507-529.

- Liu, H.-L., and R. G. Roble (2002), A study of a self-generated stratospheric sudden warming and its mesospheric-lower thermospheric impacts using the coupled TIME-GCM/CCM3, *J. Geophys. Res.*, *107*(D23), 4695.
- Liu, G., and G. G. Shepherd (2006), An empirical model for the altitude of the OH nightglow emission, *Geophys. Res. Lett.*, *33*, L09805, doi: 10.1029/2005GL025297.
- Llewellyn, E. J., B. J. Long, and B. H. Solheim (1978), The quenching of OH\* in the atmosphere, *Planet. Space Sci.*, *26*, 525-531.
- López-Puertas, M., M. A. López-Valverde, and F. W. Taylor (1992), Vibrational temperatures and radiative cooling of the CO<sub>2</sub> 15 μm bands in the middle atmosphere, *Q. J. R. Meteorol. Soc.*, *118*, 499-532.
- Manney, G. L., K. Krüger, J. L. Sabutis, S. A. Sena, and S. Pawson (2005), The remarkable 2003-2004 winter and other recent warm winters in the Arctic stratosphere since the late 1990s, *J. Geophys. Res.*, *110*, D04107, doi:10.1029/2004JD005367.
- Manney, G. L., M. J. Schwartz, K. Krüger, M. L. Santee, S. Pawson, J. N. Lee, W. H. Daffer, R. A. Fuller, and N. J. Livesey (2009), Aura Microwave Limb Sounder observations of dynamics and transport during the record-breaking 2009 Arctic stratospheric major warming, *Geophys. Res. Lett.*, *36*, L12815, doi:10.1029/2009GL038586.
- Mason, E. A., and E. W. McDaniel (1988), Transport properties of ions in gases, *Wiley, London*.
- McKinley, D. W. R. (1961), Meteor science and engineering, *McGraw Hill, New York*.
- Meinel, I. A. B. (1950), OH emission bands in the spectrum of the night sky, *Astrophys. J.*, *111*, 555-564.
- Meriwether, J. W. (1989), A review of the photochemistry of selected nightglow emissions from the mesopause, *J. Geophys. Res.*, *94*(D12), 14629-14646.
- Mies, F. H. (1974), Calculated vibrational transition probabilities of OH(X<sup>2</sup>Π), *J. Molec. Spectrosc.*, *53*, 150-188.

- Mueller-Wodarg, I. C. F., D. F. Strobel, J. I. Moses, J. H. Waite, J. Crovisier, R. V. Yelle, S. W. Bougher, and R. G. Roble (2008), Neutral atmospheres, *Space Sci. Rev.*, *139*, 191-234, doi:10.1007/s11214-008-9404-6.
- Mulligan, F. J. and R. P. Lowe (2008), OH-equivalent temperatures derived from ACE-FTS and SABER temperature profiles - a comparison with OH\*(3-1) temperatures from Maynooth (53.2N, 6.4W), *Ann. Geophys.*, *26*, 795-811.
- Myrabø, H. K. (1986), Winter-season mesopause and lower thermosphere temperatures in the northern polar regions, *Planet. Space. Sci.*, *34*(11), 1023-1029.
- Myrabø, H. K., C. S. Deehr, R. Viereck, and K. Henriksen (1987), Polar mesopause gravity wave activity in the sodium and hydroxyl night airglow, *J. Geophys. Res.*, *92*(A3), 2527-2534, 1987.
- Olivero, J. J., and G. E. Thomas (2001), Evidence for changes in greenhouse gases in the mesosphere, *Adv. Space Res.*, *28*(7), 931-936.
- Pancheva, D., P. Muktarov, N. J. Mitchell, E. Merzlyakov, A. K. Smith, B. Andonov, W. Singer, W. Hocking, C. Meek, A. Manson, and Y. Murayama (2008), Planetary waves in coupling the stratosphere and mesosphere during the major stratospheric warming in 2003/2004, *J. Geophys. Res.*, *113*, D12105, doi:10.1029/2007JD009011.
- Pendleton, W. R., Jr., P.J. Espy, and M. R. Hammond (1993), Evidence for non-local-thermodynamic-equilibrium rotation in the OH nightglow, *J. Geophys. Res.*, *98*(A7), 11567-11579.
- Picone, J. M., A. E. Hedin, D. P. Drob, and A. C. Aikin (2002), NRLMSISE-00 empirical model of the atmosphere: Statistical comparisons and scientific issues, *J. Geophys. Res.*, *107*(A12), 1468, doi:10.1029/2002JA009430.
- Remsberg, E. E., B. T. Marshall, M. Garcia-Comas, D. Krueger, G. S. Lingenfelter, J. Martin-Torres, M. G. Mlynzcak, J. M. Russell III, A. K. Smith, C. Brown, L. L. Gordley, M. J. Lopez-Gonzales, M. Lopez-Puertas, C.-Y. She, M. J. Taylor, and R. E. Thomson (2008), Assessment of the quality of the Version 1.07 temperature-versus-pressure profiles of the middle atmosphere from TIMED/SABER, *J. Geophys. Res.*, *113*, D17101, doi:10.1029/2008JD010013.

- Russell, J. M., III, M. G. Mlynczak, L. L. Gordley, T. Tansock, and R. Esplin (1999), An overview of the SABER experiment and preliminary calibration results, *Proc. SPIE Int. Soc. Opt. Eng.*, 3756, 277-288.
- Röttger, J. (2000), Radar investigations of the mesosphere, stratosphere and troposphere in Svalbard., *Adv. Pol. Upp. Atmos. Res.*, 14, 202-220.
- Schmidt, H., G. P. Brasseur, M. Charron, E. Manzini, M. A. Giorgetta, T. Diehl, V. I. Fomichev, D. Kinnison, D. Marsh, and S. Walters (2006), The HAMMONIA chemistry climate model: Sensitivity of the mesopause region to the 11-year solar cycle and CO<sub>2</sub> doubling, *J. Clim.*, 19, 3903-3931.
- Schoeberl, M. R. (1978), Stratospheric warmings: Observations and theory, *Rev. Geophys Space Phys.*, 16, 521-538.
- Schoeberl, M. L., A. R. Douglass, E. Hilsenrath, P. K. Barthia, J. Barnett, J. Gille, R. Beer, M. Gunson, J. Waters, P. F. Levelt, and P. DeCola (2004), The EOS Aura Mission, *EOS, Transactions, American Geophysical Union* 85,18.
- Schwartz, M. J., A. Lambert, G. L. Manney, W. G. Read, N. J. Livesey, L. Froidevaux, C. O. Ao, P. F. Bernath, C. D. Boone, R. E. Cofield, W. H. Daffer, B. J. Drouin, E. J. Fetzer, R. A. Fuller, R. F. Jarnot, J. H. Jiang, B. W. Knosp, K. Krüger, J.-L. F. Li, M. G. Mlynczak, S. Pawson, J. M. Russell III, M. L. Santee, W. V. Snyder, P. C. Stek, R. P. Thurstans, A. M. Thomkins, P. A. Wagner, K. A. Walker, J. W. Waters, and D. L. Wu (2008), Validation of the Aura Microwave Limb Sounder temperature and geopotential height measurements, *J. Geophys. Res.*, 113, D15S11, doi:10.1029/2007JD008783.
- Shepherd, G. G., Y.-M. Cho, G. Liu, M. G. Shepherd, and R. G. Roble (2006), Airglow variability in the context of the global mesospheric circulation, *J. Atmos. Sol. Terr. Phys.*, 68, 2000-2011.
- Shepherd, M. G., D. L. Wu, I. N. Fedulina, S. Gurubaran, J. M. Russell, M. G. Mlynczak, and G. G. Shepherd (2007), Stratospheric warming effects on the tropical mesospheric temperature field, *J. Atmos. Sol. Terr. Phys.*, 69, 2309-2337, doi: 10.1016/j.jastp.2007.04.009.
- Sigernes, F., N. Shumilov, C. S. Deehr, K. P. Nielsen, T. Svenøe, and O. Havnes (2003), Hydroxyl rotational temperatures record from the auroral station in

- Adventdalen, Svalbard (78°N, 15°E), *J. Geophys. Res.*, *108*(A9), 1342, doi: 10.1029/2001JA009023.
- Singer, W., R. Latteck, L. F. Millan, N. J. Mitchell, and J. Fiedler (2008), Radar backscatter from underdense meteor and diffusion rates, *Earth Moon Planets*, *102*, 403-409, doi: 10.1007/s11038-007-9220-0.
- Sivjee, G. G., and R. M. Hamwey (1987), Temperature and chemistry of the polar mesopause OH, *J. Geophys. Res.*, *92*(A5), 4663-4672.
- Sivjee, G. G. (1992), Airglow hydroxyl emissions, *Planet. Space. Sci.*, *40*, 235-242.
- Thulasiraman, S., and J. B. Nee (2002), Further evidence of a two-level mesopause and its variations from UARS high-resolution Doppler imager temperature data, *J. Geophys. Res.*, *107*(D18), 4355, doi:10.1029/2000JD00018.
- Tsutsumi, M., D. Holdsworth, T. Nakamura and I. Reid (1999), Meteor observations with an MF radar, *Earth, Planets Space*, *51*, 691-699.
- Turnbull, D. N., and R. P. Lowe (1989), New hydroxyl transition probabilities and their importance in airglow studies, *Planet. Space. Sci.*, *37*, 723-738.
- van der Loo, M. P. J., and G. C. Groenenboom (2007), Theoretical transition probabilities for the OH Meinel system, *J. Chem. Phys.*, *126*, 114314.
- Viereck, R. A., and C. S. Deehr (1989), On the interaction between gravity waves and the OH Meinel (6-2) and the O<sub>2</sub> atmospheric (0-1) bands in the polar night airglow, *J. Geophys. Res.*, *94*(A5), 5397-5404.
- Walterscheid, R. L., G. G. Sivjee, G. Schubert, and R. M. Hamwey (1986), Large-amplitude semidiurnal temperature variations in the polar mesopause: evidence of a pseudotide, *Nature*, *324*, 347-349.
- Walterscheid, R. L., G. G. Sivjee, and R. G. Roble (2000), Mesospheric and lower thermospheric manifestations of a stratospheric warming event over Eureka, Canada (80°N), *Geophys. Res. Lett.*, *27*, 2897-2900.
- Wayne, R. P. (2000), Chemistry of atmospheres, *Oxford University Press Inc.*, New York.

- Wijkander, A (1874), Om norrskenets spectrum, *Övf. Kongl. Vet. Akad. Förh.*, 6, Stockholm.
- Winick, J. R., P. P. Wintersteiner, R. H. Picard, D. Esplin, M. G. Mlynczak, J. M. Russell III, and L. L. Gordley (2009), OH layer characteristics during unusual boreal winters of 2004 and 2006, *J. Geophys. Res.*, 114, A02303, doi:10.1029/2008JA013688.
- Yan, T., C-Y. She, D. A. Krueger, F. Sassi, R. Garcia, R. G. Roble, H-L. Liu, and H. Schmidt (2008), Climatology of mesopause region temperature, zonal wind, and meridional wind over Fort Collins, Colorado (41°N, 105°W), and comparison with model simulations, *J. Geophys. Res.*, 113, D03105, doi:10.1029/2007JD008697.



## **Paper 1**

### **An update on the hydroxyl airglow temperature record from the Auroral Station in Adventdalen, Svalbard (1980-2005)**

Dyrland, M. E., and F. Sigernes (2007)

**Published in: Canadian Journal of Physics**

*Can. J. Phys.*, 85(2), 143-151, doi: 10.1139/P07-040.

© 2007 Canadian Journal of Physics



# **An update on the hydroxyl airglow temperature record from the Auroral Station in Adventdalen, Svalbard (1980-2005)**

Dyrland, M. E.<sup>1</sup> and F. Sigernes<sup>1</sup>

<sup>1</sup>The University Centre in Svalbard (UNIS), N-9171 Longyearbyen, Norway  
Corresponding author: margitd@unis.no

**Abstract.** This paper reports on the daily mesospheric winter temperature series derived from ground-based spectral measurements of the hydroxyl airglow layer from the Auroral Station in Adventdalen near Longyearbyen, Svalbard (78°N, 15°E). Temperature estimates from the four latest seasons (2001-2002 to 2004-2005) have been added to the series reported by *Sigernes et al. (2003), J. Geophys Res. 108(A9), 1342*. Lomb-Scargle periodogram analyses were performed on both hourly and daily average temperatures to look for significant periods. From the daily means, ~24 and ~26 day oscillations that are consistent with a solar rotation modulation of the atmosphere were identified. Analyses of the hourly averaged data did not reveal any considerable diurnal and semi-diurnal periods in the temperatures. The 2003-2004 mesopause winter was one of the warmest reported over Svalbard during the last 25 years. It is common to observe within a few days temperature fluctuations in the range 20 – 40 K. Some years show far less variation than others. The overall daily average winter temperature is 209 K. The annual mean winter temperatures show a slightly positive temperature trend ( $+0.2 \pm 0.1$  K/yr), on the verge of being a statistically significant change in the winter mesospheric temperatures over Svalbard.

## **1. Introduction**

Measuring the temperature of the different parts of the atmosphere is considered one of the most important tasks for monitoring the global impact of anthropogenic emissions. Theoretical models have predicted an increase of the tropospheric temperature and a corresponding decrease of stratospheric and mesospheric

temperatures as a result of the increased concentration of greenhouse gases seen in the last century [e.g. *Rind et al.*, 1990]. Several empirical studies have been employed to test the models, but have failed to provide consistent results. For the mesospheric region, a negative temperature trend was first indicated in a report by *Gadsden* [1990]. It linked the increasing number of observed noctilucent clouds (NLC) with a reduction of the average temperature of the summer mesosphere, and a decrease rate of 2.5K per decade was estimated. The argument was that since ice crystals are the major part of the NLC particles, a decrease in temperature would explain why NLCs are more frequently formed and sighted at lower latitudes than earlier. The fact that the altitude of the F2 electron density peak in the ionosphere has decreased, as shown by 39 years of ionosonde observations [*Ulich and Turunen*, 1997], is also consistent with a cooling of the middle parts of the atmosphere. In-situ rocket measurements at several locations have shown that most of the middle atmosphere is cooling with values which vary from a few K at 30-40 km, 10 K at 50 km and 20 K at 60-70 km since the mid-60s [*Golitsyn et al.*, 1996]. This report also showed a record high mesopause cooling of 30 K since 1957, using temperature estimates from measurements of the hydroxyl (OH) airglow layer (centered at about 87 km) at Zvenigorod (55.7°N) and Abastumani (41.8°N). However, similar studies using the same technique both at mid latitudes [*Lowe*, 2002; *Offermann et al.*, 2003] and high latitudes [*Sigernes et al.*, 2003], have shown a trend not significantly different from zero. The last study is consistent with the trend analyses of temperatures collected by the falling sphere technique [*Schmidlin*, 1991; *Lübken*, 1999]. No indication of a large decrease of the polar summer mesopause temperature has been found [*Lübken*, 2000]. However, the polar mesosphere, compared to the mid-latitude mesosphere, is not in radiative equilibrium and large departures of polar mesospheric temperatures from radiative equilibrium of ~100K are due to dynamical driving by gravity waves [*Lindzen*, 1981; *Holton*, 1983]. Therefore, a possible cooling of the high-latitude summer mesosphere may be obscured by the gravity wave activity. These issues are far from being resolved and more long term temperature measurements from different locations and by different methods throughout the year are clearly needed.

This work is a status report of one of the longest time series of spectral measurements of the hydroxyl layer (OH) conducted from the Auroral Station in Adventdalen, Svalbard (78°N, 15°E). New temperature estimates for the winter

seasons of (2001-2002), (2002-2003), (2003-2004) and (2004-2005) are added to the already compiled data series (1980 – 2001) [*Sigernes et al.*, 2003].

## 2. Observational technique

*Meinel* [1950] was the first to identify the molecular OH band emissions as the main source for the airglow spectrum in the 0.5-4  $\mu\text{m}$  wavelength range. In-situ measurements by rocket-borne instruments have been employed to find the height structure of the airglow layer. *Baker and Stair* [1988] found it to have a thickness of 8 km and to be centred at an altitude of 87 km regardless of season or latitude. However, later studies have shown that this is a simplification and that the layer is quite dynamic, varying both in the horizontal [e.g. *Clemesha and Takahashi*, 1996] and vertical [e.g. *Kubota et al.*, 1999] direction. Although the layer exhibits wave motions, these are not yet fully understood and it is customary to assume that the OH temperatures measured represent 87 km temperatures.

Since 1983, a 1m Ebert-Fastie spectrometer has provided hydroxyl OH(6-2) spectra during the winter months and these have been analyzed to find the corresponding temperature of the airglow layer. The analysis involves constructing synthetic spectra and matching these with the observed ones. The relative intensity and width of the synthetic spectral lines are closely related to the rotational temperature as explained by *Herzberg* [1950]. For this time series the P1(2), P1(3), P1(4) and P1(5) lines of the OH(6-2) band are used. Energy term values are from *Krassovsky* [1962] and Einstein coefficients are from *Mies* [1974].

The first step of the procedure is to calculate synthetic spectra as a function of instrumental bandpass and temperature. The background is then detected by finding the optimal fit between the measured and the synthetic spectrum through iteration, until the least square error is minimal. When this is achieved, the temperature is derived from the slope of the linear fit to a Boltzmann plot (log-energy term plot) using the P1 lines. The intensities of the associated P2 lines must also follow the same linear fit, or else local thermal equilibrium has broken down, [cf. *Pendleton et al.*, 1993], and one can no longer assume that the rotational temperature of the molecule is identical to the kinetic. When this is the case the observation is discarded. The covariance between synthetic and measured spectra is also investigated to reinsure that the data are not affected by moon light, clouds or aurora, which would raise the strength and variability of the background level.

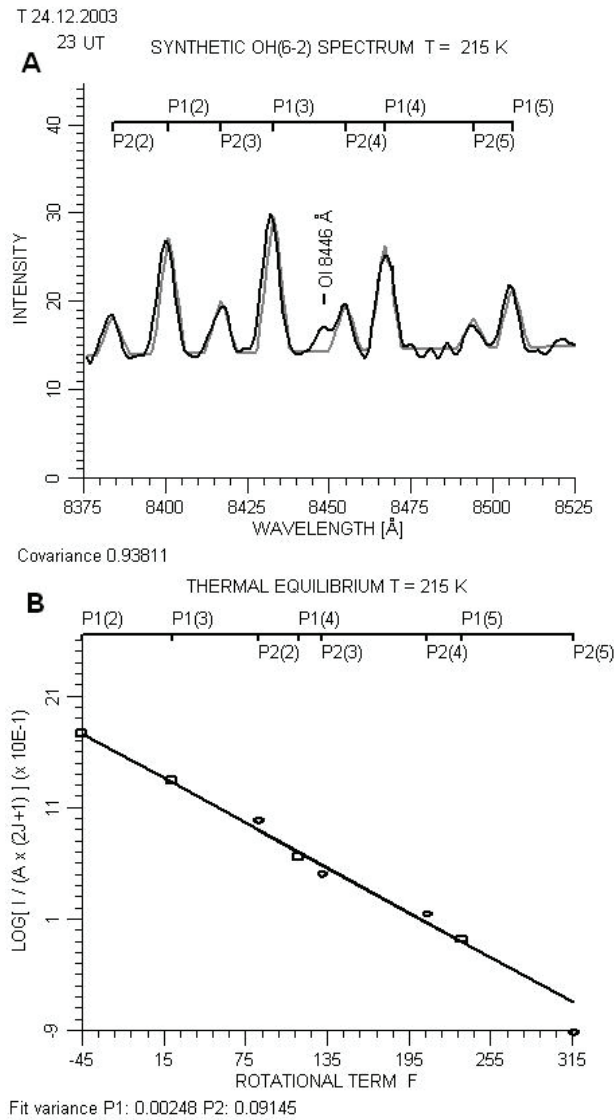


**Figure 1.** Panel (A): An hourly averaged measured- and synthetic spectrum of the OH(6-2) band from 24 December 24 2003. Each line is marked and identified according to quantum state. The curve plotted in grey is the synthetic and black the measured spectra. The auroral OI 8446 Å emission line is identified close to the P<sub>2</sub>(4) line of OH. Panel (B): Boltzmann plot for the OH(6-2) P branch of the spectrum in panel (A). The black line is the linear fit using P1 values (squares). The diamonds represent P2. A temperature of 215 K is calculated from the slope of the line. Note that a spread of the P2 values from the linear fit would indicate a departure from thermal equilibrium.

Figure 1 shows the result of a synthetic fit to a hourly averaged measured spectrum from 24 December 2003 at 23 UT. The instrument takes  $\sim 25$  s to obtain each scan, so the hourly value is an average of  $\sim 144$  scans. The covariance of the above fit is 0.94 and the log-energy term plot in panel B that shows that the linear fit of the P1 values is good, with P2 variance smaller than 0.015. On average, 44% of the total hourly spectra have covariance greater than 0.8. From these, we keep the 64% having P1 fit variance less than 0.05 and P2 fit variance less than 0.2. This leaves us with 28% of the original hourly averages. A detailed description of the temperature retrieval and instruments can be found in the work by *Sigernes et al.* [2003].

### 3. Calibration

The validity of trends estimated from long time series is difficult to assess without also having information about the instrument stability. *Sigernes et al.* [2003] presented the results of sensitivity calibrations made in 1980 and 2002. A new calibration was conducted in 2004 to check for drift since then.

The experimental setup for all of the three calibrations includes a diffuse re-emitting screen (Lambertian surface) and a 200W Tungsten lamp, both with known spectral characteristics. The lamp acts as a point light source to the screen and is mounted on top of a 5 m high tower located  $R = 30$  m away from it. The field of view of the instrument must be fully covered by the screen, since it is important to ensure that the entrance slit of the instrument is illuminated uniformly. The source of our calibration is the illuminated screen, not the lamp itself.

The calibration function of the instrument is then given as

$$K(\lambda) = \rho(\lambda) \times \left( \frac{B(\lambda)}{C(\lambda)} \right) \times \left( \frac{r}{R} \right)^2 \times \cos \alpha, \quad [\text{R}/\text{\AA}/\text{counts}]$$

where  $B$  is the known radiance (certificate) of the lamp as a function of wavelength,  $\lambda$ . The units of  $B$  are Rayleigh/Ångström ( $\text{R}/\text{\AA}$ ), initially obtained at a distance of  $r = 8.3$  m.  $C$  is the corresponding raw counts of the instrument produced by the illuminated screen. The angle of the screen is  $\alpha = 45^\circ$  and  $\rho$  is the diffuse re-emitting reflection factors of the screen.  $K$  is then a measure of the effective

throughput of the instrument as it gives the ratio of the number of photons that pass through the instrument to the number of electronic counts.

Figure 2 shows the result of the three calibrations. Note that the calibration *K80* that was conducted in 1980 used a BaSO<sub>4</sub> coated screen instead of the Spectralon surface that we use today. In addition the photomultiplier is slightly more red sensitive than in 1980, which explains the different slope. Despite this, the average fractional difference between *K80*, *K02* and *K04* is less than 3%, with larger differences (up to 8%) towards shorter wavelengths. The result is within a calibration uncertainty of 5%, and we conclude that the instrument has been operating stably with no overall degradation in sensitivity from 1980-2004.

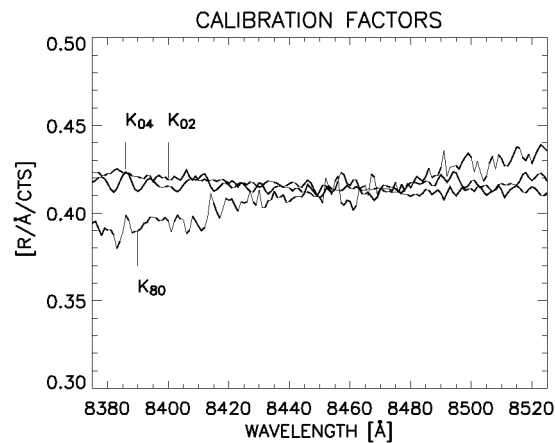


**Figure 2.** Calibration curves for the spectrometer at the Auroral Station in Adventdalen. The calibrations were conducted in 1980, 2002 and 2004.

#### 4. Results and analysis

The Svalbard temperature series consists of 746 daily averages obtained by averaging hourly deduced temperatures. At least three hourly averages must be available for each day to provide a useful daily mean. Sky conditions and operational status of the instrument determine how many hourly deduced temperatures are available for each day. Due to these limitations, the series is not uniformly sampled in time.

For the whole time series, the average daily winter temperature for 1980 to 2005 is 209K. The maximum temperature is 257K on 14 January 1983. The minimum temperature is 168K on 28 November 1989. The standard deviation is 16K.

Figure 3 shows the daily averaged temperatures from the four added seasons 2001-2002, 2002-2003, 2003-2004 and 2004-2005. They consist of 176 daily means where 85 of them are from the 2003-2004 season.

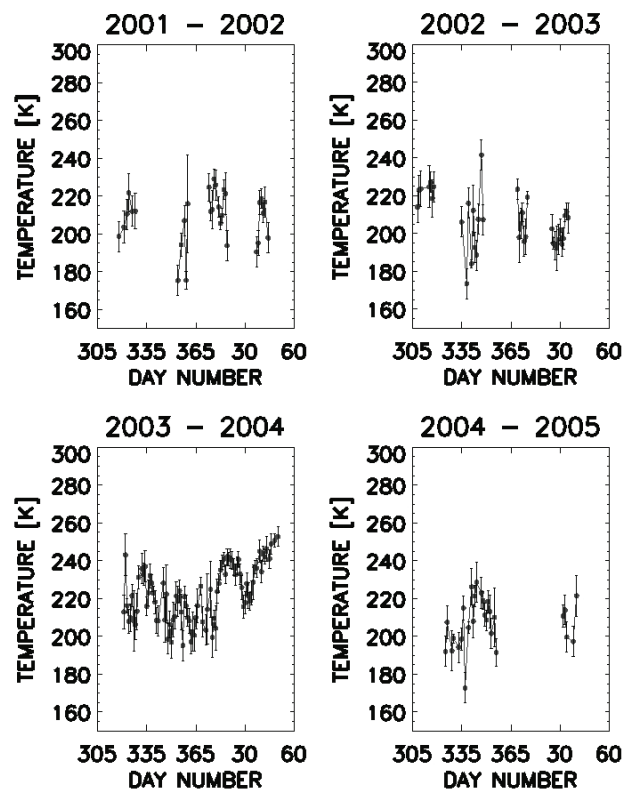


**Figure 3.** Daily mean temperatures as obtained from OH band night airglow emissions for the 2001-2002, 2002-2003, 2003-2004 and 2004-2005 winter seasons at the auroral station in Adventdalen, Svalbard. The temperatures are plotted as dark grey bullets and the error bars indicate two times the standard deviation. The  $\pm 2$  K uncertainty of the technique itself is also included.

**Table 1.** Monthly average temperatures for the 2001-2002, 2002-2003, 2003-2004 and 2004-2005 seasons from the Auroral Station in Adventdalen, Norway. The standard deviation is also included

Season	December	January
2001-2002	$194 \pm 18$ K	$216 \pm 10$ K
2002-2003	$203 \pm 19$ K	$202 \pm 10$ K
2003-2004	$213 \pm 10$ K	$226 \pm 13$ K
2004-2005	$211 \pm 14$ K	NA

Table 1 shows the average monthly temperatures of the four newly added seasons. The temperatures measured in the 2001-2002 and 2003-2004 seasons are consistent with the behaviour of low temperatures in December followed by high temperatures in January as first reported by *Myrabø* [1986].

But as noted by *Sigernes et al.* [2003], this is not consistent for all of the seasons and in 2002-2003 this tendency is not observed.

The 2003-2004 season was exceptional in several ways, both when it comes to the abundance of data and the temperature itself. It was one of the warmest winter seasons of the Svalbard temperature series, only the 1980-1981 season was reported as warmer, but at that time the temperatures were retrieved using the OH(8-3) band that have been shown to overestimate the temperatures by at least 5-6 K. In addition, only 12 daily means comprise the 1980-1981 season, so the uncertainty is rather large.

To identify periodic variations of the temperatures, Lomb-Scargle periodogram analysis [*Press and Rybicki*, 1989] was performed on both the daily and hourly data sets. The Lomb-Scargle algorithm is useful for performing periodogram analyses of non-uniformly distributed data sets. However, it assumes that there is no important clumping of data, i.e. no really large or periodic data gaps, and therefore it has to be used with care or else data gaps might be misinterpreted as temperature oscillations. Since there are only data for 3 months every year, we

exclude the long periods from the analysis. We also exclude seasons having less than 35 daily means (1980-1981, 1990-1991, 1993-1994, 1994-1995, 1995-1996, 2001-2002 and 2004-2005).

Figure 4 shows the Lomb-Scargle periodogram for the daily temperatures from the 1982-2004 time period (minus the omitted seasons). We observe significant  $\sim 24$  and  $\sim 26$  day periods having significance level  $\alpha$  smaller than 0.05. These periods are comparable to the solar rotation short-term variation (27 d). *Hall et al.* [2005] report a similar “quasi  $\sim 27$  day oscillation” of the 90 km temperature over Svalbard derived from meteor radar measurements of the ambipolar diffusion coefficient of meteor trails. From MF and LF radar data, *Luo et al.* [2001] observed such long oscillations in mesospheric winds and correlated them with variations of the UV radiation input (Mg II index and solar 10.7 cm flux), geomagnetic ( $K_p$ -index) and solar wind activity (solar wind velocity from SWE) that all exhibit 25-30 day variations. They concluded that the most probable source of the tidal oscillations is solar rotation modulated UV forcing of the underlying atmosphere (e.g. absorption of UV radiation by ozone around the stratopause).

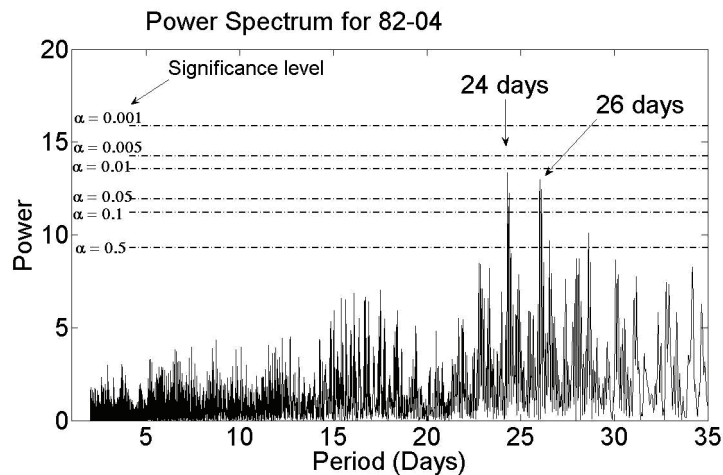


**Figure 4.** Lomb-Scargle periodogram for the daily temperatures. The continuous line is the power spectral density of the periods from 3 d to 35 d. The algorithm used is from *Press and Rybicki* [1989] implemented in a MATLAB program. The significance levels  $\alpha$  are marked by horizontal broken lines, a small value indicates a highly significant periodic signal.

A Lomb-Scargle periodogram analysis was run for the days from 1990-2005 (data from 1980-1990 are only available as daily means) having more than 15 hourly mean temperatures available for each day. The exclusion of data for the analysis was done to prevent periodic data gaps from being misinterpreted as periodic temperature variations [Press and Rybicki, 1989]. From the remaining 16 d, we were not able to identify any consistent periodic diurnal or semi-diurnal variations in the temperatures. However, running the Lomb-Scargle analysis individually on the three time periods having two successive days of data with more than 15 hourly averages per day, we found one of them showing a clear semidiurnal temperature variation (2-3 December 1998). The two other time periods did not show any statistically significant diurnal or semidiurnal variation. Diurnal and semi-diurnal variations with amplitudes in the order of as much as 30 K, have been observed in the Svalbard OH temperature data before, see, for example, refs. Myrabø [1984], Walterscheid et al [1986] and Nielsen et al. [2001]. Walterscheid et al. [1986] suggest that they are at least partly the result of the passage of a gravity wave source at lower latitudes once or twice a day. However, it has still not been possible for anyone to identify periodicities consistent for all days or seasons in the series. The main reason for this is clearly the many data gaps in the time series.

A new updated trend is calculated by adding the data from the four new seasons to the 1980 – 2001 series analyzed by Sigernes et al. [2003]. The seasonal mean temperature is calculated as an average between the monthly mean temperatures of December and January, and the estimated trend of these is plotted in Figure 5. Note that the 1980-1981 and 1982-1983 average temperatures are included in the figure, but excluded from the trend analysis since the OH(8-3) band was used to calculate the temperatures in those years.

The trend is calculated using a polynomial fit of first degree with weights defined as number of days per season divided by the standard deviation for each the yearly average temperatures. The uncertainty of the trend estimate is calculated using the bootstrap method [Efron and Tibshirani, 1993]. A small positive trend of +0.2K/year is detected and the uncertainty is  $\pm 2\delta = 0.1$  K/year.

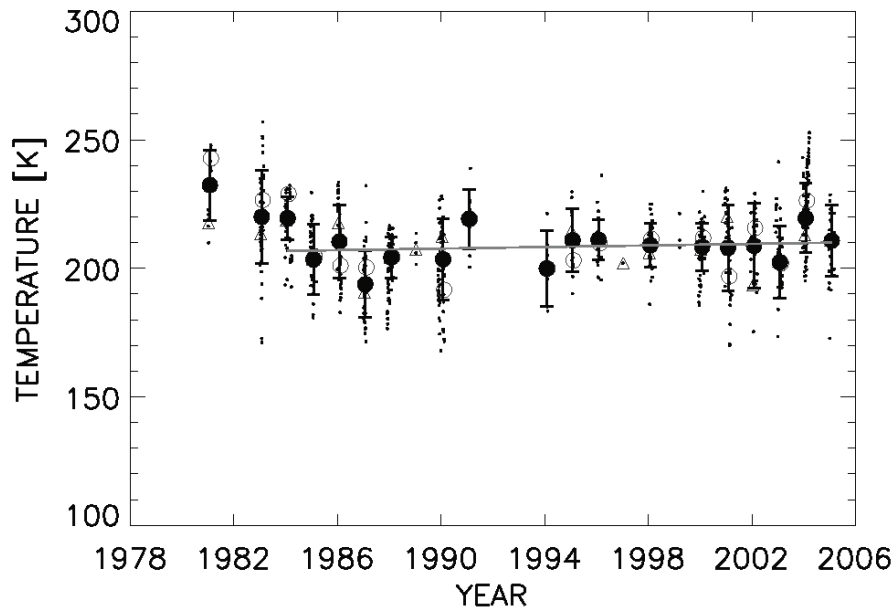


**Figure 5.** Seasonal mesospheric OH airglow winter temperature trend over Svalbard 1983-2005. The daily mean temperatures are plotted as small black dots. The monthly mean temperatures are plotted for December (grey triangles) and January (grey circles). The seasonal averages (black bullets) have the standard deviation plotted as error bars. The grey line is the estimated linear trend. The 1980-1981 and 1982-1983 temperatures are included in the figure, but excluded from the trend estimate.

The same trend was found without applying weights. The trend is statistically significant if the uncertainty is, at most, half the calculated trend. In this case it is exactly the same as half the calculated and we conclude that the trend is on the verge of being significant.

*Sigernes et al.* [2003] investigated how major and minor stratospheric warmings influenced their trend estimate. They did this by excluding months with major stratospheric warmings (found by looking at gradients in the 10 mbar temperature) and months having a standard deviation of the daily temperature greater than 10°K. The result was that only about 40% of the monthly averages could be kept for the trend analysis. When doing a similar consideration for the

four latest seasons, none of them can be included in such a modified trend estimate. There were major stratospheric warmings in December 2001, January 2003, and January 2004 [Manney *et al.*, 2005], and for the remaining months the standard deviation is larger than 10°K. So using the criteria above on the updated data sets leaves us with the same trend estimate as Sigernes *et al.* [2003]: +0.24K/year  $\pm$  0.44K.

## 5. Summary

Four more seasons of upper mesospheric winter temperatures have been obtained from spectrometric measurements of the hydroxyl airglow layer above Svalbard. Ebert-Fastie spectrometers have provided emission spectra with a resolution close to 5Å, capable of resolving the P1 and P2 lines of the OH(6-2) and (8-3) bands. Sigernes *et al.* [2003] analyzed the dataset up to 2001. The four new seasons show much of the same seasonal behaviour as the previously reported seasons. The day-to-day temperatures show relatively large maxima with amplitudes close to 20K lasting for a few days to a week or longer. The average daily temperature is 209K for the whole period. The standard deviation is 16K, indicating that the mesospheric temperature variations over Svalbard in winter are extremely high. The 2003-2004 season was special being one of the warmest reported in the 25 years of Svalbard measurements. The sky conditions were exceptionally good and this allowed derivation of many hourly and daily averages. Lomb-Scargle periodogram analyses of the daily averaged temperatures showed ~24 and ~26 periods, that might be associated with the 27 d solar rotation period. No consistent diurnal or semi-diurnal variations were identified by analysis of the hourly averaged data. The physical processes governing the temperature oscillations are not clarified and searching for correlations with solar and atmospheric parameters should be a task for future studies. An updated trend analysis of the yearly averaged OH(6-2) winter temperatures between 1983-2005 found a trend of +0.2  $\pm$  0.1 K/year. However, this trend was calculated without taking major and minor stratospheric warming events into account. A task for future work on the Svalbard series should obviously include developing a method where such effects are accounted for without having to throw away as much data as we do now. Further analyses should also include investigating the effect the non-uniform distribution of data has on the trend estimate.

**Acknowledgements.** The Auroral station in Adventdalen is operated by The University Centre on Svalbard (UNIS). We deeply appreciate the support of the Optical group at the Geophysical Institute, University of Alaska, who own the instrument. Thanks also to Brett Shoelson for distributing matlab-code for the Lomb-Scargle analysis.

## References

- Baker, D. J., and A. T. Stair, Jr. (1988), Rocket measurements of the altitude distributions of the hydroxyl airglow, *Phys. Scr.*, 37, 611 - 622.
- Clemesha, B. R, and H. Takahashi (1996), Rocket-borne measurements of horizontal structure in the OH(8,3) and NaD emissions, *Adv. Space Res.*, 17(11), 81-85.
- Efron, B., and R. T. Tibshirani (1993), An Introduction to the Bootstrap, *Chapman & Hall, New York*.
- Gadsden, M. (1990), A secular change in noctilucent cloud occurrence, *J. Atmos. Terr. Phys.*, 52, 247 - 251.
- Golitsyn, G. S., A. L. Semenov, N. N. Shefov, L. M. Fishkova, E. V. Lysenko, and S. P. Perov (1996), Long-term temperature trends in the middle and upper atmosphere, *Geophys. Res. Lett.*, 23, 1741 - 1744.
- Herzberg, G. (1950), Molecular Spectra and Molecular Structure I. Spectra of Diatomic Molecules, *D. van Nostrand Company, Inc., New York*.
- Hall C. M., T. Aso, M. Tsutsumi, J. Höffner, F. Sigernes and D. A. Holdsworth (2005), Neutral air temperatures at 90 km and 70°N and 78°N, *Submitted to Radio Science*.
- Holton, J. R. (1983), The influence of gravity wave breaking on the general circulation of the middle atmosphere, *J. Atmos. Sci.*, 40, 2497 – 2507.
- Krassovsky, V. I., N. N. Shefov, and V. I. Yarin (1962), Atlas of the Airglow Spectrum 3000-12,400 Å, *Planet. Space Sci.*, 9, 883 - 915.

- Kubota, M., M. Ishii, K. Shiokawa, M. K. Ejiri, and T. Ogawa (1999), Height measurements of nightglow structures observed by all-sky imagers, *Adv. Space Res.*, *24*, 593-596.
- Lindzen, R. S. (1981), Turbulence and stress due to gravity wave and tidal breakdown, *J. Geophys. Res.*, *86*, 9707-9714.
- Lowe, R. P. (2002), Long-term trends in the temperature of the mesopause region at mid-latitude as measured by the hydroxyl airglow, *paper presented at We-Heraeus seminar on trends in the upper atmosphere*, pp. 32, Kühlungsborn, Germany.
- Luo, Y., A. H. Manson, C. E. Meek, K. Igarashi and Ch. Jacobi, Extra long period (20-40 day) oscillations in the mesospheric and lower thermosphere winds: observations in Canada, Europe and Japan, and considerations of possible solar influences (2001), *J. Atmos. Solar-Terr. Phys.*, *63*, 835-852.
- Lübken, F.-J. (1999), Thermal structure of the Arctic summer mesosphere, *J. Geophys. Res.*, *104*(D8), 9135 - 9149.
- Lübken, F.-J. (2000), Nearly zero temperature trend in the polar summer mesosphere, *Geophys. Res. Lett.*, *27*(21), 3603 - 3606.
- Manney G. L., K. Krüger, J. L. Sabutis, S. A. Sena and S. Pawson (2005), The remarkable 2003-2004 winter and other recent warm winters in the Arctic stratosphere since the late 1990s, *J. Geophys. Res.*, *110*, D04107 doi:10.1029/2004JD005367.
- Meinel, A. B. (1950), OH emission bands in the spectrum of the night sky II, *Astrophys. J.*, *112*, 120-130.
- Mies, F. H. (1974), Calculated vibrational transition probabilities of OH( $X^2\Pi$ ), *J. Molec. Spectrosc.*, *53*, 150-188.
- Myrabø, H. K. (1984), Temperature variation at mesopause levels during winter solstice at 78°N, *Planet. Space Sci.*, *32*(2), 249.
- Myrabø, H. K. (1986), Winter-season mesopause and lower thermosphere temperatures in the northern polar region, *Planet Space Sci.*, *34*, 1023 - 1029.

- Nielsen, K. P., C. S. Deehr, E. Raustein, Y. Gjessing, and F. Sigernes, Polar OH-airglow temperature variations in the 87/88 winter (2001), *Phys. Chem. Earth*, 26, No. 6, 405-410.
- Offermann, D., M. Donner, P. Knieling, K. Hamilton, A. Menzel, B. Naujokat, and P. Winkler (2003), Indications of long-term changes in middle atmosphere transports, *Adv. Space Res.*, 32, 1675-1684.
- Pendleton, W. R., Jr., P. J. Espy, and M. R. Hammond (1993), Evidence for Non-Local-Thermodynamic-Equilibrium Rotation in the OH Nightglow, *J. Geophys. Res.*, 98(A7), 11567-11579.
- Press, W. H., and G. B. Rybicki (1989), Fast algorithm for spectral analysis of unevenly sampled data, *Astrophys. J.*, 338, 277-280.
- Rind, D., R. Suozzo, N.K. Balanchandra, and P. Prather (1990), Climate change and the middle atmosphere, 1. The doubled CO<sub>2</sub> climate, *J. Atmos. Sci.*, 47, 475-494, doi: 10.1175/1520-0469.
- Schmidlin, F. J., H. S. Lee, and W. Michel (1991), The inflatable sphere: A technique for the accurate measurements of the middle atmosphere temperatures, *J. Geophys. Res.*, 96, 22673 - 22682.
- Sigernes, F., N. Shumilov, C. S. Deehr, K. P. Nielsen, T. Svenøe, and O. Havnes (2003), The Hydroxyl rotational temperature record from the Auroral Station in Adventdalen, Svalbard (78°N, 15°E), *J. Geophys. Res.*, 108(A9), 1342, doi: 10.1029/2001JA009023.
- Ulich, T., and E. Turunen (1997), Evidence for long-term cooling of the upper atmosphere in ionosonde data, *Geophys. Res. Lett.*, 24, 1103 - 1106.
- Walterscheid, R. L., G. G. Sivjee, G. Schubert, and R. M. Hamwey (1986), Large-amplitude semi diurnal temperature variations in the polar mesopause: evidence of a pseudotide, *Nature*, 324, 347 - 349.



## **Paper 2**

### **The response of OH airglow temperatures to neutral air dynamics at 78°N, 16°E during the anomalous 2003-2004 winter**

Dyrland, M. E., F. J. Mulligan, C. M. Hall, F. Sigernes, M. Tsutsumi, and C. S. Deehr (2009a)

**Submitted to: Journal of Geophysical Research**

Manuscript # 2009JD012726

(Revised version in press, *J. Geophys. Res.*, Dec. 2009.

© 2009 American Geophysical Union)



# The response of OH airglow temperatures to neutral air dynamics at 78°N, 16°E during the anomalous 2003-2004 winter

Dyrland, M. E.<sup>1</sup>, F. J. Mulligan<sup>2</sup>, C. M. Hall<sup>3</sup>, F. Sigernes<sup>1</sup>, M. Tsutsumi<sup>4</sup>, and C. S. Deehr<sup>5</sup>

<sup>1</sup>The University Centre in Svalbard, N-9171 Longyearbyen, Norway

<sup>2</sup>National University of Ireland Maynooth

<sup>3</sup>Tromsø Geophysical Observatory, University of Tromsø, Norway

<sup>4</sup>National Institute of Polar Research, Tokyo, Japan

<sup>5</sup>Geophysical Institute, University of Alaska Fairbanks, USA

Corresponding author: [margit.dyrland@unis.no](mailto:margit.dyrland@unis.no)

**Abstract.** OH brightness temperatures from the mesopause region derived from TIMED/SABER satellite temperature profiles are compared with OH(6-2) rotational temperatures measured by spectrometer from Longyearbyen (78°N, 16°E) during the winter 2003-2004. Both sets display similar relative variations, but a positive bias of  $14 \pm 9$  K is found in favor of the satellite temperatures. We examine the temperature response to neutral air dynamics observed in meridional and zonal winds measured by meteor radar. Vertical profiles of 1.6  $\mu\text{m}$  OH volume emission rates from SABER reveal that the unusually high temperatures observed during January and February 2004 (240-250 K) correspond with a very low and bright OH layer. Significant linear correlations are found between meridional wind, OH temperature and peak altitude. These data support the theory that the high temperatures result from an anomalously strong upper stratospheric vortex which confined air to the polar regions, coupled with meridional transport and led to a strong downwelling of atomic oxygen rich air thereby lowering the altitude of the OH layer. The SABER data reveal that the reformation of the OH layer at approximately 78 km altitude accounted for an increase in temperature of approximately 15 K, while the remaining temperature increase (20-35 K) is attributed to adiabatic heating.

## 1. Introduction

The Arctic winter of 2003-2004 has been reported as remarkable from several points of view and has been the subject of many studies. *Manney et al.* [2005] described how a disruption of the polar vortex and an associated sudden stratospheric warming (SSW) persisted at the low and middle stratosphere throughout the whole winter, while the upper stratospheric vortex quickly reformed in mid-January and became the strongest on record by mid-February. This resulted in anomalously high temperatures in the lower and middle stratosphere and an unusually cold upper stratosphere.

At the upper mesospheric level, the dominant circulation pattern during an Arctic winter consists of eastward directed zonal winds (westerlies) and poleward meridional flow from summer pole to winter pole [*Andrews et al.*, 1987]. During SSW events, gravity and planetary waves disrupt the polar stratospheric vortex which leads to a warming of the stratosphere of up to 70 K at the 10 hPa level (~30 km) [*Schoeberl*, 1978] and to a reversal of the mean zonal wind in the case of a major SSW. The large-scale effects of the SSW on the mesospheric temperature and wind field for the 2003-2004 winter were studied by *Shepherd et al.* [2007] and *Mukhtarov et al.* [2007] for latitudes ranging from the tropics up to 70°N. They observed a reduction of the upper mesospheric temperature and a reversal of the zonal wind that preceded the changes in the stratosphere. This is consistent with previous studies of stratospheric warming/mesospheric cooling events made by use of ground-based optical measurements of OH rotational temperatures, models and radars [e.g. *Walterscheid et al.*, 2000; *Hoffman et al.*, 2007]. The implication is that there is a downward propagation from the mesosphere-lower thermosphere (MLT) to the stratosphere. However, other authors have found no correlation between stratospheric temperatures and the rotational temperature of the OH Meinel band at ~87 km [*Siskind et al.*, 2005], indicating that there might be an altitude limit to how far these events affect the atmosphere or that other features of the OH layer dynamics hide the variations. It is important, therefore to continue to study these events in order to obtain a more complete understanding of the processes causing them.

Rotational temperatures derived from optical measurements of the OH Meinel airglow bands in the spectrum of the night sky have been used extensively as a proxy for the neutral temperature in the uppermost part of the mesosphere, the so-

called mesopause region (80-100 km) [*Beig et al.*, 2003, and references therein]. Temperatures derived from spectrometric measurements of the OH(6-2) Meinel band measured above Longyearbyen, Svalbard (78°N, 16°E) comprise one of the longest records of mesopause region temperatures in the world [*Sigernes et al.*, 2003]. In a paper giving an update on this temperature series we reported unusually high OH(6-2) rotational temperatures for the 2003-2004 season compared to the whole series from the early 1980s to 2005 [*Dyrland and Sigernes*, 2007]. In a recent paper, *Winick et al.* [2009] noted that while several authors have documented abnormal conditions of various sorts in the 2003-2004 winter, none had been related specifically to OH. Using data from the SABER (Sounding of the Atmosphere by Broadband Emission Radiometry) instrument on the TIMED (Thermosphere Ionosphere Mesosphere Energetics and Dynamics) satellite they gave a global picture of the OH layer characteristics from late-January through February 2004, and showed that the very high OH temperatures were correlated with an unusually low and bright OH layer that inhibited significant zonal asymmetries. They argued that the lowered OH layer was due to the anomalously strong upper stratospheric vortex that formed after the SSW. The vortex supported increased downwelling of oxygen rich air and displaced the OH layer to a lower altitude than normal. However, their study was limited by the period of time that SABER was viewing northwards and could thus only report OH temperatures and heights from mid-January 2004, thereby missing the actual time prior to and during the SSW.

In this paper we examine OH temperature variability as measured by a ground-based spectrometer during the Arctic polar night of 2003-2004 and combine the data with SABER measurements to make a complete temperature record for this season. Supported by mesopause region wind data obtained by meteor radar from the same site, we establish the impact of the unusual atmospheric conditions on the OH layer and we relate it to the neutral air dynamics observed above the high-latitude location Longyearbyen (78°N). We identify the time of onset of the high temperatures and we compare the observations with current theories of the dynamics at high latitudes. Using OH layer peak altitudes and OH brightness weighted temperatures derived from SABER measurements, we quantify the effect the lowering of the layer had on the temperature. For the first time rotational

temperatures derived from the OH(6-2) band are compared with satellite temperatures measured by SABER at such a high latitude.

## 2. Instruments and data retrieval

The main data presented in this paper are temperatures retrieved from OH(6-2) spectra measured by a ground-based spectrometer, OH brightness temperatures and OH layer peak altitudes measured by the satellite instrument SABER, and zonal and meridional winds measured by the NSMR radar (Nippon/Norway Svalbard Meteor Radar). The following paragraphs provide a short overview of and references to the instruments and data retrieval.

The OH(6-2) spectra are measured above Longyearbyen, Svalbard (78°N, 16°E). The Ebert-Fastie spectrometer used to obtain these spectra, the theory and practice behind the temperature retrieval, and the temperature series (1980-2005) have been thoroughly described and discussed in previous papers [e.g. *Sivjee and Hamwey, 1987; Sigernes et al., 2003*]. Some improvements have been made to the analysis since our most recent report [*Dyrland and Sigernes, 2007*]. For this study the transition coefficients used in the temperature retrieval have been changed to those calculated by *Langhoff et al. [1986]*. This change relative to previous analyses of data from this location is based on the study of *French et al. [2000]* who found that set to be closest to their measured values for the OH(6-2) band.

OH equivalent temperatures (brightness temperatures) were calculated from each SABER temperature profile that satisfied a “coincidence” criterion with the Longyearbyen data. Spatially, this means SABER profiles with a tangent point at an altitude of  $87 \pm 8$  km that have geographic coordinates within  $78 \pm 5^\circ\text{N}$ ,  $16 \pm 10^\circ\text{E}$  (this corresponds to a circle of approximately 600 km centered on the observing site at Longyearbyen). The brightness temperatures were determined as described in *Mulligan and Lowe [2008]* using the OH  $1.6 \mu\text{m}$  volume emission rate (VER) measured simultaneously by SABER to weight the CO<sub>2</sub> vibrational temperature profiles [*Mertens et al., 2004*]. The OH  $1.6 \mu\text{m}$  VER signal covers the spectral interval  $1.56\text{-}1.75 \mu\text{m}$  and thus includes most of the  $\Delta v = 2$  bands OH(4-2) and OH(5-3). In the following description, we will use the phrase “SABER temperatures” to refer to OH equivalent brightness temperatures derived from temperature profiles produced by version 1.07 of the SABER analysis software.

From the OH VER profiles, the altitude of the emission layer and the integrated rate of emission can be computed. The peak altitude was chosen to be the peak altitude of the Gaussian that best fitted the measured OH VER profile, following the method that *Liu and Shepherd* [2006] used when analyzing WINDII satellite data. The corresponding integrated emission rate was obtained by computing the integral of the area under the OH VER profiles.

Zonal and meridional winds at the mesopause level were obtained from analysis of meteor echoes measured by the Nippon (NIPR)/Norway Svalbard Meteor Radar (NSMR). The NSMR is of the type often referred to as a meteor wind radar (MWR) or recently simply as a meteor radar. The system operates at 31MHz, and is co-located with the ground-based optical instruments at Longyearbyen. A description of the system may be found in *Hall et al.* [2002] and *Holdsworth et al.* [2004]. MWRs illuminate a large region of the sky and echoes from meteor trains are detected by receivers arranged as an interferometer. Descriptions of how winds are determined may be found in e.g. *Aso et al.* [1979], *Hocking et al.* [2001] and *Tsutsumi et al.* [1999]. A MWR at high latitude suffers less from strong diurnal variation of meteor rate than at low latitude, and therefore it is possible to obtain a time resolution of 30 min. The resulting 30 min average winds represent, however, a spatial averaging over perhaps 200 km at the peak echo occurrence height of 90 km. For this study the measured wind data have been averaged over bins spanning 1 day and 2 km in height in the altitude range 74-100 km.

### **3. Comparison of OH(6-2) and SABER temperatures**

The SABER and OH(6-2) temperatures for the 2003-2004 winter season are shown in the top panel of Figure 1 as dark blue circles and green plusses respectively. The daily averaged temperatures for each set are indicated as a solid line in their respective color. Unfortunately there are no SABER temperatures available from mid-November to mid-January. This is because the yaw periods of the satellite are such that it spends 60 days looking northward followed by 60 days looking southward. The southward looking 60 days are approximately day 325 of year  $n$  until day 15 of year  $n+1$ . Unfortunately, this coincides with the main period of observation for the ground-based spectrometer in Longyearbyen.

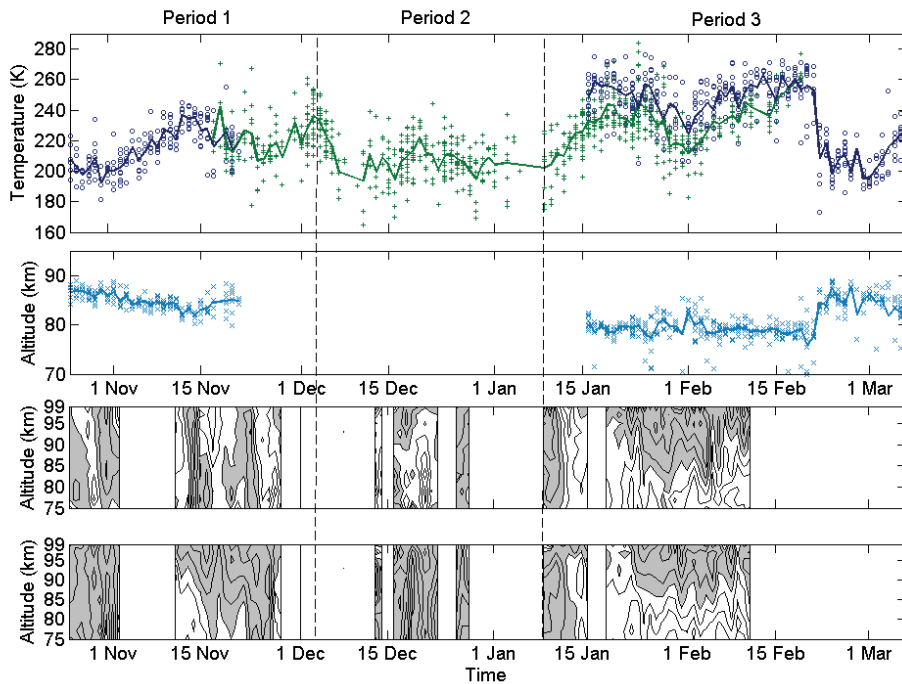


**Figure 1.** Top panel: OH(6-2) temperatures from Longyearbyen ( $78^{\circ}\text{N}$ ,  $16^{\circ}\text{E}$ ) (green plusses), and OH equivalent temperatures (dark blue circles) from SABER (v1.07) at  $78\pm 5^{\circ}\text{N}$ ,  $16\pm 10^{\circ}\text{E}$  for the winter season 2003-2004. Daily mean OH(6-2) temperatures and SABER OH equivalent temperatures are shown as solid lines in green and dark blue, respectively. Second panel: SABER OH peak altitudes (light blue crosses). The daily averaged values are shown as a light blue solid line. Third panel: zonal wind measured by the NSMR meteor radar binned in 2 km bins from 74-100 km and daily averaged. White shading indicates eastward winds, while grey shading indicates westward winds. Contour lines are shown for levels of 20 m/s. Bottom panel: meridional winds measured for the same ranges as the zonal wind.

Due to exceptionally good observing conditions, an unusually large number of OH(6-2) temperatures were available for analysis in the period January 16 to February 19, when SABER was looking northward [Dyrland and Sigernes, 2007]. This allowed us to make a comparison of the two temperature sets despite the disadvantageous SABER yaw cycle.

From the top panel of Figure 1 it is clear that the relative variations of the SABER and OH(6-2) temperatures are very similar. The mean daily averaged

temperature for the overlap period is  $247 \pm 9$  K for SABER and  $233 \pm 11$  K for OH(6-2) giving a mean difference,  $\overline{T_{\text{SABER}} - T_{\text{OH(6-2)}}}$ , of  $14 \pm 9$  K. The linear correlation coefficient between the daily averaged temperature series is 0.644. Applying a three-day running filter to the data sets to smooth the day-to-day variation increases the correlation coefficient to 0.921.

The SABER temperatures are vibrational temperatures from CO<sub>2</sub> weighted by profiles of OH vertical emission rates, whereas the OH(6-2) values are rotational temperatures. Using the Keck data, *Cosby and Slanger* [2007] have shown that OH rotational temperatures can differ by as much as 15 K (and more) when using different bands. The different field-of-view of the two instruments will also contribute to differences in the relative variations. OH(6-2) spectra are obtained from the 5 degree field-of-view spectrometer and are integrated vertically, while the SABER instrument has a 2 km vertical field of view, but maybe 500 km in the horizontal and integrates along the limb. In these respects, it is not too surprising that there is a mean difference of as much as 14 K in absolute value between of the two, and deviations between the relative variations. However, the sign of this offset is a bit surprising. Several authors have compared SABER data with OH temperatures measured from mid-latitudes before, and most have found the SABER equivalent temperature to be colder than the rotational temperature by 4-9 K [e.g. *López-Gonzales et al.*, 2007; *Mulligan and Lowe*, 2008, and references therein]. No other season had such a long overlap period between SABER and spectrometer measurements as 2003-2004, but from 25 January to 4 February 2003 there were 9 days when the two coincided. Comparison of the daily mean temperatures shows a positive bias of 12 K for SABER. The mean OH layer temperature for that time period was  $212 \pm 7$  K and  $200 \pm 12$  K for SABER and OH(6-2) temperatures, respectively. Thus we find that even in the case of a “normal” year, a SABER temperatures are significantly warmer than the ground-based measurements. We have also tested the hypothesis that there might be a diurnal bias of the two data sets used in the study reported here, but even when only choosing data that were coincided within a 30 minute window, the large positive bias for SABER remained.

To our knowledge no thorough comparison of SABER and rotational OH temperatures from high Arctic latitudes has been reported to date. However, from Figure 1 in the paper by *Siskind et al.* [2005] we see that SABER are higher than

rotational OH(4-2) temperatures measured at Rothera, Antarctica (67.6°S, 68.1°W) by an average of ~4 K. It would be interesting to examine other comparisons of SABER temperatures with rotational temperatures derived from OH spectra to check whether the high-latitude bias observed in two cases cited is sustained and to find the reason for it.

Keeping in mind the 14 K offset, we consider the two temperature series in combination as a continuous record of OH temperatures from Longyearbyen for the 2003-2004 winter.

#### **4. Temperature and wind variations during 2003-2004**

To understand the temperature variations of the 2003-2004 winter it is critical to have information about the altitude of the OH emission layer [*Kumar et al.*, 2008]. The OH layer peak altitudes corresponding to the SABER temperatures are plotted in the second panel of Figure 1. The two lower panels show the NSMR zonal and meridional winds, respectively. We divide the winter into three different periods according to the characteristics of the OH layer.

We first look at the period from 25 October to 3 December 2003 marked as Period 1 in Figure 1. During the start of this period the OH temperature was relatively low (~200 K), but increased from 1 November. The low temperatures coincided with an equatorward meridional wind which is consistent with upwelling and adiabatic cooling [*Shepherd et al.*, 2006]. Looking at two top panels of Figure 1 it is clear that the rise in temperatures of about 35 K during the 14 day period after 1 November coincided with a reduction in the altitude of the OH layer peak of 5 km. Unfortunately, wind measurements are not available for most of this event. We can however get a clue by looking at the period 11-14 November, the zonal wind was eastward and meridional wind poleward below 90 km, which is consistent with downwelling and adiabatic warming. After 14 November the temperature decreased somewhat and the meridional wind turned equatorward.

In period 2, from 4 December 2003 to 8 January 2004, the OH temperature decreased rapidly by ~40 K during the first few days. Unfortunately there are no meteor radar wind or SABER data available for this period. However, *Mukhtarov et al.* [2007] report a similar negative excursion of the ~90 km temperature starting around 1 December, indicating that it is not just a local feature. They attribute it to strong disturbances in the mean zonal wind in the mesopause region (80-90 km)

seen in radar measurements averaged for 60-70°N. According to them, these are actually the first signs of the enhanced planetary wave activity that led to the major SSW occurring in late December-early January. The actual reversal of the stratospheric zonal wind at 60°N and thus onset of the SSW was on 2 January 2004 [Manney *et al.*, 2005]. Mukhtarov *et al.* [2007] identified it occurring 10-14 days earlier in ~80 km winds measured by radars at 63-69°N. So in a way there seem to be two dates that can be associated with onset of the SSW in the MLT/mesopause region: one around 4 December associated with enhanced planetary wave activity that is believed to be the driver of the SSW event and one around 24 December when the zonal wind reversed again. We have already discussed the signatures in the OH temperatures for the first event. The temperature data around 24 December do not reveal a similar large decrease of temperature, although several negative excursions in the order of 20 K are seen around that time. However, looking at the wind data we observe that from 15-23 December the zonal wind is mainly eastward, while it has reversed and is westward at 26-28 December. This is consistent with what is the expected signature of the SSW in this region. The data gaps are especially unfortunate in this period, since they make it difficult to assign changes in OH temperature and winds to the SSW, but at least we can show that the general picture drawn by Mukhtarov *et al.* [2007] is also valid for our latitude. The temperature remained relatively low for the rest of this period and the equatorward meridional wind observed is consistent with this cooling.

Period 3 from 9 January to 7 March 2004 is the most interesting period of this winter. We believe that the westward wind seen in the third panel from 9-12 January is likely to be the remains of the wind reversal at mesopause level associated with the SSW and stratospheric vortex disruption. This corresponds well with the recovery of the upper stratospheric vortex and eastward wind by 18 January reported by Manney *et al.* [2005], and which then remained strong until mid-March. SABER and OH(6-2) temperatures increased and remained high during this period. The zonal and meridional wind changed direction at 13 January from westward/equatorward to eastward/poleward, which is consistent with a re-establishment of the polar vortex and occurred at the same time as the OH(6-2) temperature began to increase. The OH layer peak altitude shown in the second panel of Figure 1 decreased at the beginning of Period 3 and remained low throughout the period. The reduction in temperature and corresponding rise of the

OH layer peak around 1 February is probably associated with the shorter major SSW in late January [Manney *et al.*, 2005]. After 1 February the temperature increased again achieving values greater than 250 K and the OH layer peak altitude dropped below 78 km. Unfortunately, there are no OH(6-2) temperatures available after 22 February and no winds after 10 February. The SABER data show that the temperature dropped by about 50 K and the OH layer peak altitude increased correspondingly, in a very short time near 21 February. The close relationship between OH height and temperature is especially clear here. The large asymmetries in the OH layer temperature, emission and height reported by Winick *et al.* [2009] would be interesting to study in relation to this abrupt change to see whether temporal or spatial variability or a combination is the cause for it. To do this, we would need data from other stations at different longitudes and latitudes, so it is not the scope of this paper.

## 5. Discussion

To illustrate the OH layer variations observed, we have plotted monthly averaged SABER temperature profiles for selected months of 2003 and 2004 in the left panels of Figure 2. In the right panels the corresponding monthly averaged SABER OH VER 1.6 $\mu$ m emission profiles are shown. The solar zenith angle criterion  $SZA > 105$  ensures data are obtained during darkness. From the emission profiles it is clear that the OH layer over Longyearbyen during January and February 2004 is very low compared to the more “normal” year of 2003 when the peak altitude was around 87 km and the temperatures lower. The VER of the OH layer in January and February 2004 is approximately twice its value in the same months of 2003.

The coincidence of high temperatures with a reduction in altitude and an increase in the brightness of the OH layer has been observed previously. Yee *et al.* [1997] have shown that the peak emission altitude of the OH emission is inversely correlated with the strength of the emission. This inverse relationship was also observed by Winick *et al.* [2009] in their SABER data. Winick *et al.* [2009] noted that the OH layer altitude and the temperature at the OH layer are also inversely related. They showed that during the period 26-31 January 2004, the OH layer was not zonally symmetric, and that for high-latitudes stations eastward of 50° East the layer showed no unusual behavior. At 16°E, Longyearbyen was approximately halfway between the undisturbed region and the highly disturbed region at 50°W.

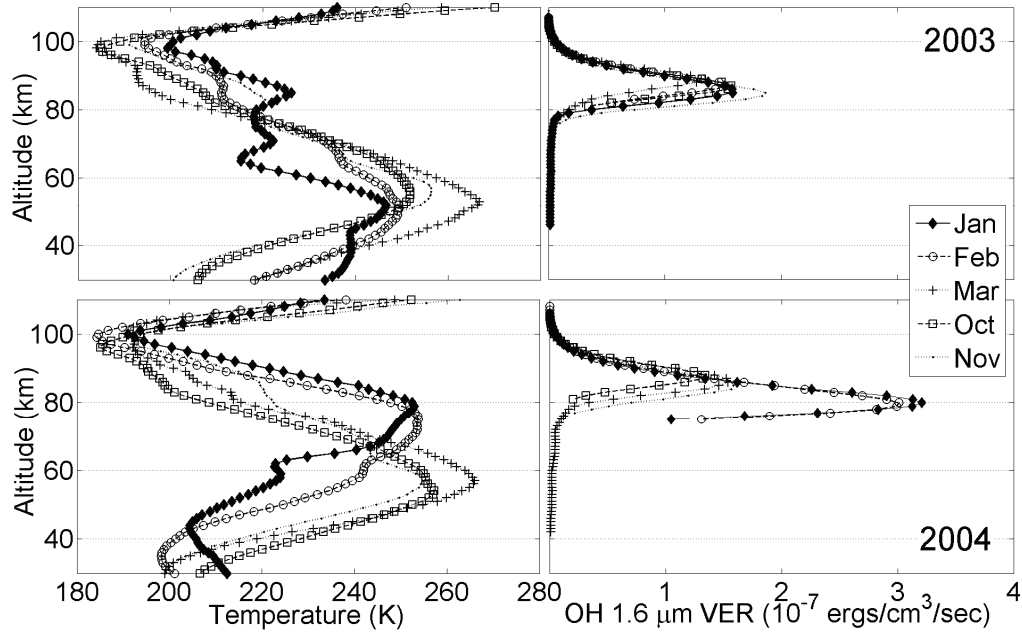


**Figure 2.** Left panels: monthly averaged SABER temperature profiles for January, February, March, October and November 2003 (top panel) and 2004 (bottom panel). Data shown are from the altitude range 30-110 km above Longyearbyen and for  $SZA > 105$ . Right panels: monthly averaged SABER OH VER 1.6 $\mu$ m profiles for the same months of 2003 (top panel) and 2004 (bottom panel).

From our ground based measurements we can confirm the existence of the unusually low OH layer at the longitude of Longyearbyen. The formation of the OH layer at lower altitudes is likely to be the result of downwelling of atomic oxygen rich air to lower heights as suggested by *Winick et al.* [2009].

In a study of the correlation between airglow temperature and emission rate at the high-latitude location Resolute Bay (75° N), *Cho and Shepherd* [2006] found evidence of a common process for all dynamical perturbations of the airglow layer, and argued this process is simply vertical motion. This is supported by the work of *Marsh et al.* [2006] where they compared SABER observations of OH emission rates with a three-dimensional chemical model. They found that at the height of peak emission, variations are predominantly caused by changes in atomic oxygen resulting from vertical transport. This leads to an increase in ozone which together

with the higher densities leads to an increase in the band brightness and temperature.

To get an idea about the quantitative effect of the lowered OH layer on the temperature, we can look at the temperature profiles in the left panels of Figure 2. From these we see that the environmental lapse rate is approximately 1.5 K/km in the altitude range 60-100 km. Of the 35 K temperature increase observed in the beginning of Period 1, we estimate that about 7.5 K is due to the OH layer peak occurring 5 km lower down, according to the environmental lapse rate observed. Correspondingly, of the overall ~50 K increase of temperature from late October to mid February, we ascribe about 15 K to the close to 10 km lowering of the OH layer, as observed in top two panels of Figure 1. The remaining temperature increase is then attributed to adiabatic heating of the subsiding air following the adiabatic lapse rate which is approximately 9.5K/km at mesopause heights [c.f. *Sherman and She, 2006*]. Seasonal variability and other shorter time scale variations that may also influence the temperature (e.g. planetary waves, gravity waves and tides) are not quantified in this paper.

The strong poleward meridional wind observed at the OH layer height (~80 km) during this period is probably also contributing to the emission intensity level by transporting odd oxygen species from their source region to the high-latitudes (where there is no winter production of O by photodissociation [*Myrabø and Deehr, 1984*]), as well as increasing downwelling which further increases adiabatic warming. To test for a possible coupling, we calculated the correlation coefficients between daily averaged meridional winds measured by the meteor radar at different heights and the OH(6-2) temperatures for the 55 days that the measurements coincided between 17 November 2003 and 11 February 2004. Figure 3 shows the correspondence between temperature and the wind at 84-86 km height, for which we found the largest correlation. The correlation coefficient is 0.70 with a probability for random occurrence  $<10^{-8}$ . This means that around 50% of the variation in temperature can be explained by the variations in the meridional wind direction and strength.

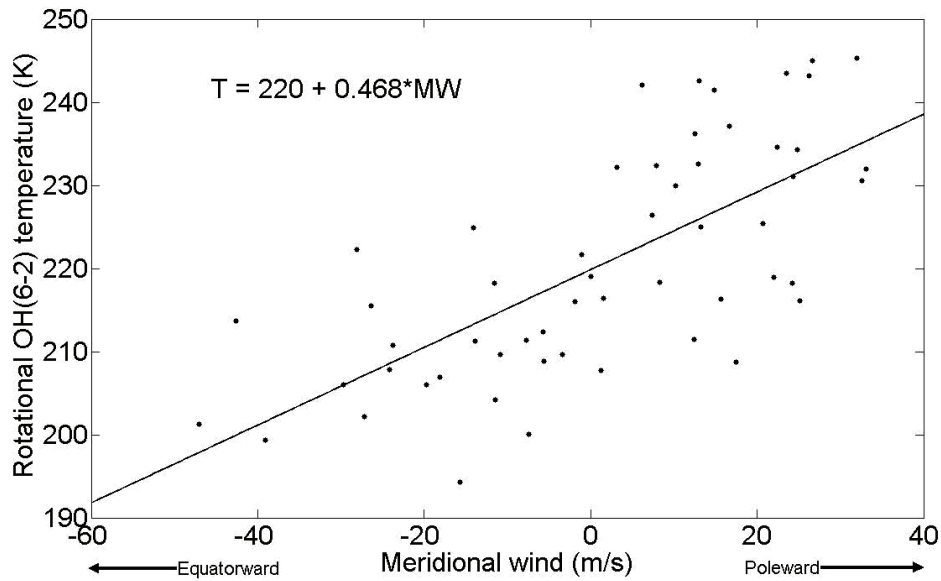


**Figure 3.** Scatter diagram of the 55 coinciding OH(6-2) temperatures and meridional wind measurements from Longyearbyen between 17 November 2003 and 11 February 2004. The solid line shows the best linear fit to the data points.  $T$  denotes the temperature and  $MW$  the value for the meridional wind. The correlation coefficient is 0.70, with the probability for random occurrence  $<10^{-8}$ .

From the figure we see how a poleward wind is consistent with a higher temperature, while an equatorward wind gives a lower temperature. This value is comparable to the findings of *Espy et al.* [2003] who reported a correlation of -0.61 between meridional wind measured by MF radar and OH(4-2) rotational temperatures at Rothera, Antarctica. The negative sign of their correlation is due to poleward wind in that hemisphere being defined as negative. They found a slope of  $-0.71 \text{ K/ms}^{-1}$ . For the Longyearbyen data the linear regression is  $T=220+0.468 \cdot MW$ , where  $T$  is the temperature and  $MW$  is the meridional wind. The slope is thus  $0.468 \text{ K/ms}^{-1}$ . The same calculations for zonal winds gave a correlation coefficient of only 0.25 and a probability for random occurrence of 0.066. *Espy et al.* [2003] found a correlation of 0.29 between zonal wind and rotation temperatures at Rothera, so these numbers are also comparable. We believe the correlation is real despite the relatively high probability for random

occurrence, because a westward flow combined with gravity wave drag is expected to produce an equatorward component, and vice versa [Holton, 1983].

We also calculated the correlation between the meridional wind at different heights and the temperature and altitude of the OH layer measured by SABER for the 44 days the two coincided between October 25 and February 11. If the poleward meridional wind is a major driver of downward transport and hence adiabatic heating as our data indicate, we can also expect it to have a role in bringing more oxygen rich air to lower altitudes and thus lowering the OH peak altitude. Table 1 shows the correlation coefficients R between the meridional wind at different heights and OH(6-2) temperature, SABER OH temperature and SABER OH peak altitude.

**Table 1.** Correlation coefficients R and probabilities for random occurrence p for the linear relationship between meridional wind at different heights and OH(6-2) temperature, SABER OH temperature and SABER OH peak altitudes.

Altitude (km)	MW vs OH(6-2) T		MW vs SABER T		MW vs SABER OH Alt	
	R	p	R	p	R	p
70-72	0.63*	5.7E-7	0.59**	3.1E-5	-0.66**	1.2E-6
72-74	0.62	4.7E-7	0.72	2.9E-8	-0.80	1.5E-10
74-76	0.67	3.0E-8	0.76	2.9E-9	-0.81	3.9E-11
76-78	0.68	1.2E-8	0.78	6.5E-10	-0.82	1.6E-11
78-80	0.69	4.2E-9	0.76	2.0E-9	-0.81	2.8E-11
80-82	0.68	8.1E-9	0.75	5.4E-9	-0.78	5.3E-10
82-84	0.70	3.4E-9	0.74	1.1E-8	-0.73	2.2E-8
84-86	0.70	2.0E-9	0.72	4.4E-9	-0.68	3.6E-7
86-88	0.66	5.2E-8	0.67	7.6E-7	-0.62	7.6E-6
88-90	0.56	1.1E-5	0.56	7.6E-5	-0.51	3.6E-4
90-92	0.45	4.8E-4	0.48	1.1E-3	-0.41	5.1E-3
92-94	0.26	5.4E-2	0.35	1.8E-2	-0.29	6.1E-2
94-96	0.040	7.7E-1	0.30	5.1E-2	-0.24	1.2E-1

MW = Meridional wind; T = Temperature; OH Alt = OH peak altitude

\* 52 coincident days

\*\* 43 coincident days

The corresponding probabilities for random occurrence,  $p$ , are also listed. It is interesting to see that the maximum correlation with the SABER measurements was found for winds at 76-78 km height, not higher up as for OH(6-2) temperatures. Figure 4 shows the meridional wind at 76-78 km height plotted against OH layer peak altitude, and the linear fit to the data points. The correlation coefficient is -0.82 with probability for random occurrence  $<10^{-11}$ . This means that more than 67% of the variation in OH layer height can be explained by the meridional wind fluctuations. A  $10 \text{ ms}^{-1}$  increase of meridional wind strength in the poleward direction corresponds to a decrease of OH peak altitude of  $\sim 1.3 \text{ km}$ , according to our data and the linear relationship found. The quantity of data is clearly not sufficient to treat this as a general rule, but it is indicative of the relation between the two parameters.

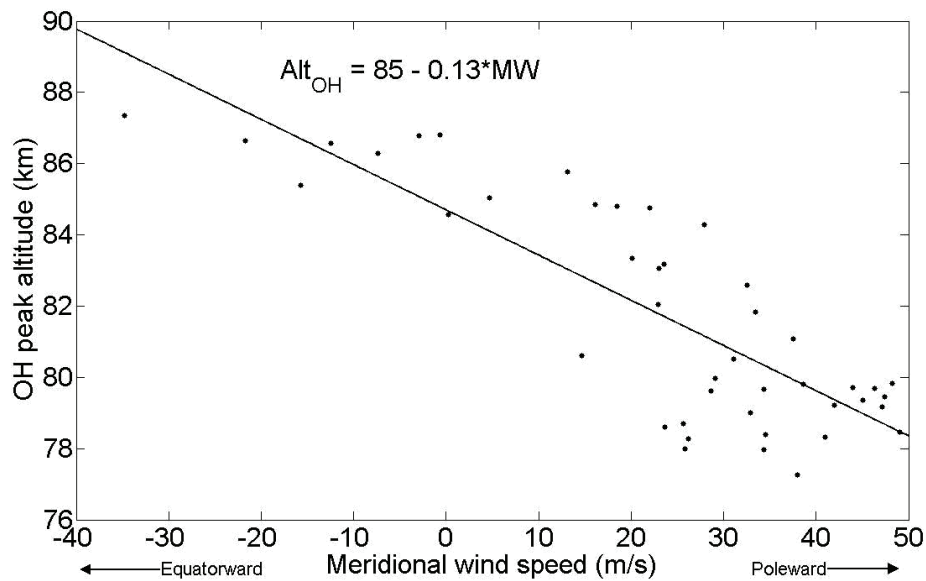


**Figure 4.** Scatter diagram of the 44 coinciding OH peak altitudes measured by SABER and meridional wind measurements from Longyearbyen between 25 October 2003 and 11 February 2004. The solid line shows the best linear fit to the data points.  $\text{Alt}_{\text{OH}}$  denotes the peak altitude of the OH layer and MW the value for the meridional wind. The correlation coefficient is -0.82, with the probability for random occurrence  $<10^{-11}$ .

The meteor radar, spectrometer and satellite data make three completely independent measurements and having them probe the same region, gives new possibilities for interpreting the different data sets. The strength of the meridional winds is obviously an important key in the OH airglow budget. Not only by transporting atomic oxygen from their source region to the high-latitude regions, but also by its close connection with downwelling of atomic oxygen (decreasing the OH layer peak height) and by inducing adiabatic heating/cooling of the neutral air.

Our data support the theory that there is a coupling between the strong polar vortex observed at the upper stratosphere during period 3 and the anomalously high OH temperature and low OH layer peak altitude. *Siskind et al.* [2007] have provided a potential explanation for the mechanism responsible for bringing atomic oxygen rich air to unusually low altitudes and *Winick et al.* [2009] discussed it in the context of their SABER measurements of v1.06 OH temperatures, altitudes and peak VER. A strong stratospheric vortex confines air to the polar region, and leads to unmixed descent of oxygen rich air to lower altitudes. At the same time, the disturbed warm lower stratosphere blocks propagation of gravity waves which normally break near the stratopause and warms this region. The temperature profiles for January and February 2004 in Figure 2 show that this was a likely state for the atmosphere above Longyearbyen. The ~50 km region for January and February 2004 was cold, while the stratopause is as high as 75-80 km. A recent model study by *Karlsson et al.* [2009] also attribute high temperatures at 80 km to enhanced downwelling that results from the negative gravity wave drag (GWD) associated with weak planetary wave activity in the lower atmosphere. They also suggest inter-hemispheric coupling mechanisms between temperature and wind fields. That coupling would be interesting to investigate combining our data sets with those at other latitudes and longitudes.

## 5. Summary

For the Arctic winter of 2003-2004, we have assembled a detailed picture of the behavior of OH temperatures and peak altitudes from a combination of ground-based and satellite data. The SABER temperatures and OH(6-2) rotational temperatures display very similar relative variations. A positive bias of  $14 \pm 9$  K is found in favor of SABER when compared to rotational temperatures, which is

opposite to the sign found at lower latitudes. A detailed examination of the reasons for this temperature difference will be the subject of a future study.

By studying the temperature and wind record from 2003-2004, we have identified the signatures of the SSW at the mesopause region above Longyearbyen. The reversal of the zonal wind happened around 24 December 2003, around ten days earlier than the reversal in the stratosphere. The eastward wind was re-established after 13 January 2004 and around the same time that the temperature increases dramatically and remained high until late February. In the same period the OH layer peak altitude was anomalously low. Studies of the correlation between meridional wind at different heights and OH temperatures and altitudes, reveal a close relationship. About 50% of the variation of the OH(6-2) temperature can be assigned to variations in meridional wind direction and strength. For the SABER OH temperatures and peak altitudes there is also a clear relationship. Variations in the peak altitude of the OH layer can be attributed to variations in the meridional wind. An increase in the poleward/equatorward wind of  $10 \text{ ms}^{-1}$  corresponds to a  $\sim 1.3 \text{ km}$  lowering/rise of the OH layer.

The data support the theory that vertical transport is the mechanism responsible for much of the modulation in OH layer emission and thus the temperature variations observed. This transport was enhanced during the unique stratospheric conditions during the 2003-2004 winter, when an unusually strong upper stratospheric vortex led to increased descent of atomic oxygen which has a key role in OH chemistry. Of the observed temperature increase of  $\sim 50 \text{ K}$  during the 2003-2004 winter, the reformation of the OH layer at approximately 10 km below its nominal altitude of 87 km accounted for a temperature increase of  $\sim 15 \text{ K}$ . The remainder (20-35 K) was due to adiabatic heating resulting from the increased downwelling coupled to the strong meridional winds observed and other non-identified processes.

Our study confirms the importance of having information about the OH layer altitudes at hand when analyzing rotational temperature time series obtained from ground-based or satellite instruments. The satellite data have been invaluable in this sense, as they provide an independent measurement of the OH layer properties. This knowledge also opens up the possibility to use meridional wind direction and strength as a predictor of temperature and OH layer peak heights, but analysis of a much larger data set is needed to explore this possibility.

**Acknowledgments.** We are grateful to the entire NASA TIMED/SABER team for making the SABER data freely available.

## References

- Andrews, D. G., J. R. Holton, and C. B. Leovy (1987), Middle atmosphere dynamics, *Academic Press, New York*, 489pp.
- Aso, T., T. Tsuda and S. Kato (1979), Meteor radar observations at Kyoto University, *J. Atmos. Terr. Phys.*, *41*, 517-525.
- Beig et al. (2003) Review of mesospheric temperature trends, *Rev. Geophys.*, *41*(4), 1015, doi:10.1029/2002RG000121.
- Cho, Y.-M., and G. G. Shepherd (2006), Correlation of airglow temperature and emission rate at Resolute Bay (74.68°N), over four winters (2001-2005), *Geophys. Res. Lett.*, *33*, L06815, doi: 10.1029/2005GL025298.
- Cosby, P. C., and T. G. Slanger (2007), OH spectroscopy and chemistry investigated with astronomical sky spectra, *Can. J. Phys.*, *85*, 77-99, doi: 10.1139/P06-088.
- Dyrland, M. E., and F. Sigernes (2007), An update on the hydroxyl airglow temperature record from the Auroral Station in Adventdalen, Svalbard (1980-2005), *Can. J. Phys.*, *85*(2), 143-151, doi:10.1139/P07-040.
- Espy, P. J., R. E. Hibbins, G. O. L. Jones, D. M. Riggins, and D. C. Fritts (2003), Rapid, large-scale temperature changes in the polar mesosphere and their relationship to meridional flows, *Geophys. Res. Lett.*, *30*(5), 1240, doi: 10.1029/2002GL016452.
- French, W. J. R., G. B. Burns, K. Finlayson, P. A. Greet, R. P. Lowe, and P. F. B. Williams (2000), Hydroxyl (6-2) airglow emission intensity ratios for rotational temperature determination, *Ann. Geophys.*, *18*, 1293-1303.
- Hall, C.M., T. Aso and M. Tsutsumi (2002), An examination of high latitude upper mesosphere dynamic stability using the Nippon /Norway Svalbard Meteor Radar, *Geophys. Res. Lett.*, *29*, 1211-1213.

- Hocking, W.K., Fuller, B., and B. Vandeppeer (2001), Real-time determination of meteor-related parameters utilizing modern digital technology, *J. Atmos. Sol. Terr. Phys.*, *63*, 155-169.
- Hoffmann, P., W. Singer, D. Keuer, W. K. Hocking, M. Kunze, and Y. Murayama, Latitudinal and longitudinal variability of mesospheric winds and temperatures during stratospheric warming events (2007), *J. Atmos. Sol. Terr. Phys.*, *69*, 2355-2366.
- Holdsworth, D.A., I.M. Reid and M.A. Cervera (2004), Buckland Park all-sky interferometric meteor radar, *Radio Sci.*, *39*, RS5009, doi:10.1029/2003RS003014.
- Holton, J. R.. (1983), The influence of gravity wave breaking on the general circulation of the middle atmosphere, *J. Atmos. Sci.*, *40*, 2497-2507.
- Karlsson, B., C. McLandress, and T. G. Shepherd (2009), Inter-Hemispheric mesospheric coupling in a comprehensive middle atmosphere model, *J. Atmos. Sol. Terr. Phys.*, *71*, 518-530.
- Kumar, K. K., C. Vineeth, T. M. Antonita, T. K. Pant, and R. Sridharan (2008), Determination of day-time OH emission heights using simultaneous meteor radar, day-glow photometer and TIMED/SABER observations over Thumba (8.5°N, 77°E), *Geophys. Res. Lett.*, *35*, L18809, doi: 10.1029/2008GL035376.
- Langhoff, S. R., H-J. Werner, and P. Rosmus (1986), Theoretical transition probabilities for the OH Meinel system, *J. Molec. Spectrosc.*, *118*, 507-529.
- López-Gonzalez, M. J., M. García-Comas, E. Rodriguez, M. López-Puertas, M. G. Shepherd, G. G. Shepherd, S. Sargoytchev, V. M. Aushev, S., M. Smith, M. G. Mlynczak, J. M. Russel, S. Brown, Y.-M. Cho, and R. H. Wiens (2007), Ground-based mesospheric temperatures at mid-latitude derived from O2 and OH airglow SATI data: Comparison with SABER measurements, *J. Atmos. Sol. Terr. Phys.*, *69*, 2379-2390.
- Liu, G., and G. G. Shepherd (2006), An empirical model for the altitude of the OH nightglow emission, *Geophys. Res. Lett.*, *33*, L09805, doi: 10.1029/2005GL025297.

- Manney, G. L., K. Krüger, J. L. Sabutis, S. A. Sena, and S. Pawson (2005), The remarkable 2003-2004 winter and other recent warm winters in the Arctic stratosphere since the late 1990s, *J. Geophys. Res.*, *110*, D04107, doi:10.29/2004JD005367.
- Marsh, D. R., A. K. Smith, M. G. Mlynczak, and J. M. Russell III (2006), SABER observations of the OH Meinel airglow variability near the mesopause, *J. Geophys. Res.*, *111*, A10S05, doi: 10.1029/2005JA011451.
- Mertens, C. J., F. J. Schmidlin, R. A. Goldberg, E. E. Remsberg, W. D. Pesnell, J. M. Russell, M. G. Mlynczak, M. López-Puertas, P. P. Wintersteiner, R. H. Picard, J. R. Winick, and L. L. Gordley (2004), SABER observations of mesospheric temperatures and comparisons with falling sphere measurements taken during the 2002 summer MacWAVE campaign, *Geophys. Res. Lett.*, *31*, L03105, doi: 10.1029/2003GL018605.
- Mukhtarov, P., D. Pancheva, B. Andonov, N. J. Mitchell, E. Merzlyakov, W. Singer, W. Hocking, C. Meek, A. Manson, and Y. Murayama (2007), Large-scale thermodynamics of the stratosphere and mesosphere during the major stratospheric warming in 2003/2004, *J. Atmos. Sol. Terr. Phys.*, *69*, 2338-2354.
- Mulligan, F. J. and R. P. Lowe (2008), OH-equivalent temperatures derived from ACE-FTS and SABER temperature profiles - a comparison with OH\*(3-1) temperatures from Maynooth (53.2N, 6.4W), *Ann. Geophys.*, *26*, 795-811.
- Myrabø, H. K., and C. S. Deehr (1984), Mid-winter hydroxyl night airglow emission intensities in the Northern polar region, *Planet. Space Sci.*, *32* (3), 263-271.
- Shepherd, G. G., Y-M. Cho, G. Liu, M. G. Shepherd, and R. G. Roble (2006), Airglow variability in the context of the global mesospheric circulation, *J. Atmos. Sol. Terr. Phys.*, *68*, 2000-2011, doi: 10.1016/j.jastp.2006.06.006
- Shepherd, M. G., D. L. Wu, I. N. Fedulina, S. Gurubaran, J. M. Russell, M. G. Mlynczak, and G. G. Shepherd (2007), Stratospheric warming effects on the tropical mesospheric temperature field, *J. Atmos. Sol. Terr. Phys.*, *69*, 2309-2337, doi: 10.1016/j.jastp.2007.04.009.

- Sherman, J. P., and C-Y. She (2006), Seasonal variation of mesopause region wind shears, convective and dynamic instabilities above Fort Collins, CO: A statistical study, *J. Atmos. Sol. Terr. Phys.*, *68*, 1061-1074.
- Sigernes, F., N. Shumilov, C. S. Deehr, K. P. Nielsen, T. Svenøe, and O. Havnes (2003), The Hydroxyl rotational temperature record from the Auroral Station in Adventdalen, Svalbard (78°N, 15°E), *J. Geophys. Res.*, *108*, 1342, doi: 10.1039/2001JA009023.
- Siskind, D. E., L. Coy, and P. Espy (2005), Observations of stratospheric warmings and mesospheric coolings by the TIMED SABER instrument, *Geophys. Res. Lett.*, *32*, doi: 10.1029/2005GL022399.
- Siskind, D. E., S. D. Eckermann, L. Coy, J. P. McCormack, and C. E. Randall (2007), On recent interannual variability of the Arctic winter mesosphere: Implications for tracer descent, *Geophys. Res. Lett.*, *34*, L09806, doi: 10.1029/2007GL029293.
- Sivjee, G. G., and R. M. Hamwey (1987), Temperature and chemistry of the polar mesopause OH, *J. Geophys. Res.*, *92*(A5), 4663-4672.
- Schoeberl, M. R. (1978), Stratospheric warmings: Observations and theory, *Rev. Geophys Space Phys.*, *16*, 521-538.
- Tsutsumi, M., D. Holdsworth, T. Nakamura and I. Reid (1999), Meteor observations with an MF radar, *Earth, Planets Space*, *51*, 691-699.
- Yee, J. H., G. Crowley, R. G. Roble, W. R. Skinner, M. D. Burrage, and P. B. Hays (1997), Global simulations and observations of O(1S), O<sub>2</sub>(1Σ) and OH mesospheric nightglow emissions. *J. Geophys. Res.*, *102*(A9) 19949-19968.
- Walterscheid, R. L., G. G. Sivjee, and R. G. Roble (2000), Mesospheric and lower thermospheric manifestations of a stratospheric warming event over Eureka, Canada (80°N), *Geophys. Res. Lett.*, *27*, 2897-2900.
- Winick, J. R., P. P. Wintersteiner, R. H. Picard, D. Esplin, M. G. Mlynczak, J. M. Russell III, and L. L. Gordley (2009), OH layer characteristics during unusual boreal winters of 2004 and 2006, *J. Geophys. Res.*, *114*, A02303, doi: 10.1029/2008JA013688.



## **Paper 3**

### **Inferring hydroxyl layer peak heights from ground-based measurements of OH(6-2) band radiance at Longyearbyen (78°N, 16°E)**

Mulligan, F. J., M. E. Dyrland, F. Sigernes, and C. S. Deehr (2009)

**Submitted to: *Annales Geophysicae***

Manuscript # angeo-2009-119

(Revised version published, *Ann. Geophys.*, 27, 4197-4205, 2009.

© 2009 Authors)



# Inferring hydroxyl layer peak heights from ground-based measurements of OH(6-2) band radiance at Longyearbyen (78°N, 16°E)

F. J. Mulligan<sup>1</sup>, M. E. Dyrland<sup>2</sup>, F. Sigernes<sup>2</sup>, C. S. Deehr<sup>3</sup>

<sup>1</sup>National University of Ireland Maynooth

<sup>2</sup>The University Centre in Svalbard, Norway

<sup>3</sup>University of Alaska Fairbanks, USA

Corresponding author: frank.mulligan@nuim.ie

**Abstract.** Measurements of hydroxyl nightglow emissions over Longyearbyen (78°N, 16°E) recorded simultaneously by the SABER instrument onboard the TIMED satellite and a ground-based Ebert-Fastie spectrometer have been used to derive an empirical formula for the height of the OH layer as a function of the brightness of the emission. Altitude profiles of the OH volume emission rate measured by SABER over a period of more than six years provided a relation between the height of the OH layer peak and the integrated volume emission rate following the procedure described by *Liu and Shepherd* [2006]. An extended period of overlap of SABER and ground-based spectrometer measurements of OH(6-2) band radiance during the 2003-2004 winter season allowed us to express radiance values in terms of the satellite integrated VER measurements. The combination of these two formulae provided a method for inferring an altitude of the OH emission layer over Longyearbyen from ground-based measurements alone. Such a method is required when SABER is in a southward looking yaw cycle. In the SABER data for the period 2002-2008, the peak altitude of the OH layer ranged from a minimum near 76 km to a maximum near 90 km. The uncertainty in the inferred altitude of the peak emission, which includes a contribution for atmospheric extinction, was estimated to be  $\pm 2.7$  km and is comparable with the  $\pm 2.6$  km value quoted for the nominal altitude (87 km) of the OH layer. Longer periods of overlap of satellite and ground-based measurements together with simultaneous on-site measurements of atmospheric extinction could reduce the uncertainty to approximately 2 km.

## 1. Introduction

An Ebert-Fastie spectrometer has been used to record spectra of hydroxyl nightglow emissions (OH(6-2) and OH(8-3) bands) at Longyearbyen (78°N, 16°E) in each winter season for more than 20 years. Analysis of these spectra has provided a detailed record of the rotational temperature at the altitude from which the emissions originate [e.g., *Sivjee and Hamwey*, 1987; *Sivjee et al.*, 1987; *Sigernes et al.*, 2003; *Dyrland and Sigernes*, 2007]. These measurements have always been subject to the twin difficulties of an inexact knowledge of the emission height and the dependence of the retrieved temperature on the rotational transition probabilities used. The work reported here concentrates on the question of the emission height only. Following the work of *Baker and Stair* [1988], the OH layer has been considered to be representative of an ~8 km layer centred at 87 km altitude. Subsequent reports by *She and Lowe* [1998] and *Oberheide et al.* [2006] have confirmed that this interpretation is an accurate assessment of the time averaged height and width of the layer. A more detailed study by *Yee et al.* [1997] using HRDI (High Resolution Doppler Imager) results from UARS (Upper Atmosphere Research Satellite) showed that the peak altitude of the night time OH emissions could occur anywhere in the range 86 – 91 km. HRDI observations showed an inverse relationship between the nightglow brightness and peak emission altitude. *Liu and Shepherd* [2006] using OH volume emission rate (VER) data from the WINDII (Wind Imaging Interferometer) instrument on board the UARS satellite reaffirmed the inverse relationship and reported systematic variations in the peak altitude of the OH layer between 40°S and 40°N. High latitude observations were precluded by the inclination of the UARS spacecraft orbit. Using data from the SABER (Sounding of the Atmosphere by Broadband Emission Radiometry) instrument on the TIMED (Thermosphere Ionosphere Mesosphere Energetics and Dynamics) satellite, *Winick et al.* [2009] found that in the region poleward of 60°N, the OH layer was between 5 km and 8 km lower than normal during the boreal winters of 2004 and 2006. Changes in altitude of this magnitude together with the associated adiabatic heating/cooling will result in substantial temperature variations, the interpretation of which is eased considerably if OH emission height information is available. *Takahashi et al.* [2005] have called for

further investigations of the relation of temporal variation between hydroxyl emission rates, height and temperatures.

Knowledge of the OH emission height is also important because of the role of OH temperature measurements in the assignment of temperatures derived from meteor radars in the MLT region. Meteor radar temperatures offer the possibility of 24 hour per day measurements and in all sky conditions [*Hocking et al.*, 2007]. *Hall et al.* [2004] extrapolated the OH temperatures from 87 km to 90 km for the purpose of a multi-instrument derivation of 90 km temperatures over Svalbard based on the CIRA-86 and MSISE-90 models. A similar extrapolation technique based on MSIS-00 was employed by the same authors in 2006 [*Hall et al.*, 2006]. The validity of their meteor derived temperatures depends on the assumption that the OH layer is centred on 87 km altitude. Interpretation of rotational temperatures derived from OH emissions must, therefore, take account of the altitude of the emitting layer.

A number of recent reports have sought to infer the altitude of the peak of OH emission by combining results from different ground-based instruments. Employing a pair of all-sky imagers at sites 32 km apart, *Kubota et al.* [1999] observed common features in nightglow structure and found that the inverse relationship between brightness and altitude persisted on a local scale. *Takahashi et al.* [2005] reported OH emission heights deduced from cross correlating rotational temperatures from the OH(6-2) band and meteor trail ambipolar diffusion coefficients at Shigaraki (35°N, 136°E). *Kumar et al.* [2008] employed a similar technique to infer day-time emission heights over Thumba (8.5°N, 77°E) which corresponded well with peak heights observed in SABER OH VER profiles in the same time period. *Liu and Shepherd* [2006] found that, in the latitude range 40°S to 40°N, the altitude of the peak of the OH layer is almost completely described by the integrated emission rates in their study of WINDII profiles from the UARS satellite. Ground-based instruments that collect photons from all altitudes in the OH layer within their field of view are well suited for measuring integrated emission rates and offer the possibility to assign an altitude to each ground-based measurement. Of course ground-based integrated brightness (radiance) measurements are subject to the effects of atmospheric extinction, which do not apply in the case of satellite observations. At 78°N, Longyearbyen is outside the range of latitude covered by the study of *Liu and Shepherd* [2006] and of the

WINDII measurements. The SABER instrument measures OH VER profiles in the range 1.56-1.72  $\mu\text{m}$ , which includes mostly the OH(4-2) and (5-3) band, and provides excellent coverage at 78°N during northward looking yaw cycles. Unfortunately, SABER is in its southward looking phase during a large part of the Arctic winter season (mid-November – mid-January) when its latitude coverage does not extend above 54° N.

A remarkable period of good observing conditions during the spring of 2004 provided 35 days (16 January – 19 February) of measurements of OH emissions by the ground-based Ebert-Fastie spectrometer at Longyearbyen during a time when the SABER instrument was in a northward looking yaw cycle. This allowed us to derive a relation between integrated OH VER measured by the satellite and the OH(6-2) band radiance measured by the spectrometer. The remainder of this paper reports our efforts to adapt the procedure described by *Liu and Shepherd* [2006] to SABER OH VER profiles and to relate the empirical formula thus obtained to the OH(6-2) band radiance measured by the Ebert-Fastie spectrometer deployed at Longyearbyen for the purpose of inferring hydroxyl layer heights during periods when SABER is in a southward looking yaw cycle.

## **2. Data and analysis**

### **2.1 SABER on TIMED**

*Liu and Shepherd* [2006] made use of more than 50,000 altitude profiles of volume emission rate (VER) collected by WINDII for the OH(8-3) band  $P_1(3)$  line emission to derive an empirical formula for the altitude of the OH nightglow emission. The results were formulated in terms of zonal averages covering the latitude range 40°S to 40°N. The work reported here makes use of altitude profiles measured by the SABER instrument on board NASA's TIMED satellite. SABER measures vertical Earth limb emission profiles in 10 broadband spectral channels covering the wavelength range 1.27  $\mu\text{m}$  to 17  $\mu\text{m}$  [*Mertens et al.*, 2004]. The high inclination angle of TIMED's orbit (74 degrees to the equator) allows it to observe tangent points as far north as Longyearbyen, when it is in a northward looking yaw cycle. The TIMED satellite orbits the Earth about 15 times per day, and measures about 100 vertical profiles in each orbit. SABER has a vertical resolution of approximately 2 km in the altitude range 10-105 km,

and an along track resolution of near 400 km. OH VER profiles (data version 1.07) measured by SABER's OH-B band channel in the range 1.56-1.72  $\mu\text{m}$  which includes mostly the OH(4-2) and OH(5-3) bands were employed in this study. *Baker et al.* [2007] made use of this channel in their study of equatorial enhancements of the nighttime mesospheric OH airglow layer. We have chosen this channel in preference to the OH-A channel, which includes mostly the  $\Delta v = 2$  bands originating in levels 9 and 8, because the higher vibrational bands tend to have their maxima at higher altitude [*Kaufmann et al.*, 2008]. Since the focus of our study was on ground-based measurements made at Longyearbyen, and since longitudinal variations were not ruled out in the investigation by *Liu and Shepherd* [2006], we restricted ourselves to orbits that satisfied the selection criteria – latitude:  $78 \pm 5^\circ \text{N}$ ; longitude:  $16 \pm 10^\circ \text{E}$  – corresponding to a radius of about 600 km centred on the station. Following the work of *Winick et al.* [2009], we also restricted ourselves to night time profiles only for which the solar zenith angle was greater than  $105^\circ$ . Typically this resulted in five or six profiles per day during a northward looking yaw cycle, and over the period January 2002 – July 2008, provided more than 3100 profiles in total.

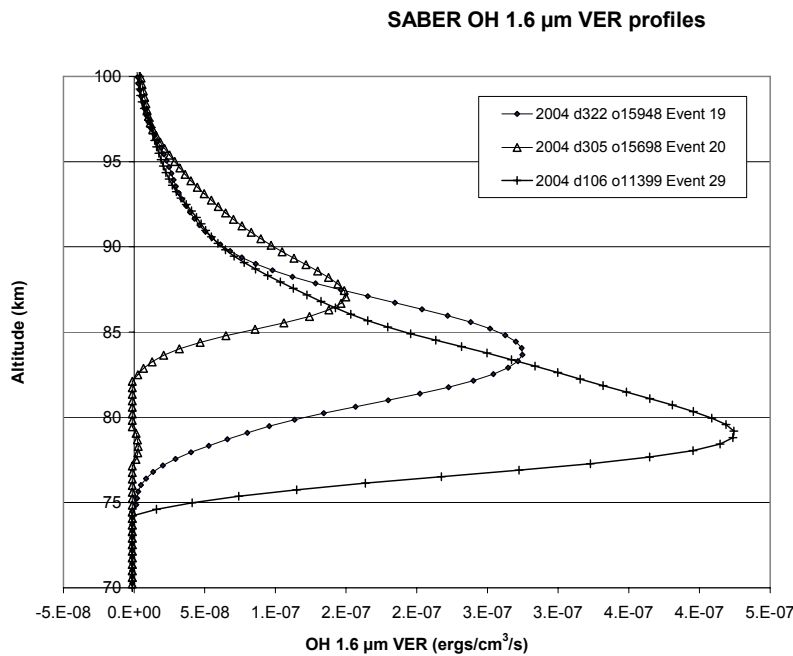


**Figure 1.** SABER OH 1.6  $\mu\text{m}$  VER profiles representative of Longyearbyen ( $78 \pm 5^\circ \text{N}$ ,  $16 \pm 10^\circ \text{E}$ ) in the period 2002-2008.

Figure 1 shows three OH 1.6  $\mu\text{m}$  VER profiles which are representative of the SABER profiles over Longyearbyen during the period 2002-2008, and it illustrates the relationship between the altitude of the OH layer peak and the brightness of the layer observed by *Liu and Shepherd* for WINDII profiles.

Following the method of *Liu and Shepherd* [2006], the peak altitude of the Gaussian that best fitted the peak of the measured profile was taken as the altitude of the OH layer peak and the corresponding integrated emission rate was obtained by computing the integral of the area under the VER profile. Figure 2 is a scatter plot of the peak altitude of each profile versus the integrated volume emission rate. The inverse relationship between the OH layer peak altitude and the integrated emission rate is immediately apparent. Through the use of multiple linear regression, we examined the influence of the various terms included in the empirical formula reported by *Liu and Shepherd*, i.e., integrated emission rate,  $I_s$  (the subscript 's' refers to the satellite to distinguish it from band radiance measurements made from the ground  $I_g$ ) in  $\text{ergs}/\text{cm}^2/\text{s}$ , 10.7 cm solar flux,  $f$ , annual and semi annual terms as well as diurnal and semidiurnal terms.

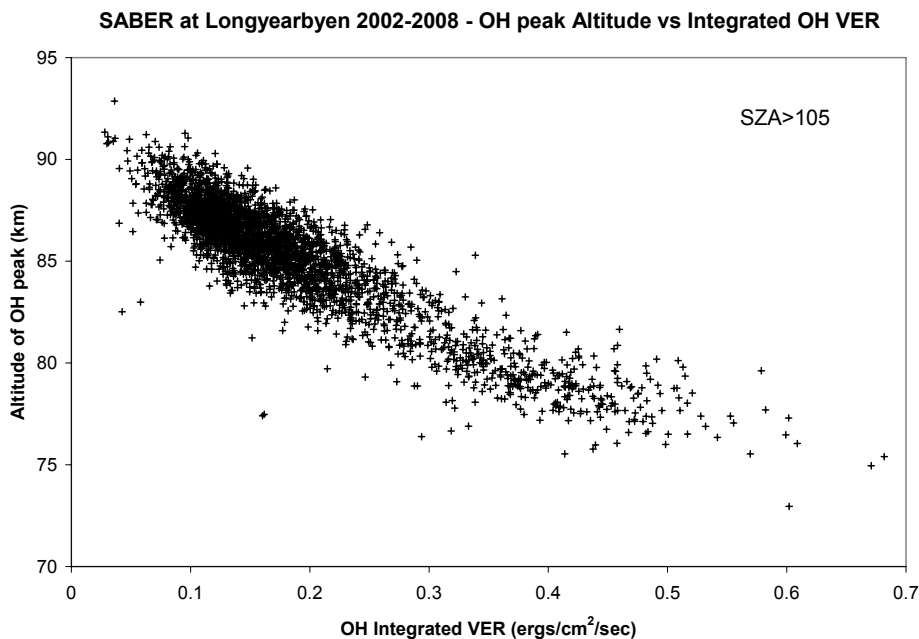


**Figure 2.** Altitude of OH maximum and integrated OH VER for each profile measured by SABER at Longyearbyen ( $78\pm 5^\circ\text{N}$ ,  $16\pm 10^\circ\text{E}$ ) in the period 2002-2008, when the solar zenith angle (SZA)  $> 105^\circ$ .

Retaining the notation employed by *Liu and Shepherd* [2006], the empirical model can be expressed as:

$$\begin{aligned}
 h = h_0 + a_1 I_s + a_2 I_s^2 + a_3 f + a_4 \cos\left(\frac{2\pi d}{T}\right) + a_5 \sin\left(\frac{2\pi d}{T}\right) + a_6 \cos\left(\frac{4\pi d}{T}\right) + a_7 \sin\left(\frac{4\pi d}{T}\right) \\
 + a_8 \cos\left(\frac{2\pi t}{D}\right) + a_9 \sin\left(\frac{2\pi t}{D}\right) + a_{10} \cos\left(\frac{4\pi t}{D}\right) + a_{11} \sin\left(\frac{4\pi t}{D}\right)
 \end{aligned}
 \tag{1}$$

where  $h$  is the peak emission altitude in km,  $h_0$  is a constant term in km,  $d$  is the day number of the year and  $t$  is the time of the observation,  $T$  and  $D$  are the length of the year in days and the length of the day in hours respectively, and the  $a_i$  are the coefficients of the various terms. By far the most significant term in fitting the peak altitude was the integrated intensity,  $I_s$ . Next in importance came the annual and semi-annual terms followed by the solar flux term,  $f$  which has only minor importance since the measurements were made in the middle of the Arctic winter.

Table 1 provides a brief summary of our results. In common with *Liu and Shepherd*, we found that including sinusoidal diurnal and semidiurnal terms made no significant improvement to the fitting of the OH peak altitudes. The fit was improved, however, by including a term in  $I_s^2$  as shown in Table 1. This may be due to the fact that at higher latitudes the OH layer descends by more than one scale height (particularly during the extraordinary spring seasons of 2004 and 2006, when the layer was as low as 75 km on occasions), at which point one might expect some nonlinear response. The rightmost column labelled ‘‘population’’ is a measure of the percentage of predicted altitudes that were within 1.5 km of the actual peak. The values are comparable to the figures reported by *Liu and Shepherd* [2006] for predictions within  $\pm 1$  km of the actual peak.

**Table 1.** Coefficients of the empirical model for the peak altitude of the OH nightglow emission at Longyearbyen.

Coefficients of the empirical model for the peak altitude of the OH nightglow emission at Longyearbyen																
$h_0$ , km	Term $I_s$		Term $I_s^2$		Term $f$		$\cos(2\pi d/T)$		$\sin(2\pi d/T)$		$\cos(4\pi d/T)$		$\sin(4\pi d/T)$		Population <sup>1</sup>	Standard error $\sigma$ (km)
	$a_1$	$\sigma_1$	$a_2$	$\sigma_2$	$a_3$	$\sigma_3$	$a_4$	$\sigma_4$	$a_5$	$\sigma_5$	$a_6$	$\sigma_6$	$a_7$	$\sigma_7$		
90.4	-27.8	0.2	-	-	-	-	-	-	-	-	-	-	-	-	79.9%	1.23
90.1	-27.7	0.2	-	-	0.0029	0.0005	-	-	-	-	-	-	-	-	80.3%	1.22
91.2	-27.7	0.2	-	-	0.0037	0.0004	-2.1	0.5	0.4	0.1	0.0	0.2	0.2	0.1	83.7%	1.14
93.9	-39.7	0.9	23.2	1.6	0.0047	0.0004	-4.6	0.6	0.9	0.1	1.0	0.2	-0.2	0.1	85.0%	1.10

The slight reduction in accuracy may be due to the greater excursions of the OH layer at higher latitudes, and that our analysis included peak altitudes for all profiles in contrast to *Liu and Shepherd* [2006] who excluded profiles that departed from the ideal single peak. We consider that this is a more realistic assessment of the method since a ground-based observer with access only to band radiance data has no way of knowing when a single peaked OH layer is being observed, or when a more complex profile is present. Figure 3 shows a plot of the modelled OH peak altitude versus the measured values using the empirical formula given in the final row of Table 1. The right hand column of this table shows the standard error in the peak altitude for the empirical formula used.

The results of this investigation showed that the methodology of *Liu and Shepherd* [2006] adapted for SABER OH VER profiles observed over Longyearbyen yielded a formula relating the altitude of the OH peak emission to the integrated emission rate. The next step involved finding a relation between the SABER OH integrated intensity and the column integrated emission rate of the OH(6-2) band observed by the spectrometer.

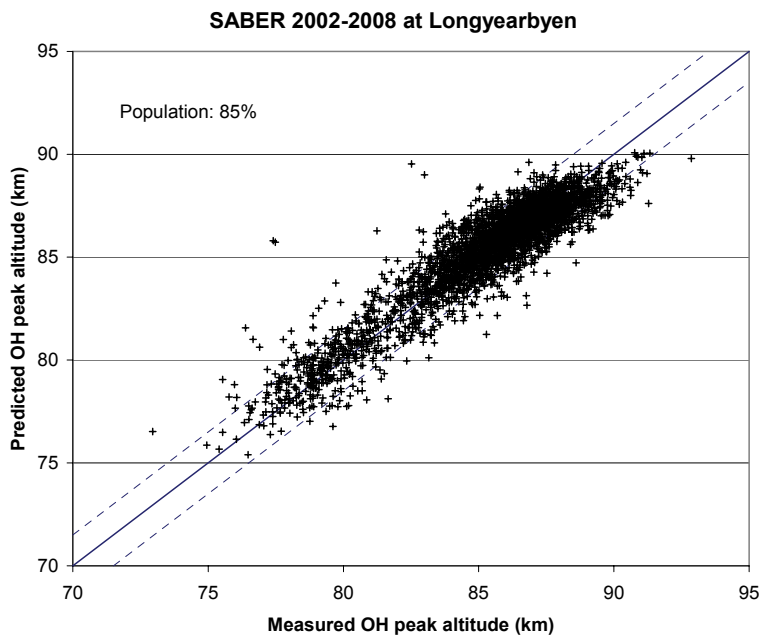


**Figure 3.** Altitude of OH layer peak predicted by empirical formula versus altitude measured by SABER at Longyearbyen ( $78\pm 5^\circ\text{N}$ ,  $16\pm 10^\circ\text{E}$ ) during 2002-2008.

## 2.2 Ebert-Fastie Spectrometer

An Ebert-Fastie spectrometer has been deployed at Longyearbyen (78°N, 16°E) for the purpose of studying hydroxyl nightglow emissions in each winter season for over a quarter century [Dyrland and Sigernes, 2007]. The instrument in use in recent years has a 1 m focal length and a field of view of approximately 5° viewing in the zenith. Spectra recorded by this instrument have been analysed to derive the rotational temperature of the emitting OH radicals at the emission altitude, e.g., Sivjee and Hamwey [1987], Sigernes et al. [2003], Dyrland and Sigernes [2007]. Detailed descriptions of the spectrometer characteristics, calibration and data reduction techniques are available in Sigernes et al. [2003] and Dyrland and Sigernes [2007]. In addition to the rotational temperature, these spectra have also been used to compute the integrated column brightness (radiance) of the emission band, e.g., Myrabø et al. [1983], Myrabø et al. [1987] and Viereck and Deehr [1989].

The analysis of each measured spectrum involves the generation of a synthetic spectrum which has as free fitting parameters (a) the rotational temperature, (b) the background which has both a slope (b1) and an offset (b2), and finally a scaling term (c), which is directly proportional to the radiance of the band,  $I_g$ , (the subscript ‘g’ refers to observations made from the ground) – in this instance the OH(6-2) band. Since the spectrometer measures the total band radiance, it is this latter parameter that we attempt to relate to the integrated volume emission rate measured by SABER. Results for a particular spectrum are accepted only when the covariance between synthetic and measured spectra fall within certain criteria which have been determined with the benefit of experience over many years of observing. Of particular relevance here is the elimination of spectra that are affected to a significant degree by atmospheric extinction. Based on the observations of Myrabø and Deehr [1984], it is unlikely that the selection criteria are capable of eliminating spectra that have less than 20% reduction in band radiance due to atmospheric extinction. In section 4 we consider the impact that such a reduction would have on the OH peak altitude assigned. Instrument calibration takes account of variations in the spectrometer sensitivity across the spectral interval accepted by the spectrometer. Long term stability is monitored by the use of calibration lamp as described in Dyrland and Sigernes [2007].

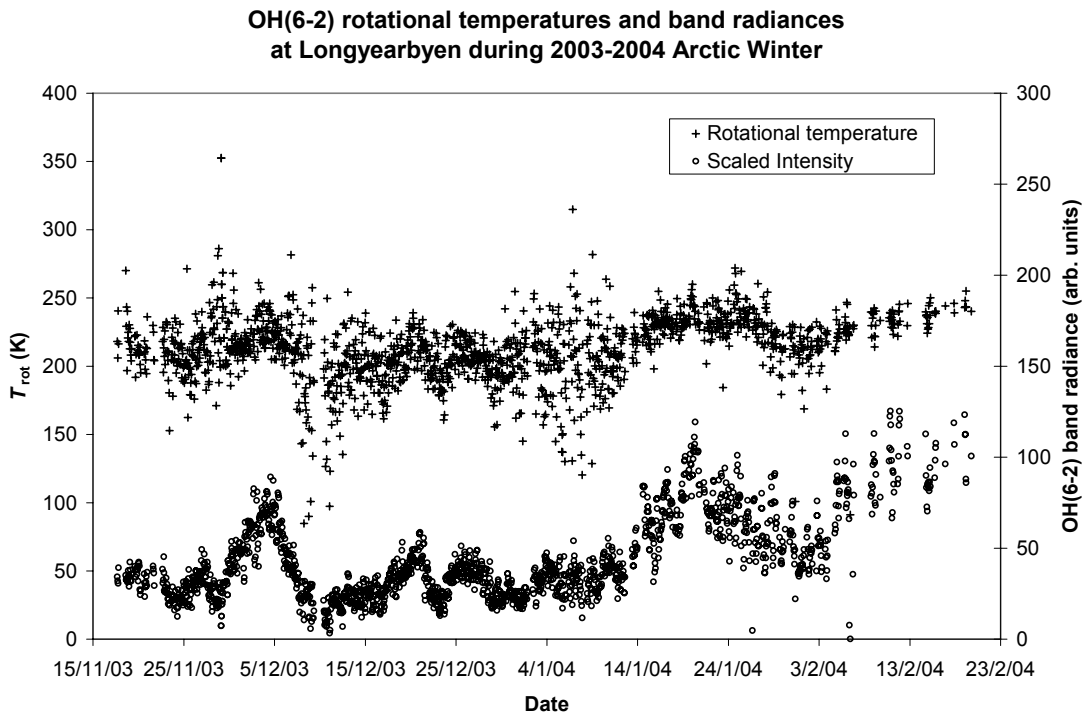


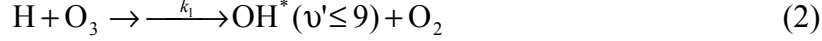
**Figure 4.** OH(6-2) rotational temperatures and band radiances (arb. units) measured by the Ebert-Fastie spectrometer at Longyearbyen during the 2003-2004 Arctic winter season.

In common with the temperature data from the spectrometer, the radiance values are calculated on an hourly average basis. Figure 4 shows a plot of rotational temperature and radiance values obtained from the OH(6-2) band for the 2003-2004 Arctic winter season at Longyearbyen. The *Langhoff et al.* [1986] transition probabilities were selected for generating the synthetic spectra used in this report based on the detailed study of the OH(6-2) band by *French et al.* [2000].

### 2.3 Relating OH(6-2) band intensities to SABER OH integrated VER measurements

The radiance values from the ground-based Ebert-Fastie spectrometer provide a record of the time variation of the total column brightness of the OH(6-2) band, whereas the integrated volume emission rates from SABER provide a similar

record for the sum of the OH(4-2) and (5-3) bands. It is generally accepted that the reaction



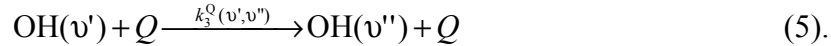
with  $k_1 = 1.4 \times 10^{-10} e^{-480/T} \text{ cm}^3 \text{ s}^{-1}$  is the primary source of vibrationally excited OH. The reaction



is sometimes considered to be a secondary source for vibrational levels ( $\nu' \leq 6$ ), but overall this reaction is believed to be of minor importance during night time conditions [Makhlouf *et al.*, 1995]. Since the OH products of reaction (2) are found in vibrational levels 6, 7, 8 and 9 [Kaufmann *et al.*, 2008], lower vibrational levels are populated as a result of radiative cascade



and single or multi-quantum, collisional deactivation [McDade and Llewellyn, 1987]



OH bands arising from different initial ( $\nu'$ ) and final ( $\nu''$ ) vibrational states have different average band radiances as reported by Krassovsky *et al.* [1962] with updated values for some of these bands by Cosby and Slanger [2007]. However, it is believed that the relative variations of band radiances from adjacent upper states follow each other closely due to the common origin of their primary source. Wrasse *et al.* [2004] show a number of nights with good correspondence between the brightness of the OH(8-3) and (6-2) bands at 23°S. Mulligan *et al.* [1995] found very good agreement between variations in the OH(4-2) and (3-1) bands at 53°N. Based on these observations, we assume that the relative variations in the OH(6-2), (5-3) and (4-2) band radiances follow one another closely. The next step is to establish a relation between the OH(6-2) band radiance measured by the ground-based spectrometer,  $I_g$ , and the integrated volume emission rate for the OH 1.6  $\mu\text{m}$  band,  $I_s$ , measured by SABER.

The yaw cycle for SABER is such that it is looking southward during the middle of the Arctic winter (mid-November to mid-January). Fortunately, a remarkable period of good observing conditions during the spring of 2004 provided 35 days of ground-based OH measurements during a time when SABER was looking northward. Figure 5 is a scatter plot of OH(6-2) band radiance values

versus SABER integrated volume emission rates during the 35 day overlap period (16/1/2004 – 19/2/2004). For the purpose of this plot, a ground-based measurement that occurred within one hour of a satellite measurement was considered coincident with it. Although one hour is a relatively long time window, the close correspondence between the two sets of measurements is clear from the plot. The equation of the best fit line to the data in Figure 5 was used to relate OH(6-2) scaled intensity values,  $I_g$ , to OH integrated VER values,  $I_s$ , measured by SABER. Thus

$$I_s = mI_g \quad (6)$$

where  $m$  is a constant of value  $(4.84 \pm 0.06) \times 10^{-3}$ . The correlation coefficient of 0.84 for the fit indicates the high degree of correspondence between the two data sets.

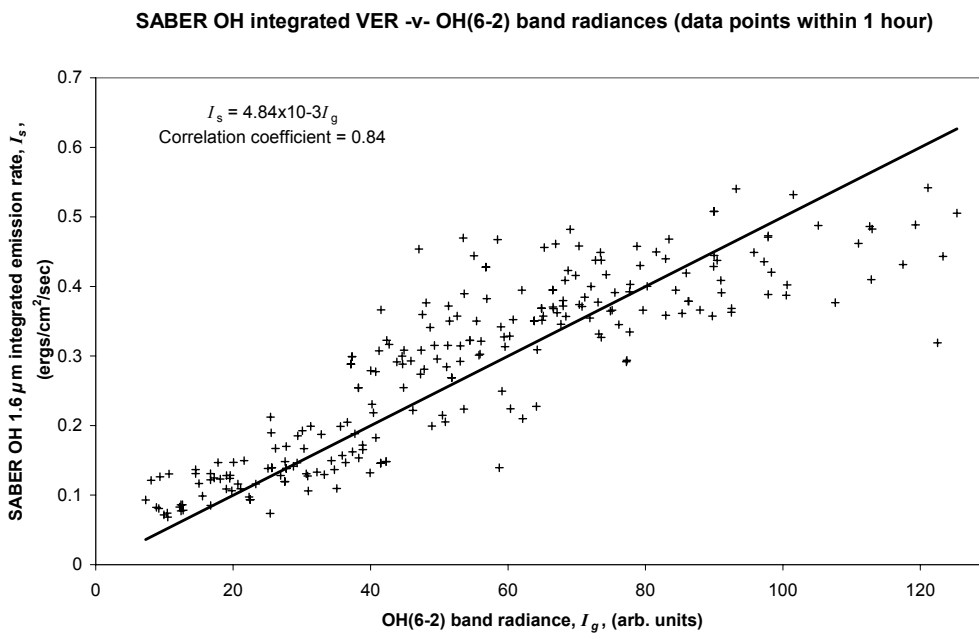


**Figure 5.** Scatter plot of integrated OH VER values measured by SABER at Longyearbyen ( $78 \pm 5^\circ\text{N}$ ,  $16 \pm 10^\circ\text{E}$ ) together with OH(6-2) band radiance (arb. units) measured by the Ebert-Fastie ground-based spectrometer during the period when the two sets of measurements overlap (16/1/2004 – 19/2/2004). The time window for coincidence of the two sets of data is 1 hour. A spectrometer measurement that occurs within 1 hour of a SABER profile is considered coincident in time with that profile.

### OH integrated VER values at Longyearbyen 2003-2004

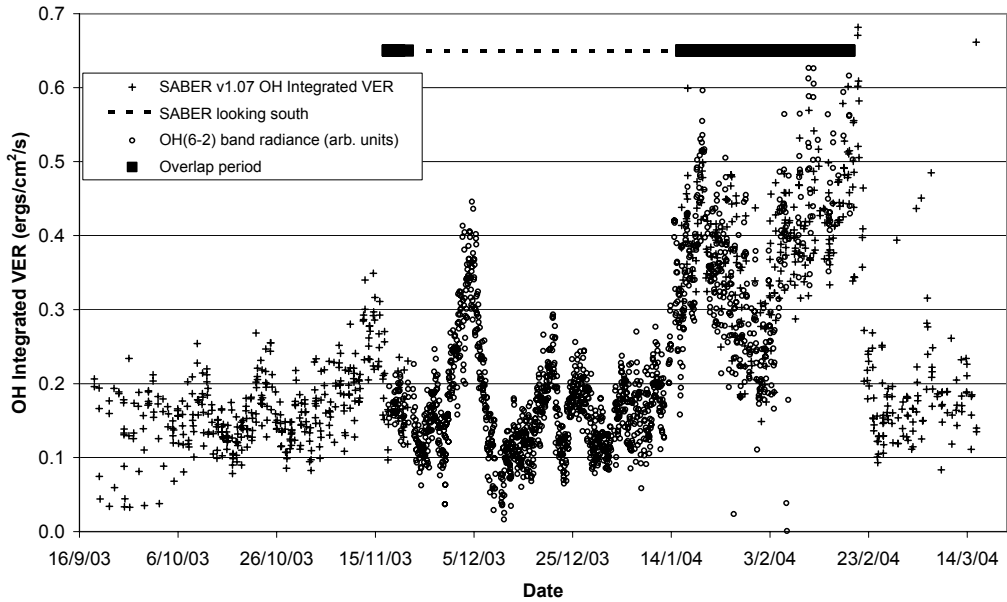


**Figure 6.** Integrated OH VER values calculated from SABER profiles at Longyearbyen ( $78\pm 5^\circ\text{N}$ ,  $16\pm 10^\circ\text{E}$ ) together with OH(6-2) band radiances (arb. units) measured by the Ebert-Fastie during 2003-2004 season. The OH(6-2) band radiance values have been scaled according to the relationship given in equation (6).

Figure 6 shows the result of combining the OH integrated VER measurements,  $I_s$ , with the re-scaled OH(6-2) band radiance measurements,  $mI_g$ . The correspondence between the ground-based and satellite measurements during the overlap period is clearly evident. The standard error in the linear fit obtained from Figure 5 contributed an uncertainty of  $\pm 2.1$  km to the modelled values of peak altitude. We note that the overlap period occurred at a time when SABER OH integrated VER values were among the highest observed during the entire seven year period (see Figure 2). The good agreement between the two data sets in Figure 6 in the period 17-19 November 2003, during a 3-day period of data overlap when OH VER values were near the average value, is very reassuring.

### 3. Results and Discussion

Substituting for  $I_s$  in equation (1) by  $mI_g$ , we predicted the peak altitude of the OH layer from the ground-based OH(6-2) band radiance measurements alone. Figure 7 shows a plot of the OH peak altitude predicted by this technique compared with values of the OH peak altitude measured from SABER OH VER profiles. The correspondence between measured and predicted values during the two overlap periods is excellent. More important however is the fact that we now have values for the altitude of the OH layer peak when no SABER profiles are available.

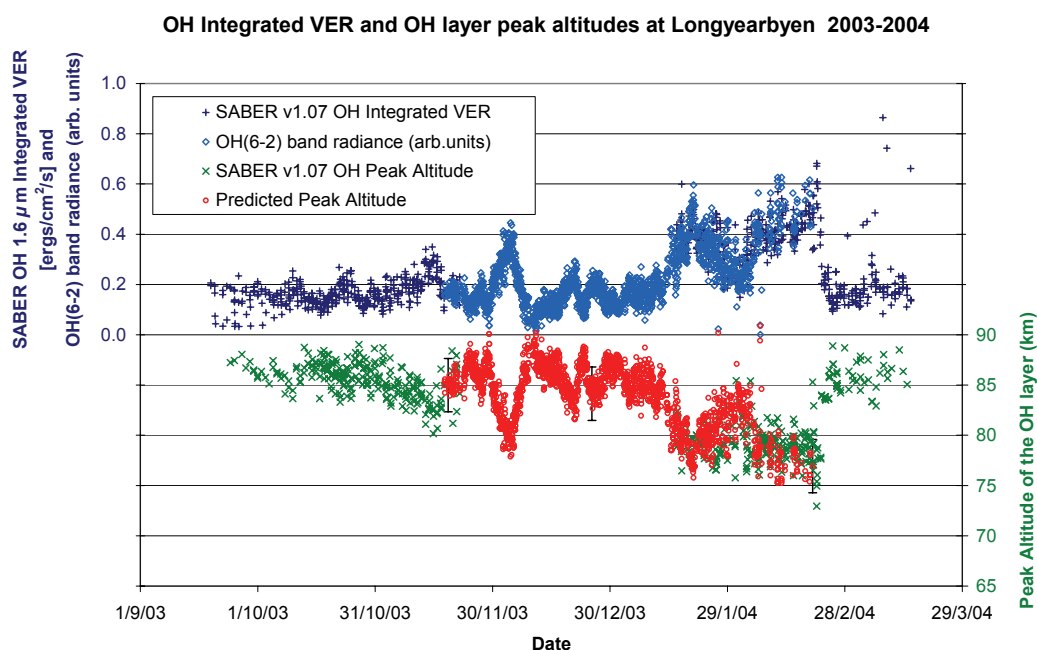


**Figure 7.** OH layer peak height measured by SABER at Longyearbyen ( $78\pm 5^\circ\text{N}$ ,  $16\pm 10^\circ\text{E}$ ) (green) and OH layer peak height predicted by empirical formula for all OH(6-2) data (red) (including the period when SABER was looking south) during the 2003-2004 season. The error bar shown in black indicates the uncertainty ( $\pm 2.7$  km) in the peak altitudes determined. OH integrated VER and OH(6-2) band radiance values (blue) are also shown in this plot to illustrate the inverse relationship between OH brightness and peak altitude.

We now attempt to quantify the uncertainties associated with the inferred altitudes. These arise from the two steps in the empirical procedure described above and from the effect of atmospheric extinction. The standard error on the prediction of the OH peak altitude from the OH integrated VER was  $\pm 1.1$  km, whereas the standard error on the conversion from OH(6-2) band radiances to OH integrated VER was  $\pm 2.1$  km. Based on the observations of Myrabø and Deehr (1984), we estimated a maximum reduction of 20% in the integrated emission brightness due to atmospheric extinction in the lower atmosphere. Such a reduction would give rise to an increase of 1.2 km in the assignment of the OH peak altitude using the combined empirical formula. The uncertainties from the two fitting processes and atmospheric extinction resulted in a combined uncertainty of  $\pm 2.7$  km on each altitude determined. Based on the range of OH peak altitude which extended from 76 km to 90 km in the period 2002-2008, this is a considerable improvement on the nominal 87 km altitude alone. The combined uncertainty is comparable with the  $\pm 2.6$  km figure quoted originally by *Baker and Stair* [1988] for the altitude of the OH layer. We estimate that the uncertainty could be reduced to  $\sim 2$  km with the use of longer periods of overlap of satellite and ground measurements together with simultaneous on-site atmospheric extinction data.

#### **4. Conclusion**

We have successfully implemented the method suggested by *Liu and Shepherd* [2006] for estimating the altitude of the OH nightglow emission altitude for a ground-based station. Substituting WINDII profiles of the OH(8-3) P<sub>1</sub>(3) line by SABER OH 1.6  $\mu\text{m}$  VER profiles, we have extended the range of latitudes available from WINDII to include a station as far north as Longyearbyen (78°N). Results are presented for the 2003-2004 winter season, which provided an opportunity to test the method. Assuming a simple correlation between SABER OH integrated VER measurements and OH(6-2) band radiances, we have demonstrated the peak altitude of the OH layer can be modelled to within an uncertainty of  $\pm 2.7$  km. This is comparable with the  $\pm 2.6$  km uncertainty associated with the nominal altitude of the OH layer. On the basis of the stability of the empirical formula over the seven years of available SABER data, it would

appear that once established at a particular station, the method provides the ground-based observer with a parameter that was previously unavailable.

**Acknowledgements.** We are very appreciative of the high quality of the SABER measurements and we extend our thanks to the entire SABER/TIMED team for making the data freely available. This manuscript was improved considerably as a result of comments on an earlier version by Professor R. P. Lowe of The University of Western Ontario, Canada.

## References

- Baker, D. J., Thurgood, B. K., Harrison, W. K., Mlynczak, M. G., and Russell, J. M. (2007), Equatorial enhancement of the nighttime OH mesospheric infrared airglow, *Phys. Scr.*, *75*, 615-619, doi:10.1088/0031-8949/75/5/004.
- Baker, D. J. and Stair Jr., A. T. (1988), Rocket measurements of the altitude distributions of the hydroxyl airglow, *Physica Scripta*, *37*, 611–622.
- Cosby, P. C., and Slanger, T. G. (2007), OH spectroscopy and chemistry investigated with astronomical sky spectra, *Can. J. Phys.*, *85*, 77-99, doi: 10.1139/P06-088.
- Dyrlund, M. E., and Sigernes, F. (2007), An update on the hydroxyl airglow temperature record from the Auroral Station in Adventdalen, Svalbard (1980-2005), *Can. J. Phys.*, *85*(2), 143-151, doi: 10.1139/P07-040.
- French, W. J. R., Burns, G. B., Finlayson, K., Greet, P. A., Lowe, R. P. and Williams, P. F. B. (2000), Hydroxyl (6-2) airglow emission intensity ratios for rotational temperature determination, *Ann. Geophys.*, *18*, 1293-1303.
- Hall, C. M., Aso, T., Tsutsumi, M., Höffner, J., and Sigernes, F. (2004), Multi-instrument derivation of 90 km temperatures over Svalbard (78°N 16°E), *Radio Sci.*, *39*, RS6001, doi:10.1029/2004RS003069.
- Hall, C. M., Aso, T., Tsutsumi, M., Hoffner, J., Sigernes, F., and Holdsworth, D. A. (2006), Neutral air temperatures at 90 km and 70°N and 78°N, *J. Geophys. Res.*, *111*, D14105, doi:10.1029/2005JD006794.

- Hocking, W. K., Argall, P. S., Lowe, R. P., Sica, R. J. and Ellinor, H. (2007), Height-dependent meteor temperatures and comparisons with lidar and OH measurements, *Can. J. Phys.*, *85*(2), 173-187, doi: 10.1139/P07-038.
- Kaufmann, M. Lehmann, C., Hoffmann, L., Funke, B., López-Puertas, M., von Savigny, C., and Riese, M. (2008), Chemical heating rates derived from SCIAMACHY vibrationally excited OH limb emission spectra, *Adv. Space Res.*, *41*, 1914-1920, doi:10.1016/j.asr.2007.07.045.
- Krassovsky, V. I., Shefov, N. N., and Yarin V. I. (1962), Atlas of the airglow spectrum 3000-12400 Å, *Planet. Space Sci.*, *9*, 883-915.
- Kubota, M., Ishii, M., Shiokawa, K., Ejiri, M. K., and Ogawa, T. (1999), Height measurements of nightglow structures observed by all-sky imagers, *Adv. Space Res.*, *24*, 593-596.
- Kumar, K. K., Vineeth, C., Antonita, T. M., Pant, T. K., and Sridharan, R. (2008), Determination of day-time OH emission heights using simultaneous meteor radar, day-glow photometer and TIMED/SABER observations over Thumba (8.5°N, 77°E), *Geophys. Res. Lett.*, *35*, L18809, doi: 10.1029/2008GL035376.
- Langhoff, S. R., Werner, H-J., and Rosmus, P. (1986), Theoretical transition probabilities for the OH Meinel system, *J. Molec. Spectrosc.*, *118*, 507-529.
- Liu, G., and Shepherd, G. G. (2006), An empirical model for the altitude of the OH nightglow emission, *Geophys. Res. Lett.*, *33*, L09805, doi:10.1029/2005GL025297.
- Makhlouf, U. B., Picard, R.H., and Winick, J. R. (1995), Photochemical-dynamical modeling of the measured response of airglow to gravity waves 1. Basic model for OH airglow, *J. Geophys. Res.*, *100*(D6), 11289-11311.
- McDade, I. C., and Llewellyn, E. J. (1987), Kinetic parameters related to sources and sinks of vibrationally excited OH in the nightglow, *J. Geophys. Res.*, *92*, 7643-7650.
- Mertens, C. J., Schmidlin, F. J., Goldberg, R. A., Remsberg, E. E., Pesnell, W. D., Russell III, J. M., Mlynczak, M. G., López-Puertas, M., Wintersteiner, P. P., Picard, R. H., Winick, J. R., and Gordley, L. L. (2004), SABER observations of mesospheric temperatures and comparisons with falling sphere measurements

- taken during the 2002 summer MacWAVE campaign, *Geophys. Res. Lett.*, *31*, L03105, doi:10.1029/2003GL018605.
- Myrabø, H. K., Deehr, C. S., and Sivjee, G. G. (1983), Large-amplitude nightglow OH(8-3) band intensity and rotational temperature variations during a 24-hour period at 78°N, *J. Geophys. Res.*, *88*(A11), 9255-9259.
- Myrabø, H. K., and Deehr, C. S. (1984), Mid-winter hydroxyl night airglow emission intensities in the northern polar region, *Planet. Space Sci.*, *32*, 263-271.
- Myrabø, H. K., Deehr, C. S., and Viereck, R. (1987), Polar mesopause gravity wave activity in the sodium and hydroxyl night airglow, *J. Geophys. Res.*, *92*(A3), 2527-2534.
- Mulligan, F. J., Horgan, D. F., Galligan, J. M., and Griffin, E. M. (1995), Mesopause temperatures and integrated band brightnesses calculated from airglow OH emissions recorded at Maynooth (53.2°N, 6.4°W) during 1993, *J. Atm. Terr. Phys.*, *57*, 1623–1637.
- Oberheide, J., Offermann, D., Russell III, J. M., and Mlynczak, M. G. (2006), Intercomparison of kinetic temperature from 15 μm CO<sub>2</sub> limb emissions and OH\*(3, 1) rotational temperature in nearly coincident air masses: SABER, GRIPS, *Geophys. Res. Lett.*, *33*, L14811, doi:10.1029/2006GL026439.
- W. R. Pendleton Jr., and M. J. Taylor (2002), The impact of L-uncoupling on Einstein coefficients for the OH Meinel (6,2) band: implications for Q-branch rotational temperatures, *J. Atmos. Sol. Terr. Physics*, *64*, 971-983.
- Sigernes, F., Shumilov, N., Deehr, C. S., Nielsen, K. P., Svenøe, T., and Havnes, O. (2003), The hydroxyl rotational temperature record from the Auroral Station in Adventdalen, Svalbard (78°N, 15°E), *J. Geophys. Res.*, *108*, doi: 10.1039/2001JA009023.
- Sivjee, G. G. and Hamwey, R. M. (1987), Temperature and chemistry of the polar mesopause OH, *J. Geophys. Res.*, *92*(A5), 4663-4672.
- Sivjee, G. G., Walterscheid, R. L., Hecht, J. M., Hamwey, R. M., Schubert, G. and Christensen, A. B. (1987), Effects of Atmospheric Disturbances on Polar Mesopause Airglow OH emissions, *J. Geophys. Res.*, *92*(A7), 7651-7656.

- She, C. Y., and Lowe, R. P. (1998), Seasonal temperature variations in the mesopause region at mid-latitude: comparison of lidar and hydroxyl rotational temperatures using WINDII/UARS OH height profiles, *J. Atmos. Sol. Terr. Phys.*, *60*(16), 1573–1583.
- Takahashi, H., Wrasse, C. M., Gobbi, D., Nakamura, T., Shiokawa, K., and Lima, L. M. (2005), Airglow OH emission height inferred from OH temperature and meteor trail diffusion coefficient, *Adv. Space Res.*, *35*, 1940-1944.
- Viereck, R. A., and Deehr, C. S. (1989), On the interaction between gravity waves and the OH Meinel (6-2) and the O<sub>2</sub> atmospheric (0-1) bands in the polar night airglow, *J. Geophys. Res.*, *94*, 5397-5404.
- Winick, J. R., P. P. Wintersteiner, R. H. Picard, D. Esplin, M. G. Mlynczak, J. M. Russell III, and L. L. Gordley (2009), OH layer characteristics during unusual boreal winters of 2004 and 2006, *J. Geophys. Res.*, *114*, A02303, doi:10.1029/2008JA013688.
- Wrasse, C. M., Takahashi, H., and Gobbi, D. (2004), Comparison of OH(8-3) and (6-2) band rotational temperature of the mesospheric airglow emissions, *Rev. Bras. Geof.*, *22*(3), doi: 10.1590/S0102-261X2004000300002.
- Yee, J.-H., G. Crowley, R. G. Roble, W. R. Skinner, M. D. Burrage, and P. B. Hays (1997), Global simulations and observations of O(<sup>1</sup>S), O<sub>2</sub>(<sup>1</sup>Σ) and OH mesospheric nightglow emissions, *J. Geophys. Res.*, *102*(A9), 19,949–19,968.



## **Paper 4**

### **Improved estimates for neutral air temperatures at 90 km and 78°N using satellite and meteor radar data**

Dyrland, M. E., C. M. Hall, and F. J. Mulligan (2009b)

## **Manuscript**

(Revised version submitted to *Radio Science*, Dec. 2009.)



# Improved estimates for neutral air temperatures at 90 km and 78°N using satellite and meteor radar data

M. E. Dyrland<sup>1</sup>, C. M. Hall<sup>2</sup>, and F. J. Mulligan<sup>3</sup>

<sup>1</sup>The University Centre in Svalbard, Longyearbyen, Norway

<sup>2</sup>Tromsø Geophysical Observatory, University of Tromsø, Norway

<sup>3</sup>National University of Ireland Maynooth

Corresponding author: [margit.dyrland@unis.no](mailto:margit.dyrland@unis.no)

**Abstract.** Recent reports using meteor wind radars (MWR) have shown that these instruments have considerable potential for monitoring atmospheric temperatures near 90 km altitude. Unlike many optically based instruments, they are not limited by clouds or by the need for darkness, which allows them to operate all year round for 24 hours per day. However, the raw temperatures produced by MWR instruments need calibration before they can be considered representative of the “true” atmospheric temperature. Extensive satellite data sets are now available and may be used as the calibration input. Two such data sets - Sounding of the Atmosphere using Broadband Emission Radiometry (SABER) and Aura Microwave Limb Scanner (MLS) - were examined in this study of the temperatures over Longyearbyen (78°N, 16°E). Aura MLS temperatures were chosen as the input for the calibration of initial temperature estimates derived from measurements of meteor echo fading times. The new calibration yielded 90 km neutral temperatures that were lower than the NRLMSISE-00 model both for winter and summer. The estimated temperature uncertainty was reduced to 7 K from the previous value of 17 K based on an earlier calibration using ground-based data.

## 1. Introduction

Making measurements of absolute neutral air temperatures from the mesopause region (~80-100 km) has long been considered an important [Jarvis, 2001], but notoriously difficult task. Mesopause region temperatures are valuable input to atmospheric chemistry models, as well as potential tracers of atmospheric dynamics and global change [Beig *et al.*, 2003]. One of the problems is that most

temperature retrieval algorithms are based on certain assumptions about the composition, the pressure or temperature gradients, the validity of thermodynamical equilibrium conditions, or other parameters [Polavarapu *et al.*, 2005]. This creates an ambiguity when interpreting the data as absolute neutral air temperatures. Measuring the temperature at high-Arctic latitudes ( $>75^{\circ}\text{N}$ ) is even more difficult, as there are few facilities and instruments available at these locations often because of logistical challenges due to a harsh climate. Also, many satellites' field of view do not extend to such high latitudes.

One of the few high-Arctic locations where ground-based measurements have been performed for several decades is Adventdalen ( $78^{\circ}\text{N}$ ,  $16^{\circ}\text{E}$ ), a valley close to the city Longyearbyen on the Svalbard archipelago. A long term winter temperature series has been derived from spectral measurements of hydroxyl (OH) airglow emissions for the last three decades [Sigernes *et al.*, 2003]. However, these temperatures can only be retrieved for polar night conditions (November through February) and when there are relatively clear skies and low auroral activity [e.g. Viereck and Deehr, 1989]. The temperature at 90 km can be deduced from the diffusion of meteor trails, and a method was developed by Hall *et al.* [2004] for obtaining these temperatures from a meteor radar also located in Adventdalen. These measurements have the advantage that they can be made throughout the full day and for all seasons.

The method involves calibration by an independent temperature series. Calibration by OH rotational temperatures (winter) and K-Lidar measurements (summer 2001-2003) have proven to yield overall realistic relative variations of the temperature at 90 km and the time series from 2001-2006 was reported by Hall *et al.* [2006]. The calibration procedure was based on the assumption that the rotational temperature of the OH(6-2) band is representative of the neutral temperature at  $\sim 87$  km altitude, an assumption that has been widely accepted and used [c.f. Sivjee, 1992; Beig *et al.*, 2003]. The measured OH rotational temperatures were adjusted from 87 km to 90 km according to the temperature gradient from a model, before being used as calibration input for the temperatures measured by the meteor radar [Hall *et al.*, 2006].

Recent studies have shown that the OH emission peak altitude can vary by several kilometers and that variations are particularly large at high-Arctic latitudes [Winick *et al.*, 2009]. Using satellite data they show that for extended periods

during the winters 2004 and 2006, the OH emission peak was located well below 80 km and large asymmetries were present within the Arctic region. Simultaneous ground-based and satellite measurements of OH airglow above Svalbard have revealed that the altitude variations are responsible for a large part of the fluctuations in the observed OH rotational temperatures (Dyrland et al., The response of OH airglow temperatures to neutral air dynamics at 78°N, 16°E during the anomalous 2003-2004 winter, manuscript #2009JD012726 submitted to J. Geophys. Res., 2009). For periods of low OH emission peak altitude, the calibrated temperatures from the meteor radar might therefore be overestimated. The opposite is also possible, but more rare.

Another recent study (Mulligan et al., Inferring hydroxyl layer peak heights from ground-based measurements of OH(6-2) band radiance at Longyearbyen (78°N, 16°E), manuscript #angeo-2009-119 submitted to Ann. Geophys., 2009) presents an empirical formula for attributing a peak height to an OH rotational temperature measurement based on the observed intensity of the OH emissions. Still, we are left with the problem of limited data coverage, both seasonally and daily. There are also studies that indicate that the OH rotational temperatures from the 6-2 band are not necessarily representative of the neutral air temperatures [Cosby and Slanger, 2007]. Awareness of these issues has prompted us to look for other independent temperature measurements to act as input to the meteor radar temperature retrieval algorithm.

Relatively recent launches of satellites probing the mesopause region have provided data sets that can be used for comparison with ground-based measurements. Some of these satellites have orbits with a high inclination angle to the equator which enables their onboard instruments to make observations at latitudes as high as  $\pm 80$  degrees. The two instruments that are of particular interest for this report are SABER (Sounding of the Atmosphere by Broadband Emission Radiometry) on board TIMED (Thermosphere Ionosphere Mesosphere Energetics and Dynamics) which was launched in 2001, and MLS (Microwave Limb Sounder) on board the EOS (Earth Observing System) Aura spacecraft launched in 2004. In this paper we examine the temperature data sets available for Longyearbyen for 2005 from the meteor radar and these two satellite instruments. We compare the temperature sets, and investigate the effect of replacing ground-based temperature sets used in previous calibrations of the MWR temperatures by satellite values.

## 2. Instruments

The data presented in this paper are retrieved from two satellites and a ground-based meteor radar. A brief overview of the three instruments and their temperature retrieval algorithms is presented in the following paragraphs. Further detail may be obtained from the references included.

### 2.1 The NSMR meteor wind radar

The NSMR (Nippon/Norway Svalbard Meteor Radar) radar is of the type meteor wind radar (MWR), often simply called a meteor radar. The NSMR radar and the temperature retrieval technique are extensively described and discussed by *Hall et al.* [2004; 2006], and references therein.

The Svalbard system operates at 31 MHz and detects echoes from meteors by receivers arranged as an interferometer. From these echoes, ambipolar diffusion coefficients  $D$  can be derived by measuring the radar echoes' decay time  $\tau$  [*Chilson et al.*, 1996]. The two are related in the following way:

$$\tau = \frac{\lambda^2}{16\pi^2 D} \quad (1)$$

Using atmospheric pressure as input, temperatures can then be derived from the daily averaged ambipolar diffusion coefficients using the expression:

$$T = \sqrt{\frac{p \cdot D}{6.39 \cdot 10^{-2} K_0}} \quad (2)$$

Where  $p$  (Pa) is the pressure and  $K_0$  is the zero field mobility, which depends on the ion species in the meteor trail.  $K_0$  is chosen according to *Cervera and Reid* [2000] and is assumed to be  $2 \times 10^{-4} \text{ m}^2 \text{ s}^{-1} \text{ V}^{-1}$ . Pressure values are derived from a combination of the empirical models of *Lübken and von Zahn* [1991] and *Lübken* [1999], these values have proven to be appropriate at  $70^\circ\text{N}$  [*Hall et al.*, 2006], and were adjusted to  $78^\circ\text{N}$  by the meridional gradient indicated by the model NRLMSISE-00 [*Picone et al.*, 2002]. In this paper we will refer to temperatures measured by the NSMR meteor radar as MWR temperatures. A meteor radar at such a high latitude as  $78^\circ\text{N}$  suffers less from diurnal variation of meteor occurrence than at lower latitudes, so calculating daily mean temperatures are believed to yield relatively small diurnal biases. Figure 1 shows a typical daily distribution of meteor echoes measured by NSMR. A maximum is seen at  $\sim 90$  km.

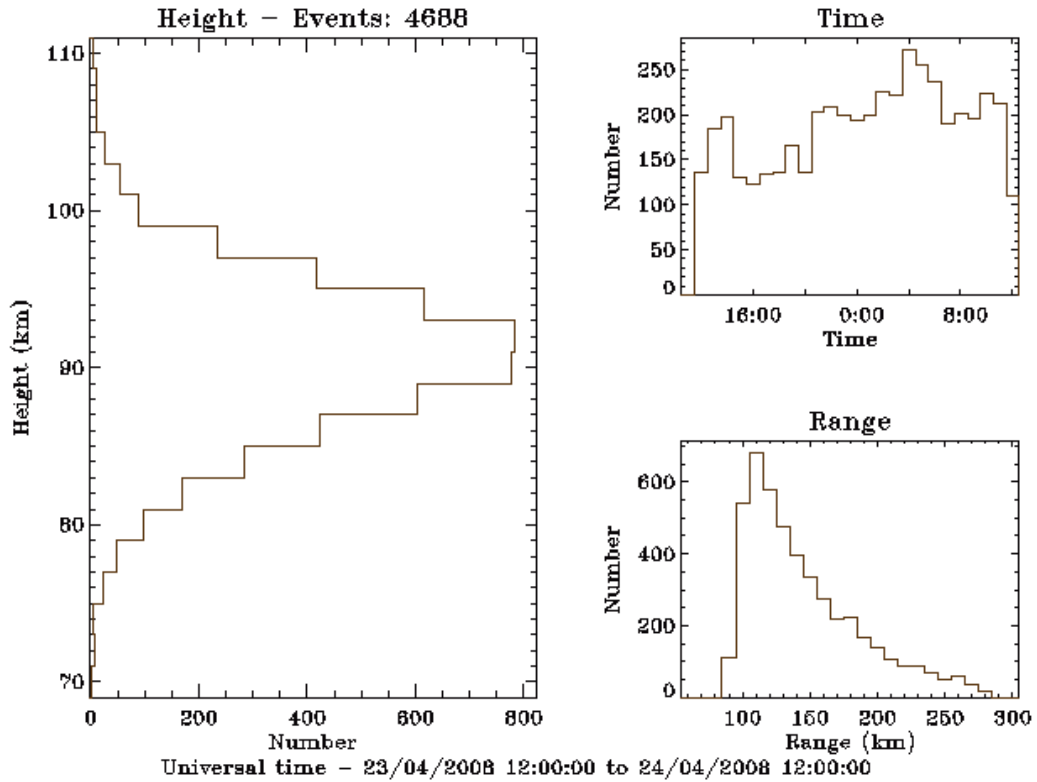


**Figure 1.** Height, range and time distribution of meteor echoes detected by the NSMR radar between 23 April 12 UT and 24 April 12 UT 2008.

## 2.2 TIMED SABER

SABER (Sounding of the Atmosphere by Broadband Emission Radiometry) was launched on the satellite TIMED (Thermosphere Ionosphere Mesosphere Energetics and Dynamics) in 2001. SABER scans the horizon and obtains temperatures from measurements of CO<sub>2</sub> 15 μm limb emissions. The observed limb emission profiles are analyzed to produce vertical temperature profiles with approximately 2 km vertical resolution [Mertens *et al.*, 2004]. The view of SABER is 90° to the right of the velocity vector of the TIMED spacecraft. Every 60-63 days the spacecraft switches between northward and southward looking yaw modes. It is only in the northward looking yaw mode that latitudes between 52-83°N can be observed.

We selected SABER profiles with tangent points at an altitude of  $90 \pm 10$  km and geographic coordinates within  $78 \pm 5^\circ\text{N}$ ,  $16 \pm 10^\circ\text{E}$  (circle of  $\sim 600$  km). The temperatures used in this study are retrieved from version 1.07 data and are validated by *Remsberg et al.* [2008]. We will refer to them as SABER temperatures in the following. *García-Comas et al.* [2008] did a thorough investigation of errors in the SABER temperatures caused by non-local-thermodynamic-equilibrium (non-LTE) parameters and found that for strong inversion layers, the errors could reach  $\pm 9\text{K}$  at  $\sim 90$  km. *Remsberg et al.* [2008] summarized the total errors due to noise and biases and found that for polar winter it was  $\sim 5\text{K}$  and for polar summer  $\sim 10\text{K}$ . The blue plusses joined by straight lines in figure 2 show an example of a vertical temperature profile from SABER. Mesospheric inversion layers (MIL) are seen at  $\sim 75$  km.

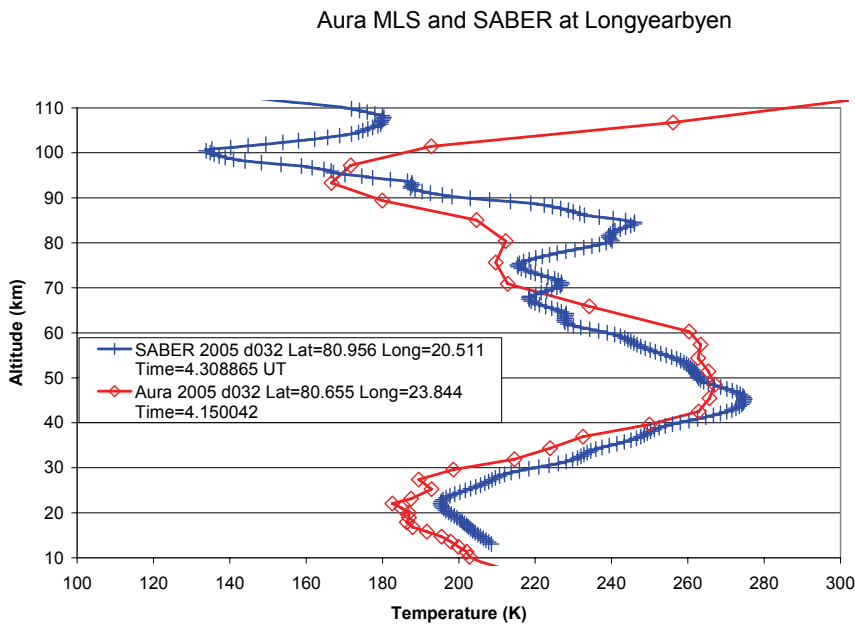


**Figure 2.** Examples of SABER (blue plusses joined by straight lines) and Aura MLS (red diamonds joined by straight lines) vertical temperature profiles from scans obtained during the winter day 1 February 2005 at  $\sim 4\text{UT}$ .

## 2.3 Aura MLS

The MLS (Microwave Limb Sounder) was launched on the EOS (Earth Observing System) Aura spacecraft in 2004. Temperatures are retrieved from thermal emissions near the 118 GHz O<sub>2</sub> and 234 GHz O<sup>18</sup>O spectral lines. Version 2.2 of the temperature retrieval algorithm is used [Livesey *et al.*, 2006]. Scans with tangent points at geographic coordinates within (78±5°N, 16±10°E) were selected (corresponds to ~600 km from observing station). This gave ~22000 individual temperature estimates from August 2004 to June 2009.

Data were selected according to data-quality criteria specified by Schwartz *et al.* [2008]. The resolution in the 80-100 km region is only ~13 km. Temperatures at 90 km were thus found by interpolation between points covering these altitudes. Schwartz *et al.* [2008] published a validation paper on the Aura MLS data and found that it had a cold bias of 9K at ~97 km compared to SABER and ACE (Atmospheric Chemistry Experiment) satellite temperatures and meteorological analyses available. They also found a seasonal difference in the bias. However, Schwartz *et al.* [2008] used SABER temperatures version 1.06 for their comparison, where the non-LTE effects in the summer mesopause mentioned in section 2.2 were not fully accounted for [Remsberg *et al.*, 2008]. This was expected to be the reason for the divergence between the summer and winter biases.

The red diamonds joined by straight lines in Figure 2 visualize the vertical profile of Aura MLS temperatures for a winter scan. The winter day scan is from approximately the same time as the SABER scan in Figure 2. It is clear that there are large differences owing to the different field of views and vertical and horizontal resolutions of the two instruments. The Aura MLS temperatures are colder than SABER temperatures in the upper mesosphere. The Aura MLS profile show less structure. The mesospheric inversion layers (MILs) clearly seen in the SABER data between 75 and 85 km, is not evident in the Aura MLS profile.

## 3. Data

### 3.1 Correlations

Initial estimates of the 90 km temperature are obtained from the meteor radar measurements of the fading time of meteor echoes. We have called these “raw” temperatures, since they are the output of the Equation 2 using daily averaged

pressures from a model as input. Daily averaged “raw” MWR temperatures from 2005 are shown as a black dashed line in the top panel of Figure 3. Daily averaged SABER and Aura MLS temperatures from the same year are indicated by a blue dotted line and a red solid line, respectively.

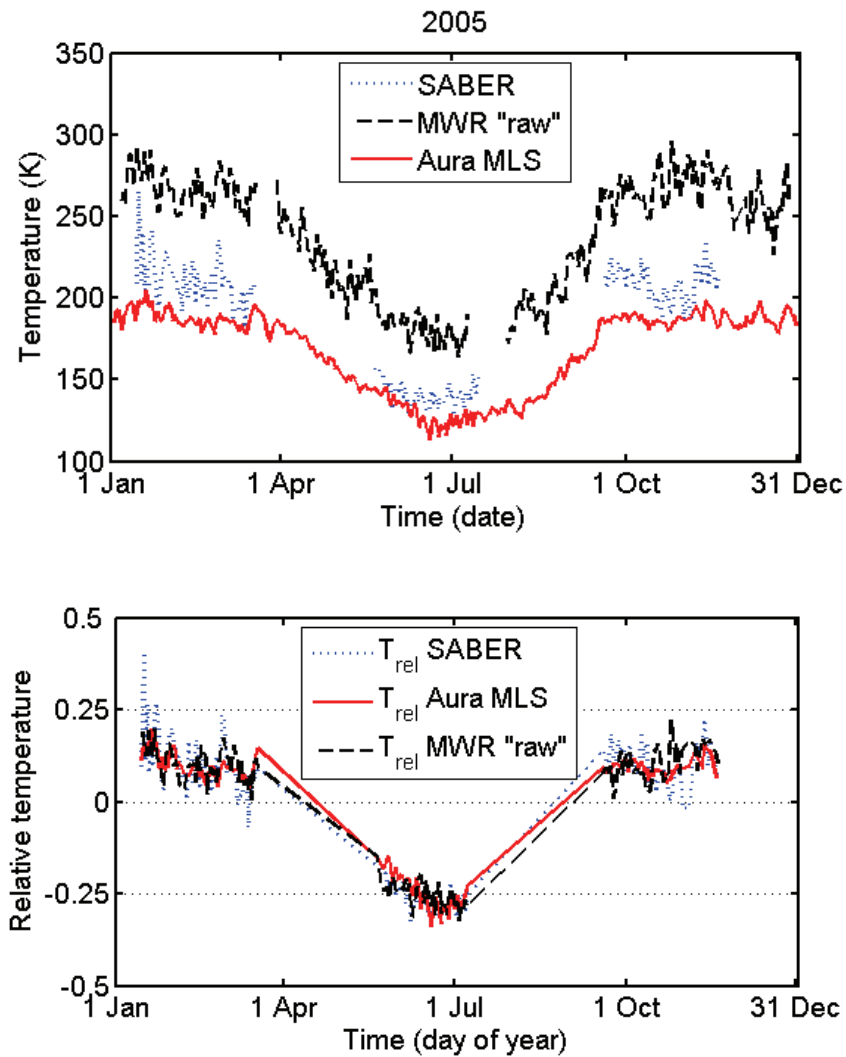


**Figure 3.** Top panel: Initial estimates of daily averaged 90 km MWR temperatures for 2005 are shown as a black dashed line and denoted MWR “raw”. The daily averaged SABER and Aura MLS temperatures are displayed as a blue dotted and a red solid line, respectively. Lower panel: Same as above, but relative temperatures (to their yearly mean).

Data from the three instruments are available for longer time periods - 2001-2009 for NSMR, 2001-2009 for SABER and 2004-2009 for Aura MLS. For reasons of easy data access, we chose the data from 2005 for our initial comparisons.

From the top panel of Figure 3 we see that all three temperature series display very similar relative variations. However, as expected we see that the absolute value of the “raw” MWR temperatures are too high and need adjustment by independent measurements as described by *Hall et al.* [2004; 2006].

In the lower panel of Figure 3 we have plotted the relative temperatures for the 155 days in 2005 when the three measurements coincided, i.e. the relative temperatures of each temperature series are computed according to:

$$T_{rel\ MWR/AuraMLS/SABER} = \frac{T_{MWR/AuraMLS/SABER} - \bar{T}_{MWR/AuraMLS/SABER}}{\bar{T}_{MWR/AuraMLS/SABER}} \quad (3)$$

where  $\bar{T}$  is the annual average of each set. For the relative temperature series we computed the correlation coefficients  $R$  of the linear relationships. For MWR “raw” and SABER the correlation coefficient  $R=0.93$  with a probability of random occurrence:  $p<10^{-68}$ . For the relative Aura MLS and MWR “raw” temperatures the correlation is 0.96 with  $p<10^{-88}$ . For the Aura MLS and SABER data,  $R=0.95$  and  $p<10^{-81}$ .

### 3.2 Bias between SABER and Aura MLS temperatures

To validate our choice of which data set to use for calibration of the meteor radar temperatures, it is useful to examine the offsets between the various data sets. *Schwartz et al.* [2008] found a 9 K bias between Aura MLS and SABER temperatures, the latter being higher. We will now determine the differences between these two data sets above Longyearbyen.

From the coinciding days of 2005 shown in the lower panel of Figure 3, we calculated the difference between the Aura MLS and the SABER temperatures. We found a mean positive bias for SABER of  $19 \pm 11$  K. From Figure 3 it is obvious that the difference is larger in winter than summer due to the relatively large variability of SABER temperatures in winter compared to Aura MLS. In winter, spring and autumn the average difference between SABER and Aura MLS is  $22 \pm 11$  K, and for summer it is  $11 \pm 7$  K. This is higher than the 9 K bias observed by *Schwartz et al.* [2008]. However, their bias was obtained by comparing individual

profiles within 2 degrees of great circle arc (220 km) and 3 hours in time from the whole globe, and they used version 1.06 of the SABER data.

Figure 4 shows the universal times (UT) of the AURA MLS (top panel) and SABER (lower panel) measurements from 2005. We see that the Aura MLS measurement times are constant throughout the year and they are the same for all the years from 2004-2009 (not shown).

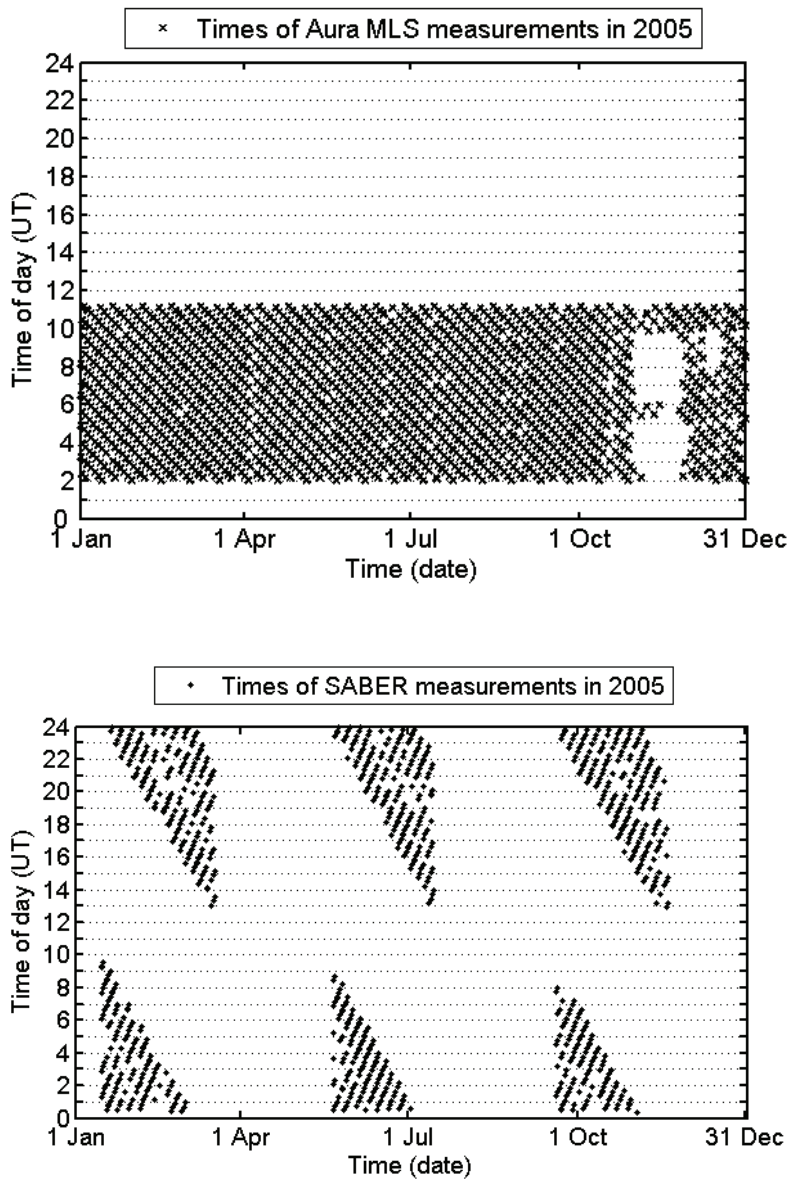


**Figure 4.** UT times of AURA MLS (top panel) and SABER (lower panel) measurements at Longyearbyen within 600 km from the meteor radar site in 2005.

The SABER times change according to the orbit of TIMED. This means that the daily averages are from different times of day in the course of a year. Aura MLS data are available on almost every day of the year, whereas SABER data has three 60-day gaps in each year corresponding to a southward viewing yaw phase. This fact and the reports of total errors in the order of  $\sim 10$  K for the SABER summer temperatures due to noise and difficulties in the non-local-thermodynamical temperature retrieval algorithm [Remsberg *et al.*, 2008], we selected Aura MLS data as the optimal input for the MWR calibration.

## 4. Improved estimates of 90 km MWR temperatures

### 4.1 Calibration by Aura MLS temperatures

Based on our investigations in the paragraphs above, we choose to use the Aura MLS data for our calibration of the MWR data. Between 14 August 2004 and 15 April 2009 there were 1398 days when Aura MLS measurements coincided with MWR measurements. The coinciding daily averages are shown in Figure 5.

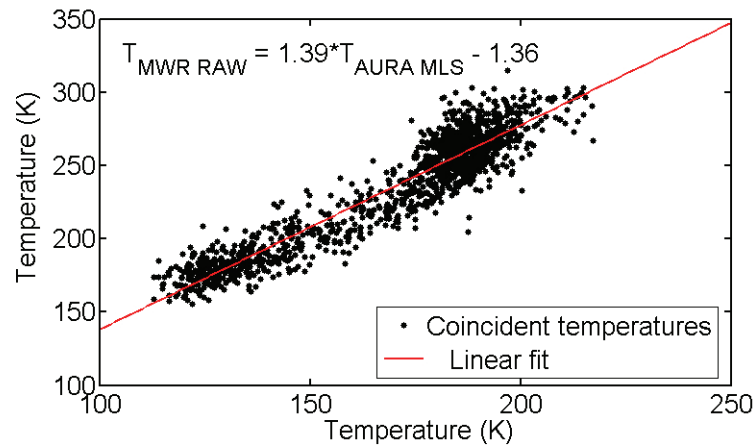


**Figure 5.** Scatter plot of coincident daily averages of Aura MLS and MWR raw temperatures between 14 August 2004 and 15 April 2009. The red line indicates the best linear fit and the equation is given. The correlation coefficient is 0.94 and the probability for random occurrence is zero.

We use the inverse of the equation for the linear relationship between Aura MLS and MWR temperatures displayed in the left corner of Figure 5, to calibrate/adjust the MWR temperatures to a realistic value. The equation we use is:

$$T_{MWR\_CALIB} = 0.72 \cdot T_{MWR\_RAW} + 0.98 \quad (4)$$

The resulting temperatures are shown as black plusses in Figure 6. We have also plotted the MSIS-00 temperatures at 90 km (orange line) for constant solar input. MSIS-00 seems to be generally warmer than  $T_{MWR\_CALIB}$  in both summer and winter. Using spectrometer and K-Lidar data as independent temperature input for the calibration, *Hall et al.* [2006] found a similar result. The Aura MLS temperatures were reported to have a 9 km cold bias compared to SABER [*Schwartz et al.*, 2008]. Adding this bias to the Aura MLS data would obviously give us higher MWR temperatures which correspond better with MSIS-00. However, the K-lidar measurements from 2001-2003 indicate that MSIS-00 underestimates the summer minimum temperature above Svalbard when temperatures as low as 120 K were observed [*Höffner and Lübken*, 2007].

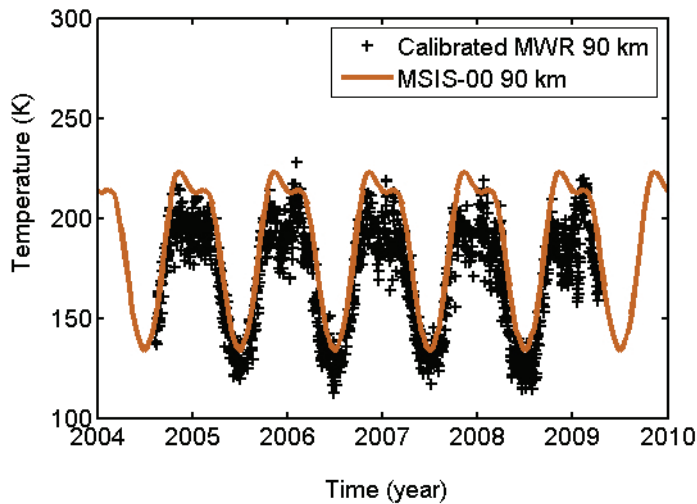


**Figure 6.** Calibrated MWR temperatures for August 2004 to April 2009 (black plusses). The inverse of the linear relationship from Figure 5 is used to adjust the “raw” MWR temperatures to “calibrated” temperature values. The orange line shows the MSIS-00 model result for constant solar input.

They report a consistent 10-20 K difference between the K-lidar and MSIS-00 temperatures. For Antarctic winter conditions *Azeem et al.* [2007] report a root-mean-square difference between MSISE-00 and meospause region temperatures of 7.5 K.

So the question of which temperature retrieval method comes closest to obtaining the true neutral air temperature at 90 km remains unresolved. However, as we will show in the next section, the use of Aura MLS temperatures has enabled us to reduce the uncertainty associated with the temperatures produced by the MWR.

## 4.2 Estimating the uncertainty in MWR temperatures

We adopt the approach of *Hall et al.* [2004] in estimating the uncertainty in the calibrated MWR temperatures. Figure 7 shows a scatter plot of the calibrated MWR temperatures as a function of the corresponding Aura MLS temperature.

We have performed a linear least squares fit of the calibrated meteor radar derived temperatures to the independent Aura MLS measurements (red dashed line). The intercept and slope of this line is very close to unity and zero, respectively (the unity intercept and zero slope line is shown as a blue solid line). The mean absolute deviation from the zero slope and intercept line, was found to be  $\pm 7$  K and is indicated by the green dashed lines in Figure 7. *Hall et al.* [2004] found a value of 17 K when rotational OH(6-2) temperatures and K-lidar data was used, and argued that this value was a reasonable representation of the uncertainty that might be expected in temperatures obtained from the radar. Substituting Aura MLS temperature data in place of the K-lidar and OH optical temperatures as the input to the MWR temperature calibration appears to have produced a significant reduction in the uncertainty of the standard error of the calibrated MWR values. However, we should note that the Aura MLS daily averages are averages from measurements made during the times 02-11 UT while the MWR data are averaged over a full day. Thus we need to consider possible diurnal biases between Aura MLS and the MWR temperatures before treating the MWR temperatures as absolute temperatures. The NSMR detects enough echoes for 30 minute averages to be computed, but ambiguities are introduced when choosing input pressures for the analysis.

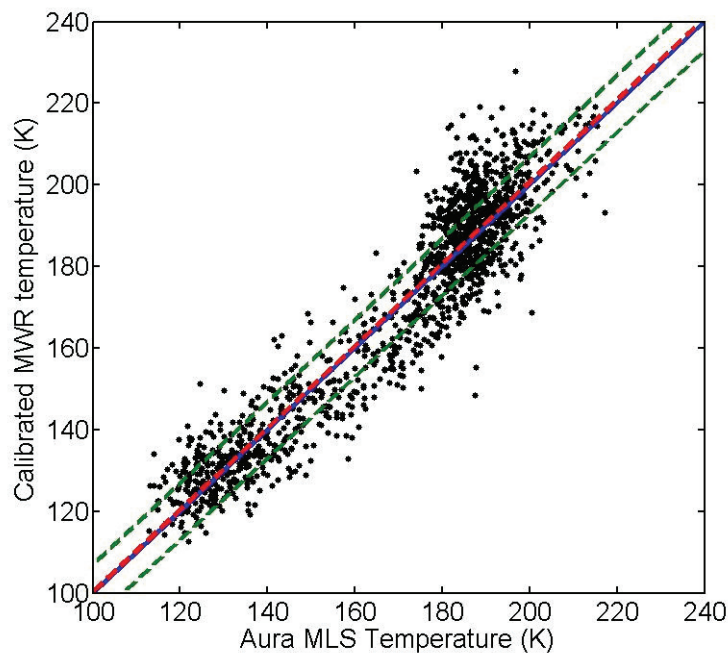


**Figure 7.** Calibrated meteor radar derived temperatures as a function of the corresponding Aura MLS temperatures. The regression line is shown as a red dashed line, while the blue solid line indicates the line of unity slope and zero intercept. The mean absolute deviation is indicated by the dashed green lines above and below.

Daily average pressure values and variations are available, but not intra-daily. There is presumably an intra-day variation of pressures as well as temperature, so this might introduce biases in the time series that are not real.

One possibility could be to derive pressures from independent temperature measurements and use them as empirical input, but then we need to be careful not to introduce any circular arguments like those described by *Polavarapu et al.* [2005]. Making these considerations is an important task for future studies of MWR and satellite temperatures from Svalbard.

## 5. Conclusions

In this paper we have presented measurements of 90 km temperatures above the high Arctic location Longyearbyen, Svalbard (78°N, 16°E). The temperatures were measured by satellites and a ground-based meteor radar. Comparison of the daily averages measured by the satellite instruments: Sounding of the Atmosphere using Broadband Emission Radiometry (SABER) and Aura Microwave Limb Scanner (MLS), showed that SABER was warmer by an average  $19 \text{ K} \pm 11 \text{ K}$  during the winter 2005. The error is the standard deviation from the mean difference. The difference was larger in winter than summer ( $22 \pm 11 \text{ K}$  versus  $11 \pm 7 \text{ K}$ , respectively).

Both the SABER and Aura MLS data display similar relative variations to the initial temperature derived from measurements of meteor echo fading times. Correlation coefficients of 0.93 and 0.96 were found for SABER-MWR and Aura MLS-MWR, respectively. However, Aura MLS makes measurements at the same time of day every day, while SABER's viewing angle changes during the season leading to a variation in observing times. This and the knowledge of the relatively large uncertainties in SABER measurements during polar summer [Remsberg *et al.*, 2008] led us to choose the Aura MLS data as input to the calibration of the MWR data.

The new calibration yielded 90 km neutral temperatures that were lower than the NRLMSISE-00 model both for winter and summer, but in accordance with the K-lidar measurements from summers 2001-2003. The estimated temperature uncertainty was reduced to 7 K, compared to the previous value of 17 K which was obtained when the calibration was performed using ground-based temperatures.

**Acknowledgments.** The satellite data used in this study were acquired as part of the activities of the NASA Earth-Sun System Division, and are archived and distributed by the Goddard Earth Sciences (GES) Data and Information Services Center (DISC). We are highly appreciative of the NASA EOS Aura MLS and NASA TIMED SABER teams for providing free access to the data. We are also grateful to Professor Chuck Deehr at The Geophysical Institute, University of Alaska Fairbanks and Professor Takehiko Aso, National Institute of Polar Research, Tokyo, for their initiatives for putting the ground-based instruments in Svalbard and for sharing the data.

## References

- Azeem, S. M. I., G. G. Sivjee, Y.-I. Won, and C. Mutiso (2007), Solar cycle signature and secular long-term trend in OH airglow temperature observations at South Pole, Antarctica, *J. Geophys. Res.*, *112*, A01305, doi:10.1029/2005JA011475.
- Beig, G., P. Keckhut, R. P. Lowe, R. G. Roble, M. G. Mlynczak, J. Scheer, V. I. Fomichev, D. Offermann, W. J. R. French, M. G. Shepherd, A. I. Semenov, E. E. Remsberg, C. Y. She, F. J. Lübken, J. Bremer, B. R. Clemesha, J. Stegman, F. Sigernes, and F. Fadnavis (2003), Review of mesospheric temperature trends, *Rev. Geophys.*, *41*(4), 1015, doi:10.1029/2002RG000121.
- Cervera, M. A., and I. M. Reid (2000), Comparison of atmospheric parameters derived from meteor observations with CIRA, *Radio Sci.*, *35*, 833-843.
- Chilson, P. B., P. Czechowsky, and G. Schmidt (1996), A comparison of ambipolar diffusion coefficients in meteor trains using VHF radar and UV lidar, *Geophys. Res. Lett.*, *23*, 2745-2748.
- Cosby, P. C., and T. G. Slanger (2007), OH spectroscopy and chemistry investigated with astronomical sky spectra, *Can. J. Phys.*, *85*, 77-99, doi: 10.1139/P06-088.
- García-Comas, M., M. López-Puertas, B. T. Marshall, P. P. Wintersteiner, B. Funke, D. Bermejo-Pantaleón, C. J. Mertens, E. E. Remsberg, L. L. Gordley, M. G. Mlynczak, and J. M. Russell III (2008), Errors in Sounding of the Atmosphere using Broadband Emission Radiometry (SABER) kinetic temperature caused by non-local-thermodynamic-equilibrium model parameters, *J. Geophys. Res.*, *113*, D24106, doi:10.1029/2008JD010105.
- Hall, C. M., T. Aso, M. Tsutsumi, J. Höffner, and F. Sigernes (2004), Multi-instrument derivation of 90 km temperatures over Svalbard (78°N 16°E), *Radio Sci.*, *39*, RS6001, doi:10.1029/2004RS003069.
- Hall, C. M., T. Aso, M. Tsutsumi, J. Höffner, F. Sigernes, and D. A. Holdsworth (2006), Neutral air temperatures at 90 km and 70°N and 78°N, *J. Geophys. Res.*, *111*, D14105, doi: 10.1029/2005JD006794.
- Höffner, J., and F.-J. Lübken (2007), Potassium lidar temperatures and densities in the mesopause region at Spitsbergen (78°N), *J. Geophys. Res.*, *112*, D20114, doi:10.1029/2007JD008612.

- Jarvis, M. J. (2001), Bridging the atmospheric divide, *Science*, 293, 2218-2219, doi:10.1126/science.1064467.
- Livesey, N. J., W. V. Snyder, W. G. Read, and P. A. Wagner (2006), Retrieval algorithms for the EOS Microwave Limb Sounder (MLS), *IEEE Trans. Geosci. Remote Sens.*, 44, 1144-1155.
- Lübken, F.-J., and U. von Zahn (1991), Thermal structure of the mesopause region at polar latitudes, *J. Geophys. Res.*, 96, 20841-20857.
- Lübken, F.-J. (1999), Thermal structure of the Arctic summer mesosphere, *J. Geophys. Res.*, 104, 9135-9149.
- Mertens, C. J., F. J. Schmidlin, R. A. Goldberg, E. E. Remsberg, W. D. Pesnell, J. M. Russell, M. G. Mlynczak, M. López-Puertas, P. P. Wintersteiner, R. H. Picard, J. R. Winick, and L. L. Gordley (2004), SABER observations of mesospheric temperatures and comparisons with falling sphere measurements taken during the 2002 summer MacWAVE campaign, *Geophys. Res. Lett.*, 31, L03105, doi: 10.1029/2003GL018605.
- Picone, J. M., A. E. Hedin, D. P. Drob, and A. C. Aikin (2002), NRLMSISE-00 empirical model of the atmosphere: Statistical comparisons and scientific issues, *J. Geophys. Res.*, 107(A12), 1468, doi:10.1029/2002JA009430.
- Polaravapu, S, T. G. Shepherd, Y. Rochon, and S. Ren (2005), Some challenges of middle atmosphere data assimilation, *Q. J. R. Meteorol. Soc.*, 131, 3513-3527, doi: 10.1256/qj.05.87.
- Remsberg, E. E., B. T. Marshall, M. Garcia-Comas, D. Krueger, G. S. Lingenfelter, J. Martin-Torres, M. G. Mlynczak, J. M. Russell III, A. K. Smith, C. Brown, L. L. Gordley, M. J. Lopez-Gonzales, M. Lopez-Puertas, C.-Y. She, M. J. Taylor, and R. E. Thomson (2008), Assessment of the quality of the Version 1.07 temperature-versus-pressure profiles of the middle atmosphere from TIMED/SABER, *J. Geophys. Res.*, 113, D17101, doi:10.1029/2008JD010013.
- Schwartz, M. J., A. Lambert, G. L. Manney, W. G. Read, N. J. Livesey, L. Froidevaux, C. O. Ao, P. F. Bernath, C. D. Boone, R. E. Cofield, W. H. Daffer, B. J. Drouin, E. J. Fetzer, R. A. Fuller, R. F. Jarnot, J. H. Jiang, B. W. Knosp, K. Krüger, J.-L. F. Li, M. G. Mlynczak, S. Pawson, J. M. Russell III, M. L. Santee, W. V. Snyder, P. C. Stek, R. P. Thurstans, A. M. Thomkins, P. A. Wagner, K. A. Walker, J. W. Waters, and D. L. Wu (2008), Validation of the

- Aura Microwave Limb Sounder temperature and geopotential height measurements, *J. Geophys. Res.*, *113*, D15S11, doi:10.1029/2007JD008783.
- Sigernes, F., N. Shumilov, C. S. Deehr, K. P. Nielsen, T. Svenøe, and O. Havnes (2003), The Hydroxyl rotational temperature record from the Auroral Station in Adventdalen, Svalbard (78°N, 15°E), *J. Geophys. Res.*, *108*, doi:10.1029/2001JA009023.
- Sivjee, G. G. (1992), Airglow hydroxyl emissions, *Planet. Space. Sci.*, *40*, 235-242.
- Viereck, R. A., and C. S. Deehr (1989), On the interaction between gravity waves and the OH Meinel (6-2) and the O<sub>2</sub> atmospheric (0-1) bands in the polar night airglow, *J. Geophys. Res.*, *94*, 5397-5404.
- Winick, J. R., P. P. Wintersteiner, R. H. Picard, D. Esplin, M. G. Mlynczak, J. M. Russell III, and L. L. Gordley (2009), OH layer characteristics during unusual boreal winters of 2004 and 2006, *J. Geophys. Res.*, *114*, A02303, doi:10.1029/2008JA013688.